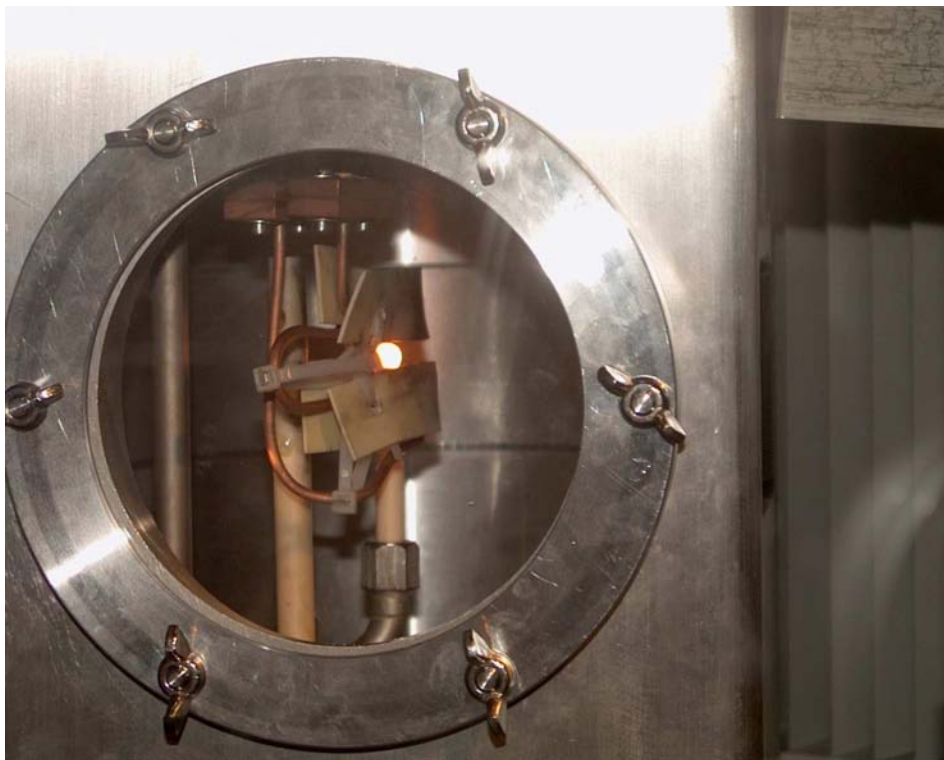


ANNUAL REPORT 2006
Forschungs-Neutronenquelle
Heinz Maier-Leibnitz (FRM II)



cover image: An electromagnetic levitation furnace from the Institut für Materialphysik im Weltraum of the Deutschen Zentrums für Luft- und Raumfahrt (DLR). For details see section 9.5.

Contents

Directors' report	2
The year in pictures	3
I Instrumentation	7
1 Central services and reactor	8
1.1 Detector and electronics lab	8
1.2 HELIOS	9
1.3 Calibration of the control rod	11
1.4 Sample environment	13
1.5 Neutron flux	13
1.6 High density fuel	16
2 Thin films and large scale structures	19
2.1 KWS-1 and KWS-2	19
2.2 MIRA	21
2.3 N-REX+	26
2.4 SANS-1	27
2.5 TREFF@NOSPEC	29
3 Structure research	31
3.1 HEIDI	31
3.2 POLI-HEiDi	33
3.3 RESI	36
3.4 SPODI	37
3.5 STRESS-SPEC	38
4 Inelastic scattering, high resolution	41
4.1 DNS	41
4.2 J-NSE	43
4.3 RESEDA	44
4.4 SPHERES	45
4.5 TOFTOF	48
5 Three axes spectroscopy	49
5.1 PANDA	49
5.2 PUMA	51
6 Imaging at ANTARES and NECTAR	54
6.1 Imaging the cold source	54
6.2 Beam filters for imaging	56
6.3 Phase contrast tomography	57
6.4 NECTAR	59
7 Nuclear and particle physics	62
7.1 NEPOMUC	62
7.2 Positron remoderation	63
7.3 MEPHISTO	64
7.4 UCN	66

8 Industrial applications	69
8.1 Irradiation	69
8.2 MEDAPP	71
II Science	73
9 Scientific highlights	74
9.1 Solvent content in thin spin-coated polymer films	74
9.2 CDBS	75
9.3 PAES-measurements of pure Cu and Cu coated Si(100)	77
9.4 ANTARES – Investigation of an early medieval sword by neutron tomography	78
9.5 Containerless sample processing at TOFTOF	80
9.6 Larmor diffraction at TRISP	82
9.7 Molecular dynamics in pharmaceutical drug delivery systems	84
10 Events	87
10.1 Workshop - Residual stress analysis	87
10.2 Workshop - Neutrons for Geoscience	87
10.3 Workshop industrial applications	88
10.4 Workshop biological and soft matter interfaces	89
10.5 Farewell colloquium Prof. Klaus Schreckenbach	90
III Facts and Figures	91
11 Experiments and user program	92
User office	92
Instruments	92
User support	94
Industrial applications	94
12 Public relations and visitor service	95
13 People	98
13.1 Committees	98
13.2 Staff	104
13.3 Partner institutions	106
14 Figures	107
14.1 Publications	107
Imprint	111

Directors' report

Plenty of Neutrons

The past year's outstanding event was the 260-day operation at full power of FRM II. Already in its second year of routine operation our neutron source achieved this record, which certainly is exceptional for high flux neutron sources. Congratulations to both our nuclear staff, who managed the smooth operation in 2006, and to our experimentalists, who served users over this period.

By the end of 2006 fifteen beam hole instruments served in routine operation. Essential progress was made in the licensing of MEDAPP, our clinical cancer irradiation facility, and we all hope to get the final approval from the Bavarian Ministry of Environment, Health and Consumer Protection early 2007. The Jülich Centre for Neutron Science (JCNS) transported its first instrument - the Neutron Spin Echo Spectrometer - to FRM II in March 2006. With the end of the 7th reactor cycle MEPHISTO, the instrument for nuclear physics, had to move from its original position at neutron guide NL3 to NL2a, in order to make room for the installation of the three small angle scattering machines of JCNS. The new east building with the new guide hall on its ground floor and the offices and labs for JCNS on its first floor made significant progress over the year. We expect JCNS to move into that building in February 2007. However, the extension of the neutron guide hall west towards the Atomic Egg advanced slowly. The Jülich small angle scattering machines are waiting for this extension impatiently in order to start their routine operation.

Important advances have been made in the attempts to develop high den-

sity fuels for future use in FRM II. Within a collaboration of CEA (Commissariat à l'Énergie Atomique), CERCA (the French producer of the FRM II fuel element), AREVA NP and TUM large fuel plates with a 8 g/cm^3 dense U8wt%Mo alloy have been irradiated to integral neutron fluxes beyond the need of FRM II. So far conservative swelling has been observed. However, there is still a long way to pursue until these high density fuels will be qualified for the use in high flux neutron sources.

On 26 June 2006 the Bavarian Minister of Science, Dr. Thomas Goppel, invited the members of the European Parliament to the Bavarian Embassy, a marvellous place in the heart of Brussels, in order to present FRM II as a Bavarian and German contribution to the European Research Area. Expert meetings held at Garching in September presented the opportunities of the neutron source to geologists, to industrial researchers, and to membrane specialists.

The Wolfram-Prandl prize for outstanding work of young neutron scientists was awarded conjointly to Dr. Oliver Stockert and Dr. Thomas Keller, both members of different Max-Planck Institutes. Dr. Thomas Keller was given this prize for the development of TRISP, one of the FRM II instruments with unique measuring capabilities. Among all the beautiful experiments at FRM II in the course of 2006 we would like to highlight the progress which was made by Prof. Keimer's group in finding experimental evidence for electron-phonon and electron-magnon coupling, just with that instrument put up by Dr. Keller.

Politicians are curious to see how a university managed to build up and successfully operate a large scale facility. And of course the TU Munich and FRM II are grateful to politicians for their support in the never ending fight for financial and human resources. The Minister President of North Rhine-Westphalia visited FRM II with his entire cabinet on 25 September 06. Mr. Yves Caristan, head of CEA Centre of Saclay, took ideas home on how FRM II and the Garching campus are building up synergies. Prof. Fidel Castro Diaz-Balart, the son of the Cuban leader, visited the research reactor in November in order to learn more about tumor therapy by particle irradiation. On the occasion of their visit in May Prof. Mlynek, President of the Helmholtz Gemeinschaft, and Dr. Herbert Diehl from the Federal Ministry of Science promised their further support to FRM II.

Guido Engelke, who first headed the Lurgi project controller team of FRM II, was appointed Administrative Director of FRM II in the beginning of 2001 and retired by the end of 2006. His successor, Dr. Klaus Seebach, started on 2 January 2007. Like Guido Engelke he has a strong industrial background. After having studied brewing technology and having achieved his PhD in business administration, both at the TU München, he started his career in the brewing business. He became CEO of several breweries, and for a certain while also CEO of a glass manufacturer. Colleagues, users and friends of FRM II expressed their thanks to Guido Engelke during a farewell party on 20 December 2006.




Guido Engelke

Winfried Petry



Ingo Neuhaus

The year in pictures

17 March 06: Successful relocation of the first of eight instruments to be transferred from Jülich to FRM II.



15 May 06: Official farewell ceremony for Prof. Schreckenbach, Technical Director during the start-up and commissioning phase of FRM II from May 1999 until the end of 2005. (Photo: Joachim Hospe)

16 May 2006: Dr. Sebastian Schmidt, Prof. Jürgen Mlynek, the top managers of the Helmholtz Association of German Research Centres visiting FRM II together with Dr. Herbert Diehl and Mrs. Ursula Weyrich, Federal Ministry of Education and Research (from right to left, dark coats, front row). (Second row) Dr. Ulrike Kirste, Bavarian Ministry of Science, Guido Engelke and Dr. I. Neuhaus accompanied the guests on their tour through the research reactor.





23 May 2006: Visitors from the Federal Ministry of Economics and Technology: Dr. Dorothee Mühl und Mr. Jochen Süßenberger, together with G. Engelke (far left) and I. Neuhaus (far right).

9 June 06: Chief executives from industries and banking invited by the Bavarian State Chancellery to visit the Neutron Research Reactor ahead of the start of the Football World Championship 2006.

Centre group (touching the footballs, from left to right): Dr. Franz B. Humer, F. Hoffmann-La Roche AG ; Alessandro Profumo, UniCredit S.p.A.; Erwin Huber, Minister, Head of the Bavarian State Chancellery; Hans Spitzner, Vice-Minister in the Bavarian Ministry of Economic Affairs. David Martin, CEO of Arriva PLC. and Dr. Andreas Rummelt, CEO of Sandoz International GmbH.

Group at the left: Monika Oberndorfer, Invest-in-Bavaria, Bayern International GmbH, Dr. Thies Claussen, Bavarian Ministry of Economic Affairs. (Photo: Frank Röthel)



26 June 06: "The New Neutron Source Heinz Maier-Leibnitz - a contribution to strengthen the European Research Area" - Scientists and politicians attended the presentation kindly hosted by the Representation of Bavaria in Brussels.

Dr. Thomas Goppel, Bavarian Minister of Science, Research and Arts, and Prof. Dr. Ernst Winnacker, former President of Deutsche Forschungsgemeinschaft, presently Secretary General of European Research Council.

26 June 06: "The New Neutron Source Heinz Maier-Leibnitz - a contribution to strengthen the European Research Area"

Dr. Beatrix Vierkorn-Rudolph (centre), Federal Ministry of Education and Research, and Anna Lechner, Bavarian Representation in Brussels, talking with Dr. Kuch, TUM Management, and Prof. Petry (far left). (Photo: Alexander Louvet)



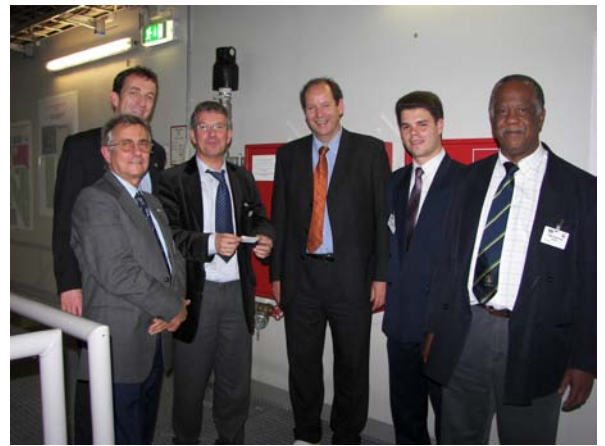
12 September 06: On the occasion of the VDI Expert Conference at FRM II: Dr. Yan Gao, General Electric Global Research, and Dr. R. Gilles, FRM II.



25 September 06: Dr. Jürgen Rüttgers, Minister-President of North Rhine-Westphalia, and his cabinet were welcomed by the TUM President, Professor Dr. Wolfgang A. Herrmann.



25 September 06: The tour guided by Prof. Petry, Scientific Director of FRM II, resulted in lively discussions in which also Dr. Thomas Goppel, Bavarian Minister of Science, Research and Arts, took part.



28 November 06: High-ranking Cuban politicians and scientists, members of the Castro family, at FRM II.



20 December 06: The entire staff says good-bye to Guido Engelke, who had worked at FRM II for 13 years; from 2002 to 2006 in his capacity as Administrative Director.

Part I

Instrumentation

1 Central services and reactor

1.1 Detector and electronics lab

I. Defendi¹, A. Kastenmüller¹, M. Panradl¹, T. Schöffel¹, K. Zeitelhack¹

¹ZWE FRM II, TU München

In 2006 most of the scientific instruments went into routine operation thus reducing the effort for commission of detector systems and electronics. While service and maintenance still were an important task of the lab, more emphasis could be gradually given to the improvement and further development of existing systems.

The launch of two new detector projects - the development of a $1 \times 1 \text{ m}^2$ fast two-dimensional position sensitive detector for the new small-angle scattering instrument SANS1 and the development of a 1 mm resolution 2D-detector for the diffraction instrument StressSpec - as well as the development of an individual channel readout system for a fast Multi-Wire-Proportional-Chamber within the NMI3-JRA2 (MILAND) joint European project took broad room in our activities.

scientific instruments using our DAQ-system with the board for the purpose of monitoring the installed ^3He -detectors and beam monitors.

The NMI3-JRA2 (MILAND) project is dedicated to the development of a fast, medium resolution ($\approx 1 \text{ mm}$) 2D-neutron detector. The lab contributes with the development of a readout system for 320×320 individual channels of a fast MWPC depicted in Figure 1.2.

Each cathode wire is connected to a transimpedance amplifier followed by a comparator that generates a Time-Over-Threshold (ToT) signal. 32 channels are integrated into a MILAND32 Card developed at ILL [2], that is directly plugged to the rear side of the MWPC. The TTL-output signals are sent to the digital processing unit consisting of 2×3 Pre-Processing Modules (PPM) and a CORrelation Mod-

ule (COM) implemented in a standard VME64x crate with custom backplane utilization. Both PPM and COM consist of a common FPGA-based board developed at FRM II with specific FPGA design and a piggy board shown in Figure 1.3. The PPM-piggy board consists of digital front-end buffers, whilst the COM-piggy board implements a fast Ethernet interface. The ToT-signals are acquired by the processing block in charge of recognizing a cluster of signals and determining the position according to a well defined algorithm (signal arrival time, longest ToT, ToT based averaging). The X and Y coordinates are then correlated in time and formatted data are sent to the DAQ system by the transport block. A set of 3 prototype boards has been built and successfully passed the hardware tests. Presently, the VHDL-implementation of the algo-

Detector readout electronics

During the previous years we developed various PCI/cPCI-based detector DAQ-boards using the M-module standard for applications like neutron counting, Time-of-Flight measurement or Multi-Channel scaling [1]. In 2006 a further module implementing a 2-channel Multichannel analyzer (MCA) was added. The board features:

- 12 bit peak sensing ADC
- 2 input channels; range 0 - 4096mV
- selectable input polarity
- selectable modus: gated / ungated / sampling

Figure 1.1 shows a pulse height spectrum of a ^3He -neutron detector produced by thermal neutrons from a ^{252}Cf -source recorded with the MCA-module. We gradually will equip the

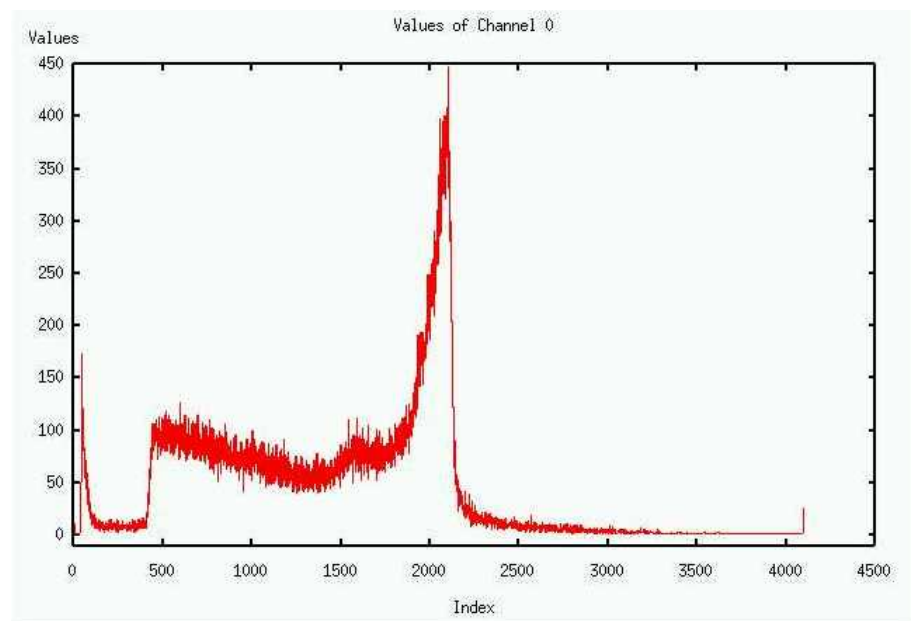


Figure 1.1: Pulse height spectrum of thermal neutrons recorded by the MCA M-module

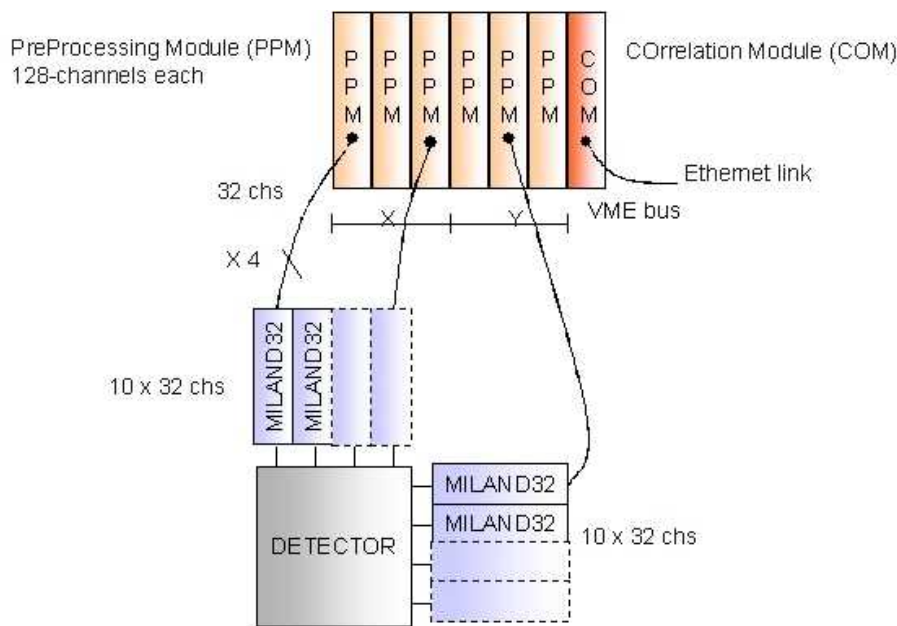


Figure 1.2: Readout scheme of the MILAND detector

gorithm to determine the neutron impact position is in progress.

Detectors

A 2D-position sensitive detector with $1 \times 1 \text{ m}^2$ active area, $8 \text{ mm} \times 8 \text{ mm}$ position resolution and 1 MHz global count rate capability is planned for the new small-angle scattering instrument SANS1 which is presently under construction. After an evaluation of various alternatives, a linear array of 1 m long position sensitive ^3He -detectors (diameter $d = 8 \text{ mm}$) is regarded as most favorable configuration similar to the D22 detector at ILL. With very helpful support by the ILL detector group the

following two prototype detectors have been investigated end of 2006 in neutron beams of $\lambda = 9.7 \text{ \AA}$ and $\lambda = 22 \text{ \AA}$ respectively at the instrument MIRA.

- 8 Reuter Stokes P4-0341-201 ^3He -PSD's ($L = 1 \text{ m}$, $d = 8 \text{ mm}$, $p_{\text{He}} = 15 \text{ bar}$) arranged as linear array
- A "multitube" ^3He -PSD consisting of 32 tubes ($L = 1 \text{ m}$, $d = 7.4 \text{ mm}$, $p_{\text{He}} = 15 \text{ bar}$) with common gas volume built by the ILL detector group

Figure 1.4 shows the prototype built of individual PSDs mounted in the collimated beam at MIRA with a remote controlled slit in front of the device.

A fast electronics for PSD's developed by the ILL detector group

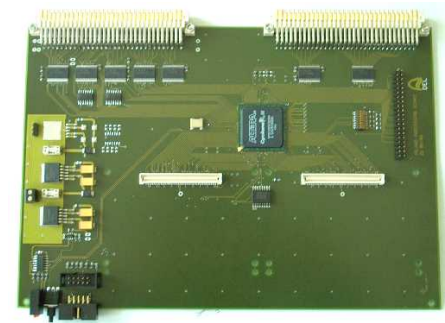


Figure 1.3: The MILAND Pre-Processing (PPM) / Correlation Module (COM)

Figure 1.4: A SANS1 prototype detector built of individual ^3He PSD's mounted at MIRA

was used to read out both prototype detectors. As a first preliminary result, both devices fulfill the requirement of a position resolution $\Delta x < 8 \text{ mm}$ for neutrons of both wavelengths and a high rate capability. A more elaborate analysis of the measurements is in progress.

[1] Zeitelhack, K., *et al.* *FRM-II annual report 2003*, 6–7.

[2] Guerard, B., *et al.* *NMI3-JRA2 annual report 2005*, 19–21.

1.2 HELIOS – polarized ^3He gas for neutron instrumentation

S. Masalovich¹, O. Lykhvar¹, G. Borchert¹, W. Petry^{1,2}

¹ZWE FRM II, TU München

²Physik Department E13, TU München

In 2006 HELIOS, the facility for large-scale production of highly polarized ^3He gas, has been fully operational throughout the year in spite of the lack of one laser for a longer period. Usually the optical pumping at HELIOS is

performed with two high-power lasers, but because of faulty performance one laser has been sent back to the company for revision. To be able to polarize ^3He gas to a high polarization state with only one laser, the optical scheme

of the setup was modified and some components were improved. In particular, the problem of degradation of the gas polarization because of instability of the laser beam polarization has been identified and new optical compo-

nents have been installed to eliminate this problem. As a result of all of these modifications, ^3He gas polarization was kept at a high level of around 76% with only slight reduction in the production rate. Finally, in autumn 2006 the second laser has been put into operation again and since then the ^3He gas polarization about 82% can be reached in the optical pumping volume.

Experiments at neutron instruments

This year experiments with the use of polarized ^3He gas have been performed at three instruments at the FRM-II: TRISP, MIRA and HEIDI.

At TRISP (the spin echo triple axis spectrometer) a Neutron Spin Filter (NSF) with polarized ^3He gas was used as an analyzer in the measurements with neutrons of wavelength 1.795Å. The NSF cells with 80 mm neutron flight pass and 2 bar gas pressure were provided for these measurements during 8 days with daily replacement. The cells were positioned in the center of a rectangular solenoid developed at TRISP and designed to implement the polarized ^3He gas.

This solenoid was located in one of the zero-field arms at the instrument. The gas polarization in the freshly replaced cell on the neutron beam was measured to be about 64% and the relaxation time of gas polarization was estimated as 60 hours.

At MIRA (the beam line for very cold neutrons) the test measurements have been performed with neutrons of wavelength 9.7Å to verify the ability to use NSF cells in neutron reflectometry as well as in small angle scattering experiments with polarized neutrons. The aim of these measurements was to check the pattern of neutrons scattered by an empty quartz cell, which supposed to be used with polarized ^3He gas at MIRA. The requirement for such NSF at any reflectometer (SANS as well) is quite obvious – it has not to scatter neutrons at small angles. To check how the quartz cell fits this requirement two measurements have been performed at MIRA.

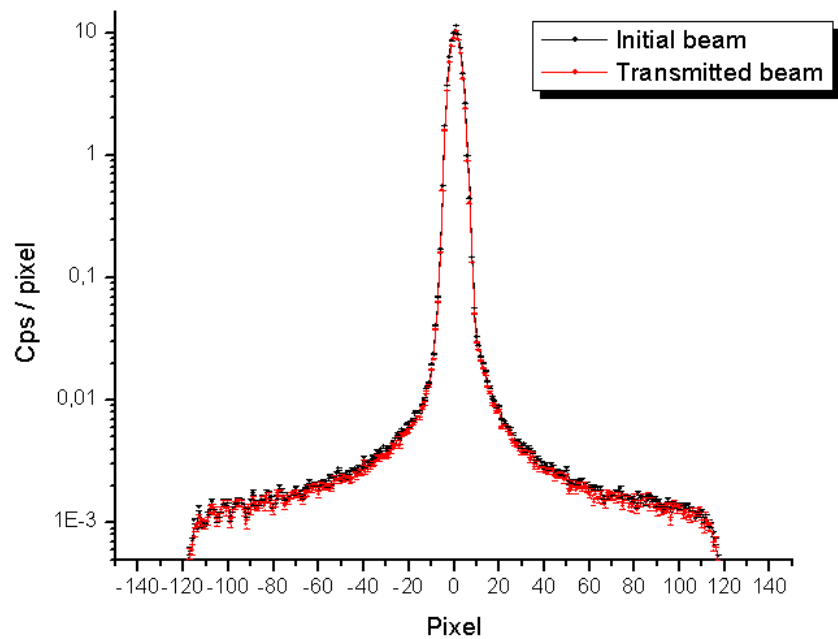


Figure 1.5: Measured intensity distributions across the neutron image with and without empty quartz cell in the beam at MIRA

First, a slit mask has been used to prepare a narrow neutron beam (3x25mm) and the image of the profile of this beam has been recorded with a 2D detector located at the distance 1.2m from the mask. Then an empty quartz cell was placed into the beam behind the mask and the image was recorded again. Two curves in Fig.1 represent the scans across the neutron beam images in both cases. One can see a typical count rate decrease because of scattering by the quartz cell (measured transmittance is 0.90 at this wavelength), but there is no visible small angle scattered neutrons. So, one may conclude that neutrons are scattered in a large solid angle (isotropic scattering) and one may neglect their contribution to the angular distribution measured in the real experiments at MIRA (at least down to the order of 10^{-4}).

To provide the ability to use polarized ^3He gas at MIRA a circular solenoid with compensated ends has been built at the Neutron Optics group. Design of this solenoid allows installing it inside the mu-metal box at MIRA. This box serves to screen the internal area against environmental magnetic fields and thus ensures a long lifetime of a NSF. The re-

laxation time related to the magnetic inhomogeneity of the assembled unit was estimated to be $T_1 = 200$ hours at 1 bar gas pressure. A preliminary imaging experiment with polarized neutrons has been done using a NSF with 0.25 bar gas pressure. The cell with such pressure yielded a relaxation time of only 35 hours. For future experiments it was decided to build special thin cells optimized for the neutron wavelength range at MIRA.

Whereas TRISP and MIRA have their integrated polarizers and NSF with polarized ^3He gas can be used mostly as analyzer, an experiment with polarized neutrons at HEIDI (the single crystal diffractometer with hot neutrons) relies entirely on the use of polarized ^3He gas. Two NSF cells are presumed to be in use. The first NSF cell serves as a polarizer and the second one as an analyzer. To check the feasibility of this approach, scientists at HEIDI developed two magnetostatic cavities to ensure a long lifetime of the polarization in the NSF cells at the environmental magnetic field of the instrument. Some preliminary measurements with NSF cells have been performed in the summer with neutrons of wavelength 0.55 Å and

0.87 Å. The whole setup assembled with MuPAD has been tested in the autumn of 2006. The experiment was running for a week with neutrons of wavelength 1.165 Å. Two NSF cells with 130 mm neutron flight pass and 1.65 bar gas pressure were provided for this experiment. A few replacements of the cells have been done in the course of measurement. The gas polarization in the freshly replaced cells on the neutron beam was measured to be about 70% and the relaxation time in each cell was estimated as 100 hours.

Neutron spin filter cells

Seven new cells for Neutron Spin Filters have been built in the year 2006. Thus, on the whole there are nine cells of different sizes currently available for neutron experiments. The cells are made of high purity quartz glasses HSQ 300 and HOQ 310. All cells have been finished (cleaned and coated with pure metallic cesium) by the Neutron Optics

group and showed relaxation time ranging from 100 up to 200 hours.

It is known that NSF cells suffer from the leaks that may appear in the grease-sealed glass valves attached to the cells. Such leaks lead to an oxidation of the metallic cesium inside the cell with subsequent degradation of the relaxation time. The risk of leakage increases with time since the grease has a tendency to get thinner with increasing number of valve operations. Finally the grease film may be broken and leaks arise. To be able to change the grease in advance, a special vacuum-tight glove box (see Fig.2) has been designed and built by the Neutron Optics group. This glove box can be evacuated and filled with pure ^4He gas to ensure oxygen-free environment for valve reinstallation.

In addition, a systematical study has been made by the Neutron Optics group with the aim to improve the reliability of the valves. As a result it was proposed to use a special wax for vacuum sealing instead of grease. The wax has a softening point about 50 – 60 °C and the valve

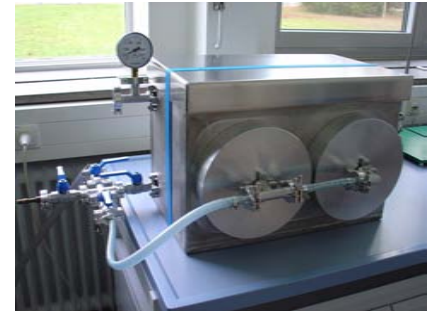


Figure 1.6: Glove box in the cell preparation lab

sealed with such wax can only operate after slight heating. At room temperature the wax becomes solid and ensure high reliable sealing even for the cells with the elevated gas pressure. It was shown that effect of the wax on gas polarization is almost identical with that of the generally accepted grease.

The work on the preparation of new cells will be continued next year along with designing of new magnetostatic cavities for better performance of Neutron Spin Filters at neutron instruments.

1.3 REACTOR - Calibration of the control rod of the FRM II in the subcritical regime

K. Schreckenbach¹

¹Physik Department E21 and ZWE FRM II, TU München

For the performance and safety of a nuclear reactor the reactivity worth calibrations of the control and shut down rods are of major importance. The experimental verification of the calculated values are also a valuable benchmark for the validation of the programs used.

The FRM II is equipped with a control rod in the centre of the light water cooled fuel element and five shut-down rods in the surrounding heavy water reflector. For routine operation all shut down rods are withdrawn and the reactor is stabilized by the control rod from the top. With the control rod fully inserted the reactor is subcritical with a high safety margin. In the present report the safety margin is deduced from

measured data and compared with calculations.

The shut down reactivity for the inserted control rod was determined during the start up of the reactor by extrapolation of the reactivity worth measured above the critical position. A more quantitative measurement is the drop rod method or the calculation from the subcritical neutron counting rates. In the present report the subcritical counting rates are evaluated.

In the subcritical regime the fuel element serves as a neutron amplifier of an external neutron source. During the first criticality a Cf-252 neutron source was used. For an already irradiated core the photo neutrons serve as primary neutron source.

For a neutron source S_0 with the

same distribution as the neutron induced fission reactions and for the point kinetic approximation the neutron density $n(x)$ as function of control rod position x is related to the neutron multiplication factor k by

$$n(x) = \frac{S_0}{1 - k(x)}$$

$$k(x) = 1 - \frac{S_0}{n(x)}$$

$$S_0 = -\frac{dk}{dx} / \frac{d(\frac{1}{n})}{dx}$$

The reactivity ρ is related to k by $\rho = (k - 1)/k$. In one of the cases discussed here, the reactor core was already used and photo neutrons were produced by gamma rays from the core in the heavy water. Criticality occurred at a higher

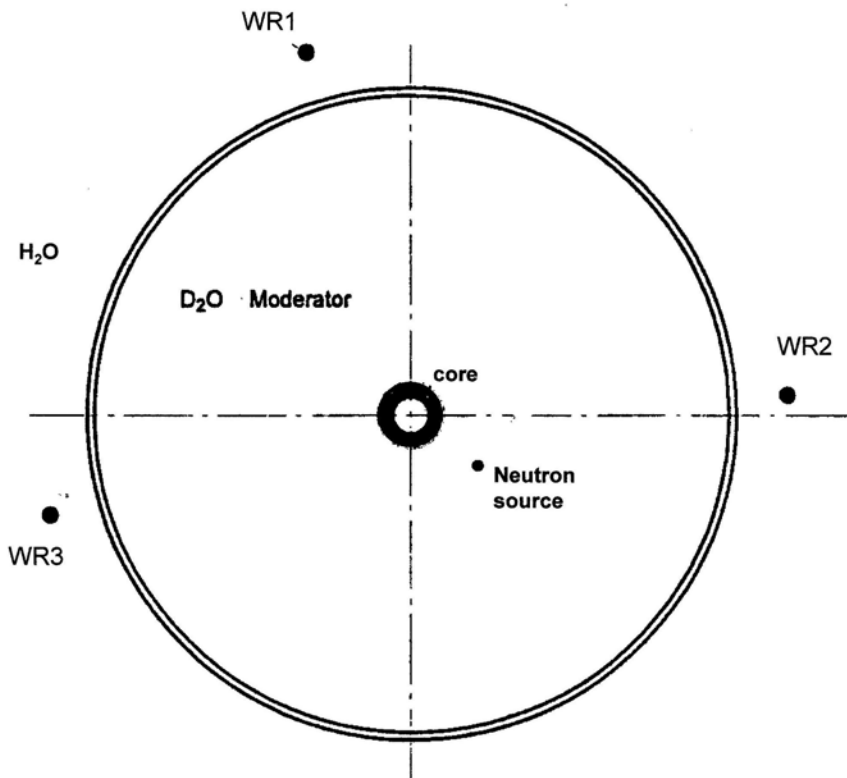


Figure 1.7: Schematic cross section of the reactor with start-up neutron source and the wide range neutron detectors WR.

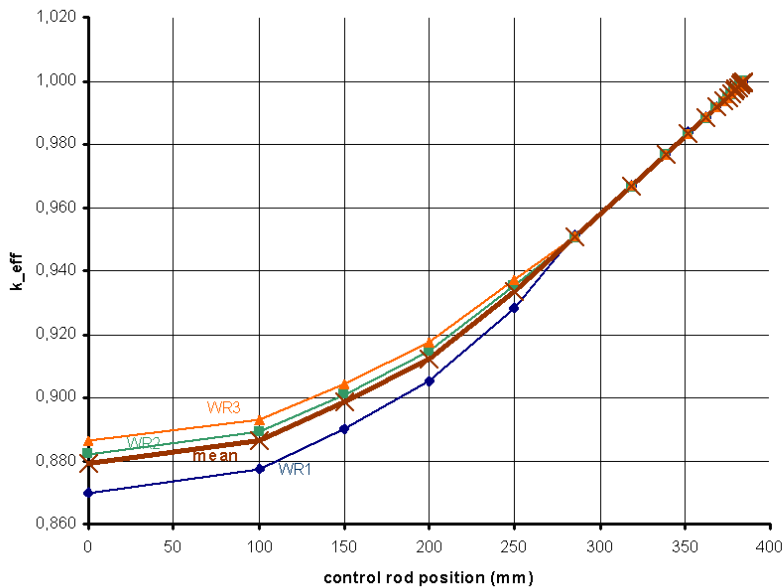


Figure 1.8: Multiplication factor as function of the control rod position for the photo neutron case.

control rod position (384 mm) compared to a fresh fuel (340 mm). For this case the above prerequisites are fulfilled approximately and the unknown parameter S_0 (here photo neutrons) can be determined from the derivative dk/dx as measured for the fresh core with the critical reactor at 340 mm.

The neutrons were counted in wide range detectors (WR) surrounding the heavy water vessel (see Fig.1.7), the counting rate $c_i(x)$ being proportional to $n(x)$ in the point kinetic approximation. The result is shown in fig.1.8. The middle plane of the core is at level 410 mm.

With the Cf-252 neutron source placed outside the core the geometry (see Fig. 1.7) does even not approximately fulfil the above prerequisites. On the other hand the counting rates $c_i(\text{dummy})$ in the wide range detectors WR were measured with a fuel dummy and the neutron source in place. Thus an approximate evaluation is possible by modifying the above equations to:

$$c_i(x) - c_i(\text{dummy}) = c_i(0) \cdot k / (1 - k)$$

The counting rate $c_i(0)$ corresponds to the part from the neutron source which reaches the fuel element and is amplified. The value of this parameter can again be deduced from the derivative dk/dx close to the critical point.

For the photo neutron case the data agree within the uncertainty with the calculation of A. Röhrmoser (FRM II) (estimated uncertainty for calculation and measurement of dk/dx in total 15%). For the radioactive neutron source the maximum deviation was less than 0,02 in k at $x = 0$ (shut down). It must be emphasized that the shut down reactivity margin of the control rod for a fresh fuel element is about $\rho = (k - 1)/k = -0,12$ and high compared to -0,02 required by regulation. Thus the present evaluation is a methodical investigation and not a necessary proof for safety of the FRM II.

1.4 Sample environment

J. Peters¹, H. Kolb¹, A. Schmidt¹, A. Pscheidt¹, J. Wenzlaff¹, P. Biber¹

¹ZWE FRM II, TU München

In March 2006, ACCEL Instruments, Germany, delivered our cryogen free super-conducting magnet. The magnet provides a maximum magnetic field of 7.5 T and a room temperature bore of 100 mm diameter. Further specifications are: split 30 mm, horizontal beam access 320°, split angle 3°. A motorized rotation stage located at low stray field level is available which allows rotation of sample environment. A second rotation stage developed in house is under construction and available in early 2007. Subsequent to intense laboratory tests a test run was accomplished on the cold three axes spectrometer PANDA in November 2006. All tests revealed a stable and reliable running system. Some further improvement must be done e.g. rotary feedthrough adapters to uncouple circular motion of magnet and cryostat from stationary flex lines.



Figure 1.9: 7.5 cryogenfree magnet

1.5 Neutron flux values/spectra at operating FRM II

A. Röhrmoser¹

¹ZWE FRM II, TU München

Neutrons designed for usage at FRM II

The Year 2006 was the first year full with routine operation of FRM II. Five cycles of full burn-up with 1040 MWd each were reached.

History within a few words

Core

The neutron physical behavior of the core during this first full operation showed up to be exactly or at least extremely close to the theoretical descriptions of the reactor design studies, that

were done now more than a decade ago (in the 1980's [1, 2]). The integral properties of the reactor were calculated with a cylinder-symmetric description of the core and its surrounding. For the core reactivity and burn up predictions one can reach excellent results that way as verified by reality.

The design was done with the assumption of a disturbance by the at that time unknown user installations (UI) of 4% absolute in k_{eff} and a necessary reserve in k_{eff} of 2% to cover all uncertainties of the calculation or even fabrication tolerance factors.

User installations (UI)

Mid of the 90's the design task shifted totally to the need of secondary source design. That way one tried to find the most appropriate arrangement for the beam tubes and the cold (KQ) and hot source (HQ) in the D₂O-moderator vessel [3]. All the 10 horizontal tubes and one of the two vertical ones were realized very close to the outlines of this design phase. More remarkable changes were only made later at the tubes facing the cold source in height and width. Further thinner walls have been realized at the close core neighborhood.

With this design model of user in-

stallations (3Dmodel96) there were predicted:

1. the decisive flux of neutrons at the noses that can enter the beam tubes for the usage at experiments (s. below) and
2. the disturbance on the core reactivity itself.

This design model 3Dmodel96 had a rather simplified core, thus being fully qualified for the 'beam tube layout'. But also reactivity disturbances could be evaluated pretty well. It was calculated a disturbance of the reactor in k_{eff} of 5.6%, thus practically consuming the bulk of reserve in reactivity of the core design calculations.

As-built model of user installations and core

At the beginning of the new millennium the core was realized with all its beam and irradiation tubes. TUM created a quite new 3d model of the core and D₂O-tank content. This model 3Dmodel2k took care of all the 'as-built'-data, that were comprehended very diligently. Again the core itself was modeled 3d with the involute plates structure. The output of these new 'as-built' calculations was now:

1. The absolute core reactivity is very close to the results of the 2d-core design calculations without UIs and thus confirming late 3d-results of '99 [4], too.
2. The disturbance of the reactor in k_{eff} was at 5.0% with 'as-built' UI-structures, thus consuming exactly half of the design reserve to reach certainly the aimed 52 full power (FPDs) operation at 20MW of the core design studies. The regain of reserve was mainly because of the thinner beam tube front parts and less expressive assumption on absorption of unknown structure additives. Besides, this is in absolute agreement to the reserve that the reactor shows in reality with the remaining control rod margin after operating a full cycle of 52 FPDs.

FRM II/E7, TEB, KQ kalt, r=2cm tally, MOL
 MCNP4C / 41*41 Fluss-Maschen Hoehe: -5.cm
 bei 20.0MW th. / EV= 0.9994/STS= 10.00

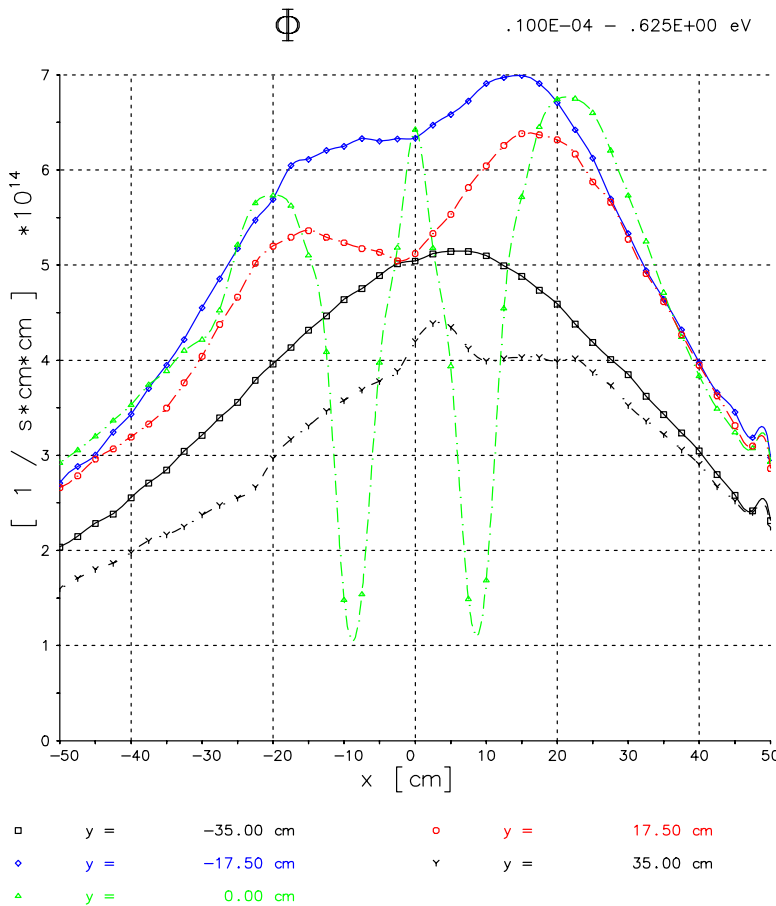


Figure 1.10: Thermal n-flux Φ_{th} , cuts at const y-value. The dots are the centers of flux tally bowls, lines are given to guide the eye.

Thermal flux distribution in the D₂O-tank

As a side product of the new core model one could even produce a 3d-flux map of the core surrounding. The program version MCNP5, that inherently supports this feature, was not obtainable to European users till 2007, but it could be done an adaptation to version MCNP4C. Vertical asymmetries can be also obtained in 2d-symmetry, but here one can especially predict azimuthal asymmetries in the flux distribution, too. Again the axial flux distribution in the D₂O-tank will be describable most exact.

To obtain a best representable value over the cycle a calculation was done with the 3Dmodel2k at about mid of the operations cycle (MOL). Figures 1.10 (and 1.11) show Φ_{th} in the core surrounding 5 cm below core mid plane. There are given five cuts at constant y position in the reactor. As structure easily conceivable is mainly the core itself, which is cut two times at y=0 cm (sharp flux dips). The maximum flux in the D₂O is obviously of exactly $7.0 \cdot 10^{14} \text{ cm}^{-2}/\text{s}$. At the opposite side of this maximum point the cold source

FRM II/E7, TEB, KQ kalt, r=2cm tally, MOL
 MCNP4C / 41*41 Fluss-Maschen Hoehe: -5.cm
 bei 20.0MW th. / EV= 0.9994/STS= 10.00

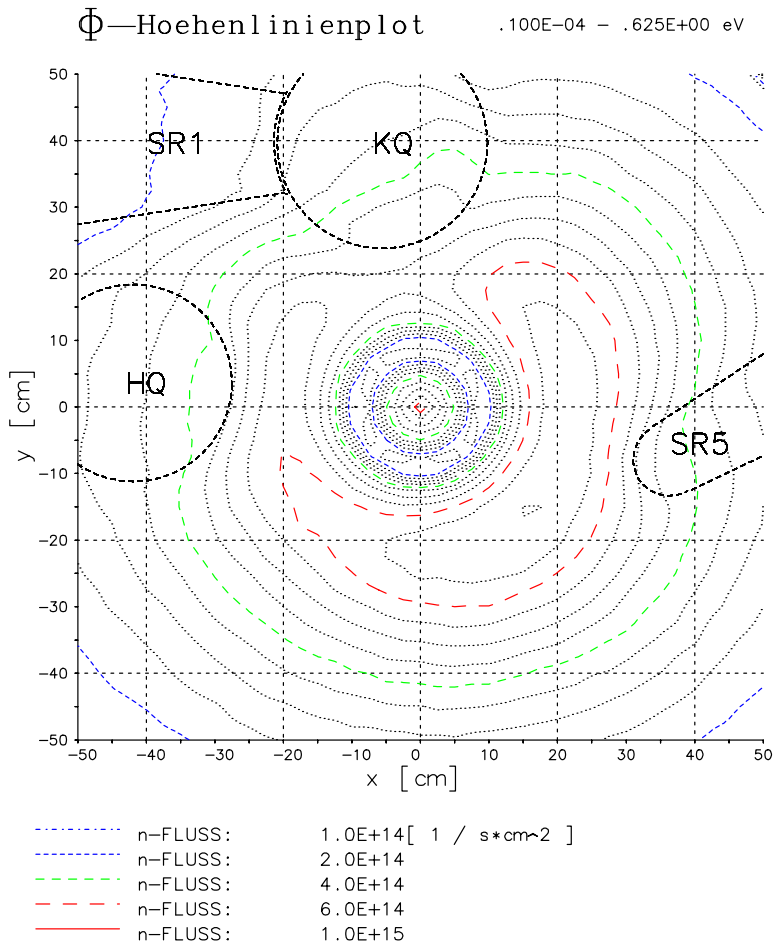


Figure 1.11: Thermal n-flux Φ_{th} obtained with a 3Dmodel2k calculation 5 cm below core mid plane at about mid of the operations cycle (MOL). Same data are used as in Figure 1.10, but now a full 2d-map is drawn. The hot source HQ, the cold source KQ, the beam tubes SR1 and SR5 are shown, the latter showing nearly exact onto the maximum of the thermal n-flux Φ_{th} at FRM II. All four installations influence the thermal flux distribution in their surrounding. The very strong flux depression in the center results from the cylindrical fuel element itself.

with its huge beam tubes has depressed the flux to a lower flux level, what is more impressive shown in the 2d-flux map figure. The cold (and hot) source and some beam tubes, which are cut here, are sketched also in the picture. Some of the beam tubes produce a kind of a fingerprint in the flux map as best conceivable here at SR1 and SR5. The latter tube penetrates nearly direct into the flux maximum (cmp. below).

As a rough estimation from the former 2d-symmetric contemplations at full thermal power $P_o=20$ MW it was predicted a flux level of $\Phi_{th}^{max,az.-avg.} =$

$6.5 \cdot 10^{14} \text{ cm}^{-2}/\text{s}$, averaged at $r=22 \text{ cm}$

Φ_{th} (bowl, r=5cm) 10cm thick before nose of beam tube nose [$10^{14} \text{ cm}^{-2}/\text{s}$]						
	BOL, Φ_{th}	rel. error	BOL, Φ_{th}	rel. error	EOL, Φ_{th}	rel. error
	model 96		as-built		as-built	
SR3	3,27	3,1%	3,06	0,28%	3,57	0,26%
SR5	5,66	2,6%	5,49	0,21%	5,63	0,20%
SR7	5,45	2,1%	4,91	0,22%	4,45	0,23%
SR8	4,82	2,8%	5,06	0,22%	4,58	0,23%

Table 1.1: n-flux Φ_{th}^{nose} before the beam tubes obtained with the 3Dmodel96 for BOL and the 'as-built'-model 3Dmodel2k for both BOL and EOL. The 'rel. error' is the statistical one.

over the 360° azimuthal angle. This is fully confirmed here.

Flux at thermal beam tubes SR3/5/7/8

For any user the output at the beam ends is decisive, not the flux at the nose Φ_n^{nose} . But in fact the output must be regarded rather proportional to the input Φ_n^{nose} .

With the design model 3Dmodel96 and the fresh fuel element (begin of life, BOL) the following Φ_{th}^{nose} values are calculated: $5.5 \cdot 10^{14} \text{ cm}^{-2}/\text{s}$ for the two beam tubes SR5 and SR7, nearly $5 \cdot 10^{14} \text{ cm}^{-2}/\text{s}$ for beam tube SR8 and more than $3 \cdot 10^{14} \text{ cm}^{-2}/\text{s}$ for tube SR3.

With the new 'as-built'-model the corresponding values are expected to be rather close to the old calculations. The values of the table confirm this and only SR7 is clearly outside the statistical error (3%) of the former ones. The values can be given as follows:

SR5 with $5.5 \cdot 10^{14}$, SR3 with $3 \cdot 10^{14} \text{ cm}^{-2}/\text{s}$ and both SR8/7 at $5 \cdot 10^{14}$. An explanation for the lower value for SR7 must be searched in the modified beam tube, especially at the nose, which is built more stocky; this has a major effect only on the flux in the control volume at the nose and does not mean less streaming into the beam to the user exit.

Because the situation BOL is a somewhat extraordinary situation with the control rod in the lowest position and moving strongly upward over the first 2 days (Xe poisoning) of nominal power operation, the averaged values Φ_{th}^{nose} over the typical cycle life time are of more concern for the user. The Figure

1.12 shows the values from Table 1.1 for BOL and compares them to the corresponding values $\Phi_{th}^{nose,EOL}$ from a calculation with a control rod positions STS as for the operational state EOL.

SR3 must obtain a significant gain in flux during reactor operations cycle. SR5 gains again a few %, but the two low lying tubes SR7 and SR8 have their highest flux at BOL (10% higher than at EOL).

[1] Böning, K., Gläser, W., Röhrmoser, A. In *RERTR Conference 1988 (1988)*.

[2] Röhrmoser, A. *Neutronenphys. Kernausslegung FRM II*. Ph.D. thesis, TUM (1990).

[3] Gaubatz, W. *Rechnerische Optimierung der sekundären Neutronenquellen des FRM-II*. Ph.D. thesis, TUM (1999).

[4] Petrov, Y., Onegin, M., Böning, K. In *Gatchina-Garching (2001)*.

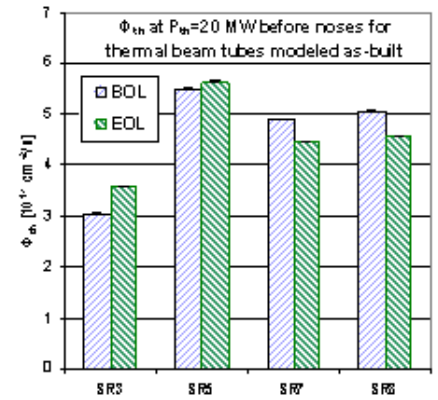


Figure 1.12: Φ_{th}^{nose} after the calculations with the 'as-built'-model for the extreme operational states with control rod positions STS time for BOL and EOL. The averaged value must be seen a little bit more close to the state EOL than BOL. A sketch of SR5 is also shown in Figure 1b. SR3 is above and SR7 and SR8 are below the core mid plane.

1.6 Reduced enrichment for FRM II

A. Röhrmoser¹, R. Jungwirth¹, W. Petry¹, W. Schmid¹, N. Wieschalla¹

¹ZWE FRM II, TU München

There are intense and widespread international efforts to develop very high density fuels for research reactor concepts with reduced enrichment. TUM is fully engaged here, too, and became a member in the 'International working group for high density fuel development' in 2006.

There exist mainly two pathways that are investigated intensively.

1. Dispersive fuel in Al matrix and Al cladding: instead of the currently used powders as U_3Si_2 in case of FRM II one regards mainly UMo alloys. The powder can be produced with the grinding method or with an atomizing process. The percentage of Mo can be chosen free with the alloy and varies between 6 - 10 wt %.
2. The more progressive pathway with the same material UMo alloys but not dispersed or mixed with a matrix but in form of a monolithic foil. The foils have

to be cladded as usual. One of the main challenges with this very high density fuel is the fabrication of full size plates with fine and resistable bonding.

By means of collaboration with the French CEA, the fuel fabricant AREVA-CERCA, TUM contributes in both fields to find ways of progressing the fabrication and the irradiation behavior of this fuel.

Besides the technical problems with fuel fabrication and plate production it was followed a quite new conceptual study with the monolithic fuel on base of a thickness variation of the fuel layer. The results (s. below) were presented in April and June on RRFM-06 and at an IAEO-meeting on invitation by the Norwegian government.

Fuel irradiation program

For the first irradiation program it was decided to irradiate four test

plates of full size at the MTR reactor OSIRIS/Saclay. For this purpose six plates were produced by CERCA with UMo-Al dispersive fuel (8% wt. Mo) at 50% enrichment. The uranium densities were 7 and 8g/cm³. Two of the 8g/cm³ plates contain a Si additive, a possible considerable "diffusion blocker". Before starting irradiation OSIRIS needed an extension of its license for heat flux values in the order of 300 W/cm² for the TUM plates to reach a targeted cladding surface temperature of 100°C. After some delay with the nuclear licensing the irradiation could finally start Sept. 2005 with four plates in two different IRIS devices. Meanwhile all four plates have reached the aimed density of $2.3 \cdot 10^{21}$ fissions/cm³. This value covers any obtainable level in a future fuel element for FRM II.

Motivated by the conservative swelling behavior two plates were irradiated to higher fission densities. Meanwhile, one of the plates

has reached a fission density of $3.4 \cdot 10^{21}$ fissions/cm³ and still no anomalous swelling is observable.

Due to the radioactive load post-irradiation examinations (PIEs) of the irradiated plates have to wait until mid of 2007. The plates now are already shipped for investigations to CEA Cadarache.

UMo-monolithic fuel research cooperation

For the more progressive pathway there were collected a lot of new results by the RERTR program in 2006 so that the very thin data base till 2005 on irradiation behavior is now extended remarkably. Major results can be summarized as follows:

1. The swelling of the 'monolithic' fuel itself shows up on a very comparable scale to the dispersive variant.
2. The problem interface switched from the particle surface to the UMo/Al-clad interface. Here a variety of problematic behaviors showed up and obviously very dependant on the different processes for bonding the UMo-foil to the clad.

Since 2005 TUM is in a 'Cooperation in development for UMo-monolithic fuel plates' with French CEA and CERCA. In the frame of the so called IRIS5 experiment full size plates shall be produced and a common TUM/CEA/CERCA irradiation experiment will be launched as soon as available at OSIRIS with two plates. To overcome the bonding problems, the CERCA/TUM cooperation investigates new ways of bonding the UMo foil to the clad.

Core design calculations with UMo monolithic fuel

With the availability of UMo monolithic fuel the uranium density in the fuel layer can be increased drastically to the maximum of 15-16g/cm³, only slightly dependent on the Mo percentage variation.

Regardless of the technical feasibility to produce large monolithic fuel

plates, former studies with continued. The conditions for a possible conversion scenario are that the power level has to be kept at 20 MW, the cycle length has to be maintained at at least 52 days, only marginal losses in neutron flux and neutron quality, similar safety margins and no essential increase of fuel costs.

A first trial with monolithic fuel plates, the thickness of which changed step-like at a certain radial width in order to avoid unacceptable heating at the outer fuel side, showed up to be very unfavorable. At a level of 34 % enrichment more than 40 kg Uranium (14 kg U-235) had to be used and the local maximum power turned out to be larger by 20 % compared to the actual U_3Si_2 element.

The idea was now to introduce a *continuous gradient in fuel thickness*. One key reason is, that a step gradient in U density as currently used is not feasible with monolithic fuel at all. Again the U²³⁵ amount has to be led to a practical value at about 10 kg or even below. All the demanded aims were achieved now.

With those studies of radial continuous variation of fuel layer thickness the power distribution could be progressed very much. Fig. 1.13 displays the radial thickness variation of the uranium foil and the radial heat form factor in a comparison to the currently used fuel element. The heat form factor is remarkably better than even with the current core of relative low density. Only 9.1 kg of fissionable material U²³⁵ are needed. The maximum thermal flux is depressed by 9% over the whole cycle when compared to the actual HEU fuel at the same thermal power of 20MW.

The solution opens some other opportunities for parameter studies. Not all of them were followed up to last extent in the moment, since the solution is afflicted with to many unknowns, but to give an example:

With a thicker meat, lets say 300μm instead of 250μm and the same thickness shaping in this calculation, the total output on FPDs would be extended by about 20%.

Metallographic studies

The build up of the harmful UMo-Al interdiffusion layer (IL) at the surface of the UMo powder or foils during irradiation has to be better explained.

In a quite new approach TUM irradiated UMo samples by the domestic heavy ion facility in order to distinguish between physical processes, that are regarded to be responsible for the harmful buildup. In contrast to in-pile irradiations the samples can be studied easily by all kind of metallurgical methods and without time delay, what makes the procedure fast and less expensive. First results of measurements on thermal conductivity of those samples before and after beam bombardment were gathered in a diploma thesis, too.

The approach was followed by the French CEA in their efforts to explain and distinguish between different UMo fuel powder and additives.

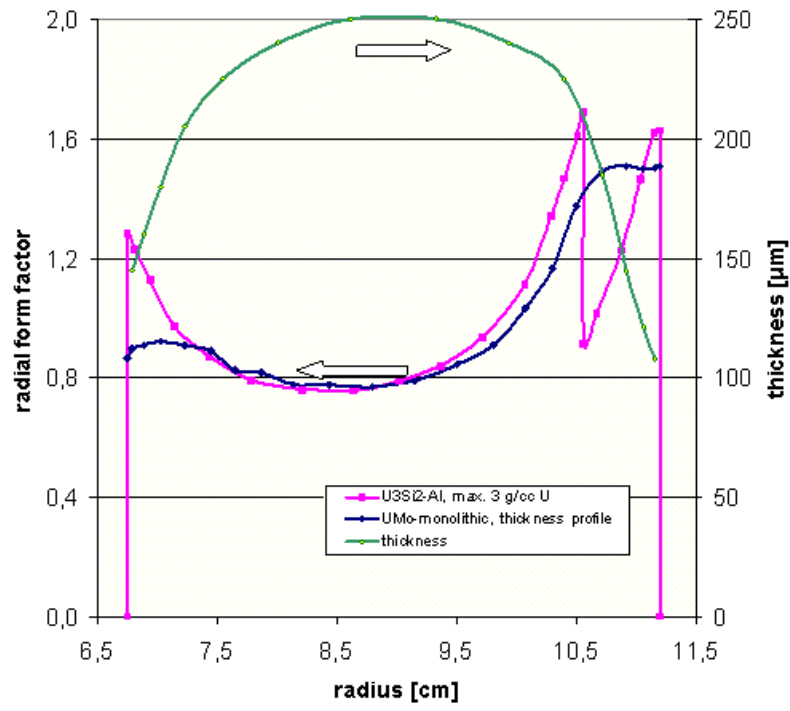


Figure 1.13: Calculated radial power form factors (left scale) in FRM II at BOL with U_3Si_2-Al HEU fuel as currently and with the newly studied UMo monolithic MEU fuel. The thickness of the monolithic fuel layer is variable and up to $250\mu m$ in the central region (right scale).

2 Thin films and large scale structures

2.1 KWS-1 and KWS-2 Small-Angle Neutron Scattering Diffractometers

H. Frielinghaus¹, A. Radulescu¹, P. Busch¹, V. Pipich¹, E. Kentzinger², A. Ioffe¹, D. Schwahn², R. Hanslik³, K. Dahlhoff³, M. Heiderich², G. Hansen³, D. Richter^{1,2}

¹JCNS, Research Centre Jülich, outstation at FRM II

²IFJ, Research Centre Jülich

³ZAT, Research Centre Jülich

With the shut-down of the Jülich reactor FRJ-2 all high-performance instruments started to move to the Munich reactor FRM II. The two Small-Angle Neutron Scattering diffractometers found a space at the very end of the neutron guide hall and partially in the ring laboratory of the old FRM-I reactor. The following setup should split the large number of possible experiments to the two SANS diffractometers. KWS-1 should be optimized for high resolution, GISANS, and polarized neutron experiments, whereas KWS-2 should be optimized for high intensity. Thus, all extraordinary requirements should be served by KWS-1, whereas conventional and high intensity requirements should be served by KWS-2. A continuous upgrading will bring KWS-1 and KWS-2 to the same state in a moderate future. While the old state of the instruments was rather conventional, the new techniques of this refurbishment will meet the requirements of world leading scientists. These things are described in the following:

Polarization and He³ filter for analysis

Transmission neutron polarizers are optimized for maximum transmission at 4.5, 7 and 14 Å. To keep the neutron beam polarization along the collimator the neutron guiding elements are coated with non-magnetic $m = 1.4$ NiMo-Ti supermirrors. Polarization analysis of the scattered beam will be carried out by a He³ neutron spin filter of 15 cm diameter immediately behind

the sample. The filter will be placed in vacuum and the direction of the He³ nuclear polarization will be controlled by the adiabatic fast passage method.

Neutron lenses

Neutron lenses will become a standard for SANS diffractometers now. Quite frequently spherical biconcave MgF₂ lenses with a diameter of approx. 3 cm are being used [1]. We will install MgF₂ parabolic lenses of 5.2 cm diameter in order to avoid spherical aberration and make use of the whole beam area given by the neutron guide [2]. The lenses will be placed in vacuum inside the collimator just in front of the sample and can be moved in and out of the neutron beam by a motor controlled drive similarly as the neutron guide elements. Furthermore, the lenses will be cooled to approx. 70 K in order to avoid thermal diffuse scattering. This cooling allows for a gain of intensity by a factor of approx. 3 for 7 Å neutrons and the maximum irradiated area. The whole construction allows for a lens operation with ease.

High resolution detector and chopper

A small high resolution detector will be installed in front of the conventional detector, and can be moved to any position covered by the large detector. When measuring at larger scattering angles the resolution is dominated by the wavelength distribution. Therefore, a chopper placed behind the selector in combination with a time-of-flight

analysis will select $\Delta\lambda$ channels of 1% and below. The small detector can also be placed to the beam centre, and then a USANS experiment is carried out with no need for a narrow wavelength distribution. In combination with the lenses a scattering vector of 10^{-4} \AA^{-1} will become available with a less stringent Q^{-2} restriction compared to the Q^{-4} law of conventional SANS [3].

GISANS

For the investigation of magnetic nanoparticles on surfaces or heterogeneous polymer films classical SANS in transmission geometry suffers mainly from the low scattering volume. If alternatively the beam impinges under a glancing angle (typically 1° or lower) the large footprint of the beam increases the scattering volume as well as the projection of the coherence volume onto the sample surface. In this way information about lateral as well as vertical correlations on length scales between 10 and 2000 Å can be obtained simultaneously at KWS-1. Due to the very small incident angle this technique has been established as grazing incidence small angle neutron scattering (GISANS). Additionally, as for many materials below a certain incident angle total external reflection occurs, GISANS can also be used for the investigation of surfaces or interfaces.

The positioning of the sample will be realized by a hexapod system, allowing a high accuracy of the incident angle as well as the rotation around the surface normal for anisotropic films. The polarization analysis described above

will allow for probing also the magnetic properties of magnetic nanoparticles or layered magnetic materials. To resolve also structures in the small angle regime, where the in-beam component of the scattering vector contributes significantly, the small detector will be used.

Present status

The KWS-1 and KWS-2 instruments currently under reconstruction at the FRM II reactor are positioned at the end of the NL3a-o (KWS-2) and NL3b (KWS-1) neutron guides. Both instruments are identical from the concept and consist of a 20 m collimator and a 20 m detector tube. Due to the foreseen upgrades, which are described in the previous section, the positioning of instruments within the FRM II neutron guide hall and the particular beam characteristics at FRM II (beam height, beam size, etc.) the constituent parts of the instruments were subject of major changes. The first change relates to the increase of the beam size from 30x45 mm² (in Jülich) to 50x50 mm² (at FRM II). Therefore, both instruments will be equipped with a new system of neutron guides (for each instrument 18 pieces x 1m length, with an $m = 1.4$ NiMo-Ti coating) inside the collimation case and new collimation apertures. The use of the old collimation housing required a modification of the working principle of the guide segments and apertures.



Figure 2.1: View along the KWS-2 collimation housing and mechanical components of the collimation system; to the left the collimation housing of the KWS-1 instrument can be seen.

Thus, the old system of one carriage supporting a neutron guide and a collimation aperture alternatively moved in or out of beam was replaced to that of distinct carriers for the neutron guide and aperture allowing them to move independently of each other (Fig.2.1). Currently, the collimation housing and the mechanical parts of the collimation system are installed and adjusted for both instruments.

Due to implementation of the optical focusing elements (parabolic lenses) the end segment of the collimation system towards the sample position was modified both technically and functionally. Thus, the old variable aperture defining the 1 m collimation length was cancelled and the first 1 m segment of the collimation housing was transformed into a separate chamber designated to host the carrying and the cooling system of lenses. In this way, the smaller collimation distance available will be of 2 m and defined by an adjustable aperture fixed on the separation window between the collimation and the housings of the lenses. Concerning the detection system, it is planned that, due to the limited space available for KWS-1 and KWS-2 instruments, the 20 m long detector tubes will be pushed out of the present neutron guide hall and located partially into the ring laboratory surrounding the old FRM-I reactor. Thus, the installation of

the complete detector housing will be possible only after joining the FRM II guide hall with the FRM-I ring laboratory (estimation: summer of 2007). For the currently available space into the FRM II guide hall a 14 m long detector tube was installed for the KWS-2 instrument.

The mechanical elements for guiding and transporting the detector (Fig.2.2) and cables inside the housing have been installed and adjusted. The vacuum system (pumps and controllers) was also installed and the tightness of the detector tube was successfully tested. The work of refurbishing the KWS-1 and KWS-2 instruments at FRM II reactor is currently in progress.

- [1] Choi, S.-M., Barker, J. G., Glinka, C. J., Cheng, Y. T., Gamme, P. L. *Journal of Applied Crystallography*, 33, (2000), 793–796.
- [2] Alefeld, B., Schwahn, D., Springer, T. *Nucl. Inst. a. Meth. in Physical Research A*, 274, (1989), 210–216.
- [3] Lengeler, B., Schroer, C. G., Richwin, M., Tümmler, J., Drakopoulos, M., Snigirev, A., Snigireva, I. *Appl. Phys. Lett.*, 74, (1999), 3924–3926.



Figure 2.2: Inside view of the KWS-2 detector housing.

2.2 MIRA – The beam line for very cold neutrons at the FRM II

R. Georgii¹, N. Arend¹, P. Böni², H. Fußstetter¹, M. Janoschek³, T. Hils², A. Mantwill¹, S. Mühlbauer², C. Pfeleiderer², R. Schwikowski¹, Shah Valloppilly²

¹ZWE FRM II, TU München

²Physics Department E21, TU München

³Laboratory for Neutron Scattering ETHZ& PSI, CH-5232 Villigen

MIRA is a versatile instrument for very cold neutrons (VCN) using neutrons with a wavelength $\lambda > 8 \text{ \AA}$ (see Fig. 2.3). The flux at the sample position is $5 \cdot 10^5$ neutrons/(cm² s) unpolarised. It is situated at the cold neutron guide NL6b in the neutron guide hall of the FRM II. As the instrument set-up can be changed quickly, MIRA is ideally suited as a testing platform for realizing new instrumental set-ups and ideas. In particular, MIRA is unique in its possibilities of combining different neutron scattering methods as:

- Polarized or non-polarized reflectometry.
- Spherical Polarimetry
- Polarized or non-polarized small angle scattering (SANS).
- Classical NRSE (Neutron Resonance Spin Echo) setup as well as using the MIEZE principle.

This year MIRA was successfully operated for 5 reactor cycles, **it means for 260 days (!)**. In total, 28 external and 33 internal proposals, several test and service measurements were performed. One example is shown in section 9.1. One Ph.D. thesis (Multi-Mieze measurements by Nikolas Arend (FRM II)) and several measurements for Diploma theses were finished using mainly data from MIRA.



Figure 2.3: MIRA equipped with the MIEZE option, a closed cycle cryostat and a magnet.

A new polarising multilayer monochromator was taken into operation. This allows now full polarisation analysis, 3D-polarimetry and MIEZE measurements. The MSANS principle was tested for later operation on MIRA. The existing magnet was upgraded for automatic adjustment of the field perpendicular to the neutron beam and independent from the sample movement.

Polarised reflectometry

Fe/Cr thin films and multilayers remain one of the most extensively investigated systems in thin film magnetism. Some pioneering discoveries in thin film magnetism like interlayer exchange coupling, giant magneto-resistance (GMR) etc. have been made on this system. Complex magnetic structure in Cr render intriguing magnetic properties in bulk as well as in thin films especially when Cr is used as a sandwich layer between two ferromagnetic layers. Earlier models of interlayer exchange in Fe/Cr multilayers were based on an oscillatory RKKY-type exchange coupling and quantum-well behaviour of the electrons in the Cr spacer layer. Later, calculations based on the commensurate and incommensurate spin density waves (SDW) in Cr, and direct observation of SDW by neutron scattering suggested that Fe/Cr multilayers display more rich variety of magnetic phenomena.

A variety of experimental techniques have been employed for the investigations that extend from bulk to layer resolved magnetometry like in Polarized Neutron Reflectometry (PNR). PNR reveals the vectorial layer magnetization and is very sensitive to the parallel and perpendicular components of magnetization with respect to the neutron polarization. Thus, bilinear and bi-quadratic types of layer configurations

can be easily resolved with depth sensitivity. The origin of bi-quadratic exchange has been attributed to intrinsic properties of the spacer layer, dipolar fields resulting from rough surfaces, super-paramagnetic impurities within the spacer, spacer thickness fluctuations etc. It has also been pointed out that the bi-quadratic exchange coupling has a dependence on the SDW.

The objective of the present work is to examine the magnetic configurations of the layers as a function of magnetic field and temperature of epitaxially grown [Fe(4 nm)/Cr(1.5 nm)]₁₀ on MgO single crystal by PNR, to corroborate with bulk magnetization results and to find a model to explain the temperature dependence of hysteresis behaviour. Epitaxial, Fe (4 nm)/Cr (1.5 nm)]₁₀ multilayers were grown by magnetron sputtering on a MgO(100) single crystal wafer of 1 x 1 cm. Polarized neutron reflectometry with full polarization analysis was implemented at the MIRA reflectometer by using flipper coils in conjunction with polarizing benders. Due to small size of the sample, a clear total reflection region was not obtainable marred by the large footprint of the beam. Nevertheless, clear effects of PNR are immediately visible in the corrected data as illustrated for a typical case, T=10K and H=500 Oe in Fig. 2.4(top). The splitting of non spin-flip (NSF) channels ++ and --, and the presence of half order Bragg peak in the spin-flip (SF) channel +- and -+ arising from the double periodicity of the magnetic lattice are indicative of the PNR with polarization analysis at MIRA. The experiments were performed around the magnetic (half-order) peak and its intensity as a function of applied magnetic field and temperature was measured. Fig. 2.4(bottom) summarizes the SF scattering intensity (integrated intensity of the half order peak) at selected fields and tem-

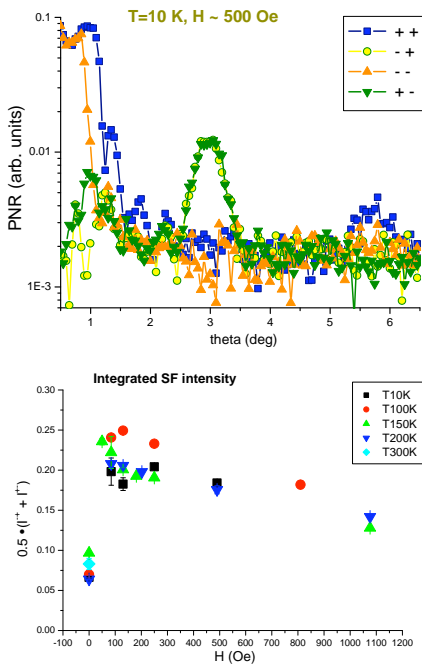


Figure 2.4: (top) PNR of Fe/Cr multilayers at 10K and $H \approx 500$ Oe. (bottom) Dependence of SF intensity as a function of field and temperature.

peratures.

In general, at remanence after exposing the sample to a high negative field, the Fe layers are found to order in an antiferromagnetic configuration as indicated by a high NSF intensity and a low SF intensity. By the application of a small magnetic field of 50 Oe, the NSF intensity drops to low values and the SF intensity increases. With further high magnetic fields, the SF intensity reaches a maximum at a certain field and thereafter decreases gradually. The highest SF scattering indicates the highest deviation of magnetization from the collinear configuration and its field dependence indicates the evolution of magnetization in an exchange coupled magnetization reversal process. Clearly, the magnitude and behaviour of the field dependence of SF intensity at various temperatures, suggest the role of Cr on inter-layer exchange and its temperature dependence.

3D-Polarimetry

MnSi crystallises in the cubic space group $P2_13$ with the lattice parameter $a = 4.558$ Å. MnSi is an itinerant-electron ferromagnet with a Curie temperature T_C of about 29 K and an ordered magnetic moment of $0.4 \mu_B$ on each Mn site. Its magnetic structure in zero field is a long-period ferromagnetic spiral with the propagation vector $(2\pi/a)(\zeta, \zeta, \zeta)$ with $\zeta = 0.017$ resulting in a period of approximately 180 Å [1, 2] along the [111] direction.

MnSi attracts presently high interest due to the speculation about an intermediate phase between the helical and the paramagnetic phase which may be triggered by the soft longitudinal fluctuations in MnSi. Roessler *et al.* [3] calculated that the magnetic state may form skyrmion patterns in this phase, e.g. the pinning of the spiral is cancelled by the fluctuations. This skyrmion condensate may only be stable when a variation of amplitude of the magnetisation is allowed. This intermediate magnetic ground state should in principle be observable by means of *Spherical Neutron Polarimetry* (SNP) as this technique is very sensitive to changes in the magnetic structure [4, 5, 6].

For the experiment the MuPAD option [5, 6] was installed on the very cold neutron instrument MIRA. In this SNP setup we used MIRA in small angle diffraction mode with a wavelength of 9.7 Å. The sample was adjusted on the instrument to fulfil the Bragg-condition on the magnetic satellite reflection (0.017, 0.017, 0.017). In order to have enough intensity to perform full polarisation analysis in the vicinity of T_c we adjusted MIRA to use the full beam divergence and thus, sacrificed Q-resolution (Slit after monochromator

15mmx50mm, circular slit in front of sample $\phi = 13$ mm).

When the optimum crystal position was adjusted we started to measure the temperature dependence on all matrix elements of the polarisation matrix (s. Fig 2.5). A polarisation value of about 92 % (s. e.g. Table 2.1) was observed on the xx, yx and zx terms of the matrix in the helical magnetic phase. This is due to the chiral term $i(\mathbf{M} \times \mathbf{M})$ which is generated by the anisotropic Dzyaloshinski-Moriya (DM) interaction [7, 8] that arises because of the non-central arrangement of the Mn moments in the unit cell. The chiral term additionally polarizes the neutron beam. All other terms are small and interpreted as zero. This is the polarization signature of a helical spin arrangement if the scattering vector \mathbf{Q} is parallel to the propagation vector of the helix. However, when the temperature is increased over the transition temperature T_{c1} the three terms xx, yx and zx slowly start to decrease until they go to zero at approximately $T_{c2} = 31.5$ K. This seems to indicate an intermediate magnetic phase between the helical and the paramagnetic phase as for a direct magnetic phase transition from a helical arrangement to an unordered state the helical signature is expected to be observed just until the transition temperature T_{c1} is reached, whereas a matrix with zero polarisation on all elements is expected just directly above T_{c1} . This is shown in the graphs in Fig 2.5 marked as 'Theory'.

Thus, the result supports the proposition of an intermediate phase in MnSi by Rößler *et al.* [3]. The experiment can be regarded as very successful even though special care has to be undertaken to analyse the data keeping in mind the effects of the coarse Q-resolution.

P_{out}		Measurement			Theory		
		x	y	z	x	y	z
P_{in}	x	0.836(7)	0.07(1)	0.09(1)	1	0	0
	y	0.880(1)	0.062(3)	0.091(3)	1	0	0
	z	0.880(1)	0.059(3)	0.083(3)	1	0	0

Table 2.1: Polarization matrix observed on the magnetic satellite reflection (0.017 0.017 0.017) at $T \approx 20$ K is shown together with the expected matrix for this magnetic structure. The elements where the x-component of the final polarization vector is measured are reduced from one due to the flipping efficiency of the polarisation analyser.

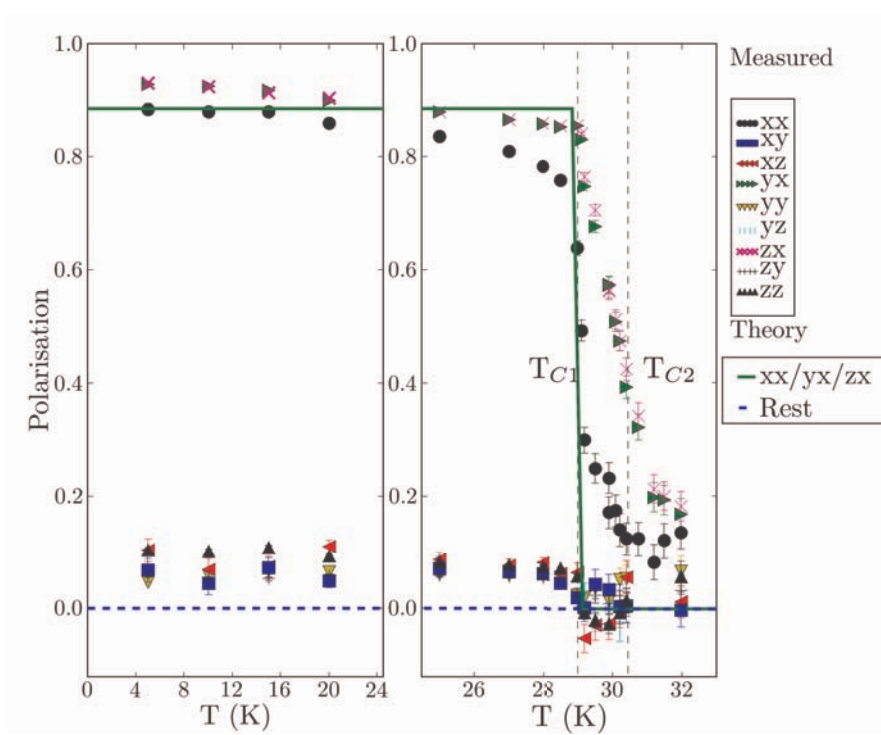


Figure 2.5: The temperature dependence of the matrix measured on the magnetic satellite reflection (0.017, 0.017, 0.017) is shown. Remarkable is the smooth transition from the helical below T_{c1} into the paramagnetic phase above T_{c2} . The lines show the expectation for the behaviour in the case that there would be no intermediate magnetic phase.

Spin echo option - MIEZE

In order to establish the MIEZE and NRSE techniques as standard measurement options at the instrument MIRA, new resonance spin echo hardware has been built and tested during the last few years. In 2006 several different measurements using MIEZE/NRSE have been performed, among those are

- Verification of the Multi-level MIEZE principle. The time-dependent, high-frequency sinusoidal signal of a MIEZE instrument can, just like the signal of an NSE/NRSE instrument, be used for quasi- and inelastic measurements with a wide range of applications. The MIEZE instrument, however, has a strong connection with a time-of-flight interferometer and is therefore potentially well-suited for fundamental physics experiments. One such application is the verification of

the longitudinal Stern-Gerlach effect, which manifests itself in the temporal splitting of the spin-up and spin-down states of a cold neutron beam when passing through resonantly tuned fields of an NRSE flipper coil. To actually see the splitting of a cold neutron pulse, such pulses must have a sharp width and a sufficient separation in time. These prerequisites are difficult to achieve by conventional beam chopping. A Multi-level MIEZE instrument, which could provide those kind of pulses, consists of several stacked single MIEZE parts, all tuned to have a common focusing point. This principle and the predicted pulse form and sharpening [9] was successfully verified at MIRA with a two-level setup. Fig. 2.6 shows the single and two-level signals and the respective non-linear fits.

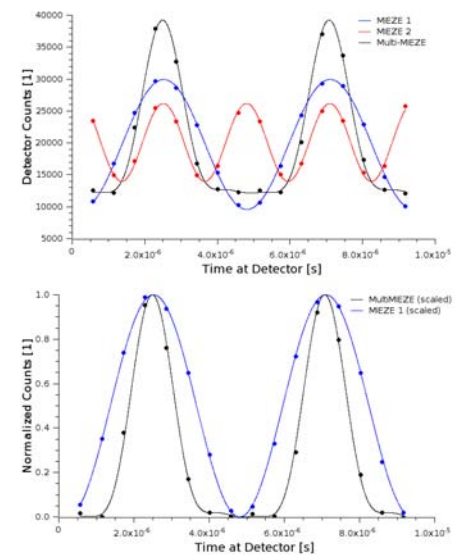


Figure 2.6: MIEZE and Multi-level MIEZE signal data with fits.

- MIEZE measurements with strong magnetic fields and a cryostat at the sample region. One of the strengths of MIEZE is the freedom the experimenter has in arranging the sample region compared to conventional NRSE. Since the MIEZE signal is already prepared after the second analyzer, it is easily possible to e.g. apply strong magnetic fields, do measurements on ferromagnetic samples, or realize long scattering geometries. Since these advantages do not seem to have been fully recognized in the past, we performed a showcase measurement: A MIEZE setup at MIRA was equipped with a 2 kG solenoid and a cryostat (see Fig. 2.3). The magnetic field at the sample region was gradually increased while monitoring the contrast of the MIEZE signal. If the strong magnetic field (i.e. its stray fields) would have destroyed the beam polarization, the initial contrast of $\approx 80\%$ would have decreased significantly. The 2D scan in Fig. 2.7 shows that this was not the case, proving the suitability of MIEZE for such measurement environments. An interesting sample to investigate with MIEZE is e.g. MnSi with its chiral magnetic

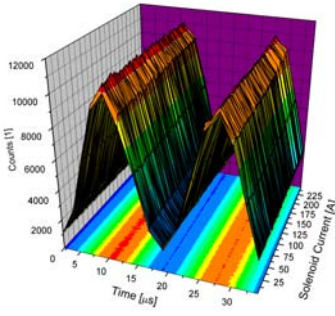


Figure 2.7: 2D scan of MIEZE signal vs. solenoid current. The signal contrast of approx. 80% is more or less unaffected.

structure that is revealed at low temperatures and high magnetic fields.

Multiple Small Angle Neutron Scattering (MSANS)

Research on polymers, colloid systems, cements, microporous media, are examples of a rising field, where μm -correlations play a crucial role. Small angle X-ray and neutron scattering (SAXS and SANS) typically measure lateral correlation lengths in the 0.01 to 1 μm range, the q -resolution ranging up to 10^{-3}\AA^{-1} . To measure larger μm correlations with neutrons, the q -resolution has to be improved and various specific instruments have been designed. The technique is commonly known as USANS (ultra small angle neutron scattering). However these methods are sensitive to scattering only in one dimension and often suffer from intrinsic small angle scattering due to structure material in the beam.

Here we propose MSANS (Multi hole SANS), a new USANS option for a standard long baseline SANS instrument. It uses the common SANS infrastructure except for the detector, which requires enhanced spatial resolution. We aim at improving the q -resolution to about 10^{-5}\AA^{-1} at 10 \AA , so correlations up to 60 μm should be possible.

Using multi-hole apertures at the entrance (M_e) of the collimator and near the sample (M_s) with lattice constants a_e , a_s and hole diameters d_e , d_s

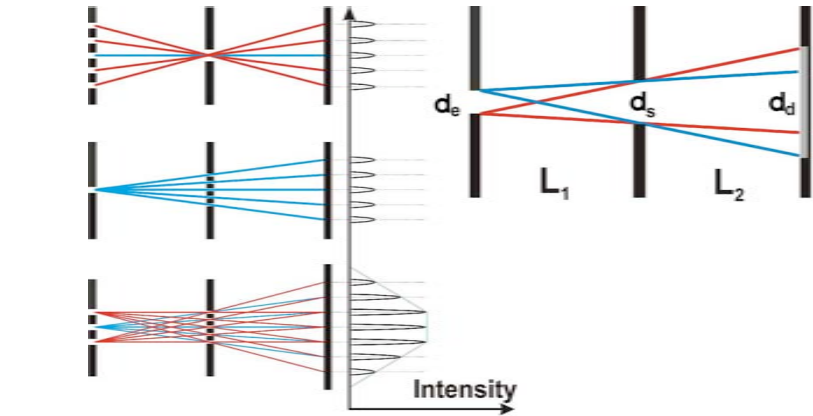


Figure 2.8: (Top) Number and Intensity of spots depends on number of holes of sample and entrance mask (see Fig. 2.9). (Bottom) Width of spots at detector depends on width of entrance and sample aperture.

respectively and with the choice

$$G_{e,s} = \frac{2\pi}{a_{e,s}}$$

$$G_e \cdot L_1 = (G_s - G_e) \cdot L_2$$

$$G_d = G_s - G_e$$

an intensity pattern of well separated peaks with lattice constant a_d in the detector plane is observed ($a_d = 2\pi/G_d$) (see Fig. 2.8).

Short range correlations in the sample may lead to significant overlap, however typical SANS intensities drop very rapidly with increasing q , and overlap will not be fatal in many cases. Sets of apertures with different relations $a_{e,s} / d_{e,s}$ (d diameter of hole apertures) can be used to adapt the pattern to the demand. In MSANS, resolution is decoupled from intensity, as long as the transmission of apertures is kept constant. The increase in q -resolution in MSANS is typically one order of magnitude, compared to SANS at equal intensity. The gain originates from the reduction in q -range in MSANS and the increase of the input guide cross section and its divergence. Diffraction from the aperture holes of typically 1mm are

not yet crucial, as the beam correlation length is only in the μm range.

Prototypes of a set of multihole-apertures based on cadmium and coated with typ. 13 μm ^{10}B were produced with the following properties: hole diameter $d_{e,s} = 0.5/1\text{mm}$; lattice constant $a_{e,s} = 2.5/5\text{mm}$. The proposed configuration leads to $\text{FWHM} \approx 1\text{mm}$.

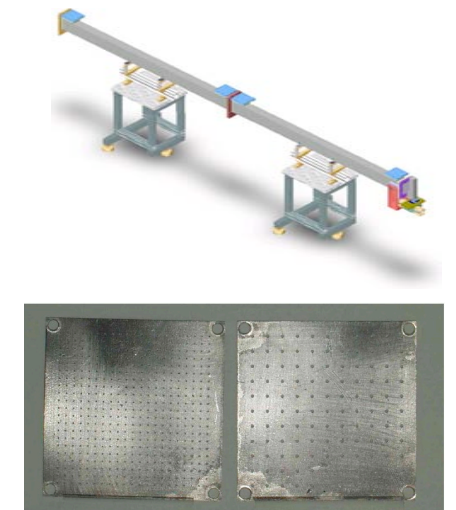
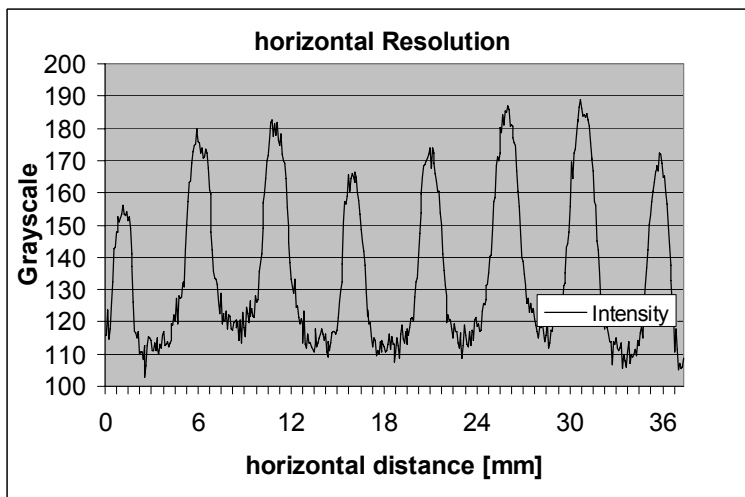
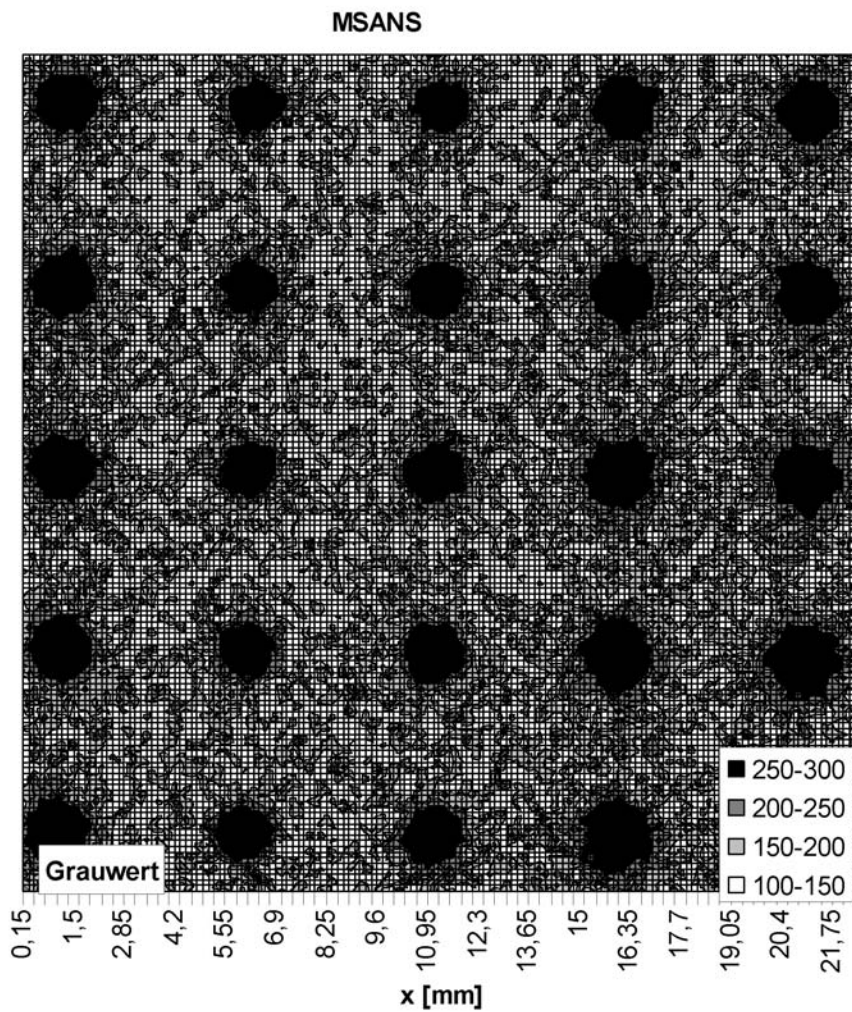


Figure 2.9: (top) MSANS setup, (bottom) Multihole apertures



In 2006 a first setup on the MIRA beam-line at FRM II was accomplished and preliminary measurements (Fig. 2.10) mainly concerning the basic principle were made.

- [1] Shirane, G., Cowley, R., Majkrzak, C., Sokoloff, J., Pagonis, B., Perry, C. H., Ishikawa, Y. *Physical Review B*, (1983).
- [2] Roessli, B., Böni, P., Fischer, W., Endoh, Y. *Phys. Rev. Lett.*, (2002).
- [3] Rößler, U. K., Bogdanov, A. N., Pfeleiderer, C. *Nature*, 442, (2006), 797–801.
- [4] Tasset, F. *Physica B*, 156-157, (1989), 627.
- [5] Janoschek, M. " ". Master's thesis, Technical University Munich, <http://mupad.wired-things.de> (2004).
- [6] Janoschek, M., Klimko, S., Roessli, B., Medarde, M., Böni, P. *Annual Report E21*, 21.
- [7] Dzyaloshinskii, L. *J. Phys. Chem Solids*, 4, (1958), 241.
- [8] Moriya, T. *Phys. Rev.*, 120, (1960), 91.
- [9] Arend, N., Gähler, R., Keller, T., Georgii, R., Hils, T., Böni, P. *Physics Letters A*, 327/1, (2004), 21–27.

Figure 2.10: (top) 2d-Intensity map (arbitrary units) showing resolution in real-space, (bottom) Approximation of horizontal resolution due to direct superposition of intensity in y-dir.

2.3 N-REX⁺ – The Neutron/X-ray contrast reflectometer for materials science

A. Rühm^{1,2}, M. Nülle¹, F. Maye¹, J. Franke^{1,2}, U. Wildgruber^{1,2}, J. Major^{1,2}, H. Dosch¹

¹Max-Planck-Institut für Metallforschung, Stuttgart

²Max-Planck-Institut für Metallforschung, Stuttgart, outstation at FRM II

During the year 2006 the basic commissioning of the neutron reflectometer with add-on X-ray option, N-REX⁺ [1], has been completed. The majority of instrument operation modes have been implemented and undergone first experimental tests on real samples. This includes conventional neutron reflectometry, X-ray reflectometry, and spin-echo resolved grazing incidence scattering (SERGIS) on solid samples. The implementation of SERGIS includes polarization control as it is also required for polarized neutron reflectometry. A tilt of the neutron beam, as required for the study of free liquid surfaces, has been realized, but is not yet automated.

Results

In 2006 we have focussed on the main novelties provided by N-REX⁺, i.e. in-situ neutron/X-ray contrast variation and the novel SERGIS technique [2].

The results of a combined neutron and X-ray reflectivity measurement on a nickel/titanium multilayer on silicon

substrate are shown in Fig. 2.11. The corresponding experimental setup is shown in 2.12. The multilayer was measured i) after sputtering at room temperature and ii) after subsequent annealing in vacuum for 5 hours at 300 °C. From the electron and neutron scattering length density profiles derived from the reflectivity curves we conclude, that after annealing the nickel layers have completely disappeared and Ni₄Ti₃ layers have formed instead due to interdiffusion. Only 1.4 nm thick titanium layers remain, interlaced between the Ni₄Ti₃ layers. Interestingly, this alloy phase is instable in the bulk, but it can be stabilized in the reduced dimension of a thin-film geometry. We are planning a more detailed investigation of the stability of these alloy layers, as well as an extension of the combined neutron/X-ray reflectometry technique to magnetic systems and to in-situ studies.

Regarding the second focus area of N-REX⁺, we have installed and tested the spin-echo setup and conducted first SERGIS experiments on reference sam-

ples. First scientific studies on real samples have also been started recently. Fig. 2.13 shows N-REX⁺ in spin-echo operation mode. Visible is the mumetal housing extending over the sample region and two neutron resonance spin-echo coil assemblies, upstream and downstream of the sample. A first SERGIS data set obtained on an optical grating with 3600 lines per mm is shown in Fig. 2.14. The polarization P of the in-plane integrated diffuse scattering signal from this sample at fixed incidence and exit angle is plotted (after correction for instrumental imperfections) as a function of the spin-echo length l_{SE} . $P(l_{SE})$ is proportional to the in-plane pair-correlation function $g(r = l_{SE})$ of the sample in real space [2]. The position of the first peak in the SERGIS data corresponds well with the known groove period of 280 nm of the grating. This experiment demonstrates the suitability of SERGIS for the characterization of mesoscopic in-plane structures in the 100 nm to 1000 nm range, which are for intensity reasons unresolvable by conventional neutron reflectometers

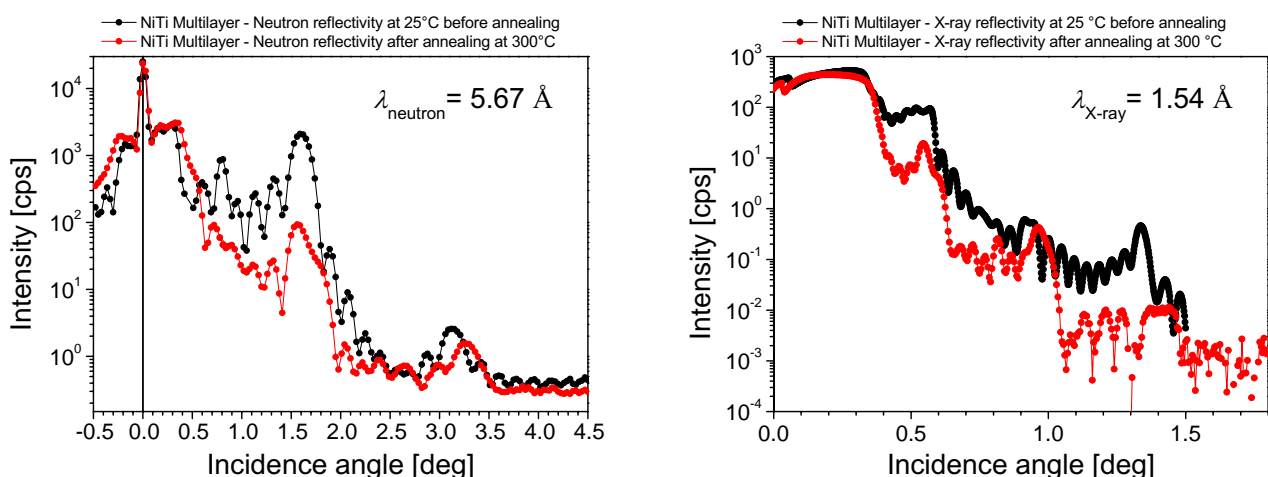


Figure 2.11: Neutron and X-ray reflectivity curves measured on a [Ni(5 nm)/Ti(5 nm)]₈/Si multilayer before and after annealing and interdiffusion at 300 °C.

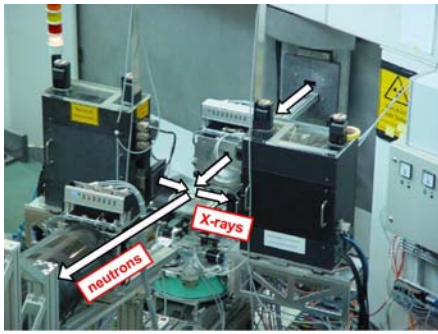


Figure 2.12: The N-REX⁺ sample table with compact X-ray source and detector units mounted for simultaneous neutron/X-ray reflectivity experiments. The neutrons are impinging from the monochromator hutch on the right, the neutron area detector (not shown) is located on the left.



Figure 2.13: N-REX⁺ in neutron resonance spin-echo operation mode, with the neutron monochromator hutch on the right and the detector tower on the left.

with the GISANS technique.

2.4 SANS-1, the Small-Angle Scattering instrument

R. Gilles¹, B. Krimmer¹, A. Ostermann¹, O. Nette², A. Vogel², R. Kampmann^{1,2}, H. Türck¹, P. Jüttner¹, J. Krüger¹, K. Zeitelhack¹, A. Schreyer², W. Petry¹

¹ZWE FRM II, TU München

²GKSS Forschungszentrum Geesthacht

Major tasks in 2006 were test and installation of the Z-translation and omega tilt (Z/tilt) stage for the selector, the first start of the medium resolution velocity selector delivered by EADS/Astrium and the test and installation of the instrument shutter together with a monitor at the end of the S-shaped neutron guide (see Fig. 2.15). A small z-translation moves this moni-

Outlook

In the next months, the various operation modes of the instrument N-REX⁺ will be further optimized and automated for routine application. Figures to be optimized are the background level, the neutron flux, the required measurement times, and the measurement speed.

[1] Rühm, A., Wildgruber, U., Franke, J., Major, J., Dosch, H. In *Neutron Reflectometry, A Probe for Materials Surfaces, Proceedings of a Technical Meeting organized by the International Atomic Energy Agency and held in Vienna, 16-20 August 2004, Vienna, Austria*, 161–175 (2006).

[2] Major, J., Dosch, H., Felcher, G. P., Habicht, K., Keller, T., te Velthuis, S. G. E., Vorobiev, A., Wahl, M. *Physica B*, 336, (2003), 8–15.

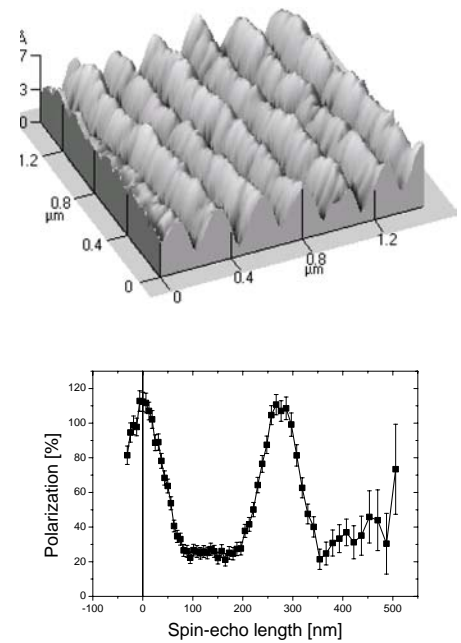


Figure 2.14: First successful SERGIS measurement at N-REX⁺ on an optical grating. An AFM image of the grating is shown on top. In the SERGIS experiment, the grooves were aligned parallel to the incident beam direction. The SERGIS data curve is explained in the text.

tor into and out for measuring the white beam. The Z/tilt stage enables the user to choose between a high intensity velocity selector with medium resolution of $\Delta\lambda/\lambda = 10\%$, a neutron guide for white beam experiments or a high resolution velocity selector (optional). Tilting of the complete stage allows an additional adjustment of the selector resolution in combination with one of the

velocity selectors [1]. Monitor 2 is foreseen as one of the instrument monitors which gives a value for the neutrons entering the polarizer and collimation section (Fig. 2.16).

Another significant step has been the construction and set-up of the velocity selector shielding cube. Fig. 2.17 shows the Z/tilt stage mounted and an aluminum cage around it. This cage

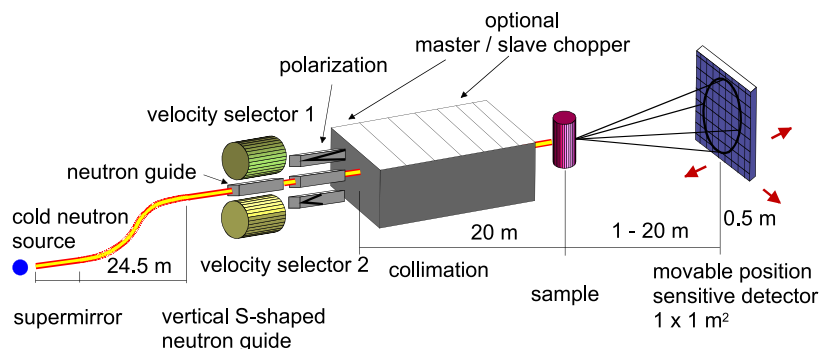


Figure 2.15: Schematic drawing of the new SANS-1 instrument.

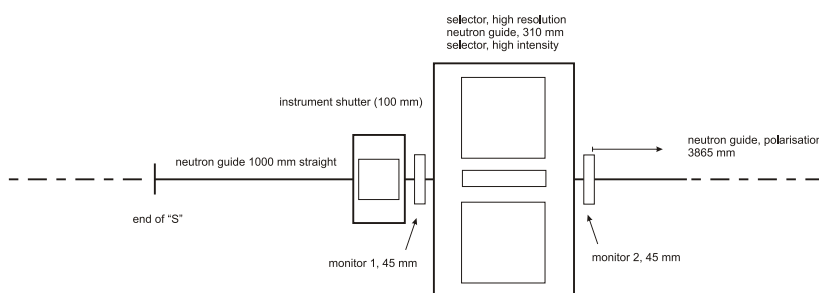


Figure 2.16: Schematic set-up of the velocity selector area.

works as a carrier for the lead shielding (thickness 100 mm). B_4C mats are covering the inner lead surface.

A first neutron distribution measurement at the end of the S-shaped neutron guide was performed [2]. In Fig. 2.18 is a comparison of the simulated neutron distribution and a measurement of the white beam just before the selector position. Fig. 2.18a shows the first measurement of the beam profile (line of sight against the beam) directly after the S-shaped neutron guide. Both, the simulation and the measurement show in the upper half of the two-dimensional pattern higher intensity than in the lower half (see Fig. 2.18b) which is caused to the S-shaped neutron guide positioned in vertical.

The result of a Monte Carlo simulation for this position is given in Fig. 2.18b. The averaged beam profile in horizontal and vertical direction is shown in Fig. 2.18c and Fig. 2.18d respectively. As expected there is slight decrease from the right to the left side (compare Fig. 2.18c). This is due to the horizontal curvature ($R=2100$ m) of the last 12.2 m section of the S-shaped neutron guide. The vertical intensity distribution (see Fig. 2.18d) is not reproduced by the simulation. Further Monte Carlo simulations have shown that the position of the intensity maxima are strongly correlated with the illumination of the beam tube nose and therefore with the filling state of the cold source. The filling state of the cold source slightly differs from

one reactor cycle to another. For the shown simulation results a completely filled cold source with a nearly empty displacement body was assumed.

The next component which will be installed is the collimation set-up. The vacuum chambers are currently built and most of the internals (optics, translation systems etc.) are under construction. At the moment the containers of the vacuum chamber will be prepared for vacuum tests. One of the seven containers is shown in Fig. 2.19.

[1] Gilles, R., Ostermann, A., Schanzer, C., Krimmer, B., Petry, W. *Physica B*, 385-386, (2006), 1174–1176.

[2] Gilles, R., Ostermann, A., Petry, W. *J. Appl. Cryst.*, (2006). Submitted.



Figure 2.17: First selector installed on site in a Z/tilt stage. (Shielding not shown in this picture).

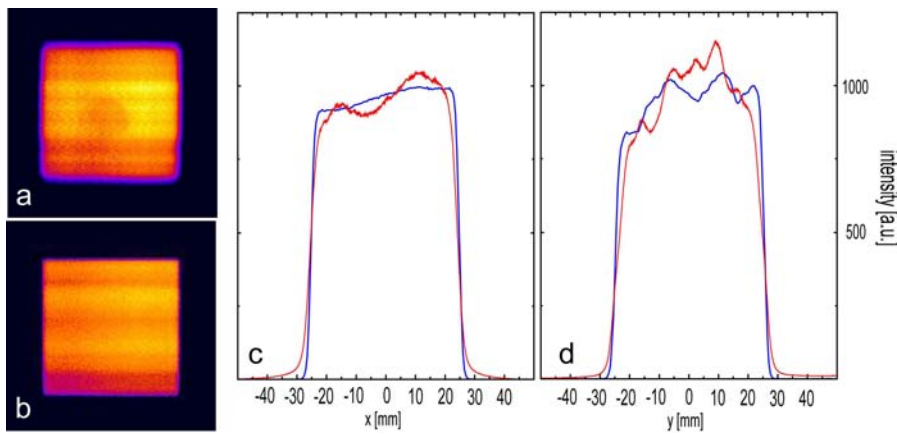


Figure 2.18: Beam profile at the end of the S-shaped neutron guide: (a) Profile measured with neutron imaging plate, (b) Monte Carlo simulation, (c) Averaged horizontal beam profile of the measured data (red) and the Monte Carlo simulation (blue) and (d) Averaged vertical beam profile.



Figure 2.19: Vacuum chamber.

2.5 TREFF@NOSPEC : A facility dedicated to test neutron optical devices

U. Rucker¹, A. Ofner², S. Mattauch³, A. Ioffe³, T. Brückel¹, G. Borchert²

¹IFF-Streumethoden, Forschungszentrum Jülich

²ZWE FRM II, TU München

³JCNS, Forschungszentrum Jülich, outstation at FRM II

The Temporary REflectometer Facility (TREFF) (Fig.2.20) is a dedicated reflectometer and diffractometer for the test of neutron optical devices. It is a joint project of the Jülich Center for Neutron Science (JCNS) and the Neutron Optics Group of FRM II. The instrument is equipped with polarized neutrons, polarization analysis and a 2D position sensitive detector, which is completely covered by the polarization analyzer (see Fig. 2.21). A zero-field chamber with 3D vector polarization analysis of the transmitted beam will be added soon. TREFF will serve as a flexible and high-intensity instrument for investigation of neutron optical devices as supermirrors (polarizing and non-polarizing), monochromator crystals, spin turners etc. Furthermore, it will host the research activities of FZ Jülich on magnetic thin films until the startup of MARIA (Magnetism re-



Figure 2.20: TREFF@NOSPEC: From the cylindrical shielding of the first monochromator (right) the neutrons are brought to the shielding box of the second monochromator. Then follows the collimation (with the resonance spin flipper coil around the vacuum tube), the sample table and the detector arm (middle left).

flectometer with variable Incident Angle), which is currently being designed. TREFF is not a regular scheduled user instrument of FRM II.

TREFF is located at the beamport NOSPEC (Neutron Optics' SPECTrometer) of the Neutron Optics Group using the lower part of the neutron guide NL5-S, which it shares with RESEDA (REsonance Spin Echo for Diverse Application). TREFF uses main components of the former HADAS reflectometer [http://www.fz-juelich.de/iff/wns_hadas] that used to be installed at the reactor FRJ-2 in Jülich. The neutrons are extracted from NL5-S with a double monochromator at a Bragg angle of $2\theta=90^\circ$.

In a first step, TREFF will operate at $\lambda=4.75\text{\AA}$, delivered by PG (002) monochromator crystals. A vertically focussing monochromator and a collimation with two pairs of slits in a distance of 170 cm deliver a beam to the sample position, which is 4 cm high, has a vertical divergence of 1.9° and can be collimated horizontally between 0.1 and 16 mrad. To reduce the background, a vacuum tube is inserted between the collimation slits. A transmission polarizer can be placed automatically between the second monochromator and the first slit and offers polarized neutrons with a

maximum divergence of 4 mrad. A resonance spin flipper is used to control the direction of the incident neutrons' spins. In a second step, we will install Nb(002) monochromator crystals to be used alternatively to P.G.(002) (Pyrolytic Graphite). This will allow to use $\lambda=2.5\text{\AA}$ for the investigation of single crystal quality, mosaic spread and orientation.

The sample table can take and adjust heavy loads of up to 300 kg in all 6 dimensions (3 translation and 3 rotation degrees of freedom). An electromagnet with $\mu_0H=450\text{ mT}$ over 10 cm gap between the poles or 1.9 T over 2 cm gap is available to expose the samples to a magnetic field.

The detector arm carries a lead and B_4C shielding tunnel to protect the detector from gamma and neutron background, that is not coming from the sample. It contains an evacuated beam tube with spin flipper, a beamstop for the part of the primary beam, which is not reflected by the sample, a polarization analyzer (see Fig. 2.21) and a 2D detector. The inclination of the polarization analyzer can be adjusted automatically either to be polarizing or transparent (for maximum transmission without polarization analysis). It is designed to offer good polarization efficiency without compromising angular resolution and sensitivity over the

whole range of scattering angles, which the detector covers. The detector has a circular sensitive area with 80 mm diameter and a spatial resolution of 1.5 mm. It is mounted at a distance of 1.6 m from the sample, so that it covers a range of scattering angles of 2.2° . Scattering angles of more than 60° can be reached by moving the whole arm on air cushions.

The first parts arrived in Garching in March 2006 after having been assembled and tested in Jülich. During the past months the instrument has been assembled in the Neutron Guide Hall of FRM II. Today, we are ready to start the commissioning of the instrument as soon as the modification of the neutron guide NL5-S is accomplished and neutrons are available.

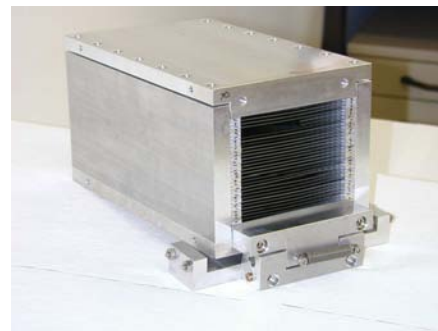


Figure 2.21: The polarisation analyzer of TREFF.

3 Structure research

3.1 HEiDi – Single crystal diffractometer with hot neutrons

M. Meven¹, V. Hutanu^{1,2}, G. Heger²

¹ZWE FRM II, TU München

²Institut für Kristallographie, RWTH Aachen

General

HEiDi is one of the two single crystal diffractometers at the neutron source Heinz Maier-Leibnitz (FRM II). It is placed at beam line SR9B in the experimental hall of the reactor building (fig. 3.1). It was developed in collaboration between the RWTH Aachen (Institut für Kristallographie) and the TU München (ZWE FRM II) to cover a broad range of scientific cases in the area of structural research on single crystals in the following fields of interest:

- Crystal structure analysis (harmonic and anharmonic mean square displacements, hydrogen bonds, molecular disorder).
- Investigation of magnetic ordering (magnetic structure, spin density).
- Structural and magnetic phase transitions.

Beam line SR9 uses the hot source of the neutron reactor. This leads to a remarkable increase of the neutron flux below 1 Å with a gain factor of 7.7 at 0.44 Å (fig. 3.2).

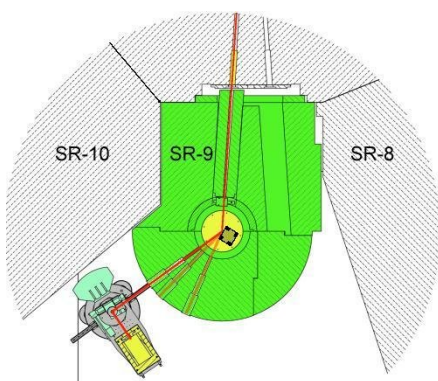


Figure 3.1: Overview of HEiDi

The hot source itself consists of a graphite cylinder with temperature around 2300 K at the maximum reactor power of 20 MW and shifts the thermal neutron spectrum to shorter wavelengths. Diffraction experiments with the focus on structural and magnetic details profit at HEiDi from the access to a very large reciprocal space ($Q = |\vec{Q}| = \sin\Theta_{max}/\lambda$) with $Q > 1.5$ at 0.55 Å. Other advantages are the

- reduction of extinction effects of large and very perfect single crystals and
- reduction of absorption effects in compounds with highly absorbing elements like samarium or gadolinium.

Although we had to focus our efforts on the development of the new BMBF supported polarized diffractometer at SR9 and in spite of the vacant position of the technician for HEiDi since August 2006, we managed to guarantee the high availability of our instrument for experiments of internal and international users through the whole year. Details of the instrument and its applications were presented on the DGK meeting in Freiburg and on the SNI 2006 in Hamburg.

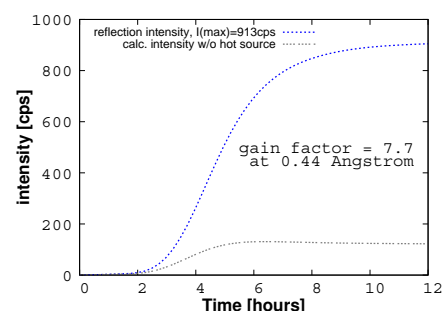


Figure 3.2: Gain factor of hot source at SR9

Sample environment

Since January 2006 a small closed cycle cryostat (Sumitomo SDK101) is available at HEiDi. The minimum temperature of 2.2 K makes the instrument very attractive for detailed investigations on magnetism at low temperatures.

In the last cycle of 2006 the cryostat was successfully tested with substantially more flexible connectors between the stiff He hoses and the rotating cryostat in the Eulerian cradle. This change reduces the angular limits of HEiDi at low temperatures. Therefore, the number of observable reflections could be increased significantly. In figure 3.3 the old and the new design of the cryostat is shown.

An air cooled furnace (developed at FZ Jülich) was successfully tested with a

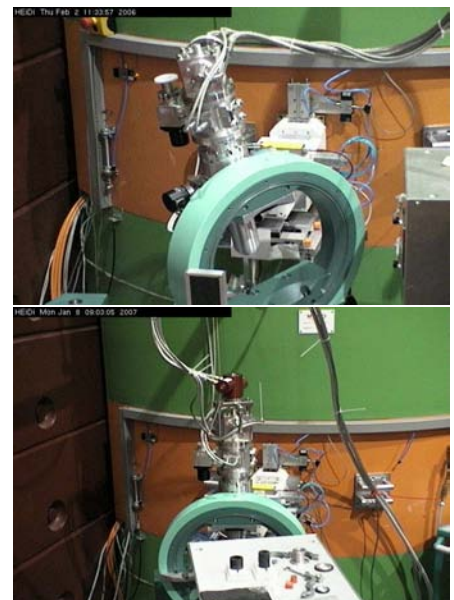


Figure 3.3: Cryostat in cradle: without (top) and with (bottom) rotating connectors

maximum temperature of about 1100 K (fig. 3.4). Currently optimizations of this furnace design as well as alternative techniques (mirror furnace for Eulerian cradles) are discussed to improve the maximum temperature significantly according to the users needs. Experiments with slightly increased temperatures up to about 420 K can be performed with a small furnace developed at the Institut für Kristallographie, RWTH Aachen (fig. 3.4).

Scientific output

In the last three proposal rounds HEiDi was always substantially overbooked. On average only less than half the time requested altogether in the proposals could be assigned. In 2006 15 proposals were accomplished at HEiDi with altogether 180 days. Additionally, some time was used to check crystal orientations and homogeneities of samples that were used for experiments on other instruments at FRM II, especially the triple axes spectrometers. Typical scientific cases of the proposals were

- magnetic superstructures at low temperatures,

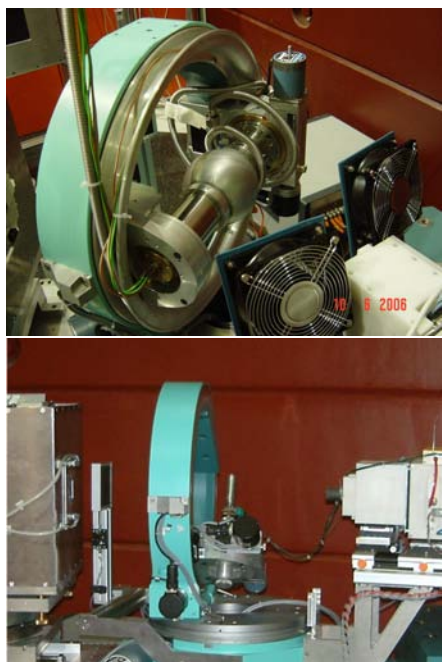


Figure 3.4: Large (top) and small (bottom) furnace in Eulerian cradle

- order/disorder phase transitions at low and high temperatures,
- ionic conductors and
- local disorder or vacancies, esp. of H bonds.

A typical result from a temperature dependent measurement of a magnetic superstructure is shown in figure 3.5, where the evolution of the magnetic (110) reflection in the antiferromagnetic state of the artificial olivine Co_2SiO_4 – starting at $T_c = 49.5$ K – can be seen down to 2.2 K.

This measurement is part of a Ph.D thesis (A. Sazonov from the Institut für Kristallographie, RWTH Aachen) where the influence of the symmetrically nonequivalent Co^{2+} sites on the magnetic superexchange cross sections is of large interest. In December 2006 a data set of this compound was measured at HEiDi at 2.2 K and up to $Q = \sin\Theta/\lambda = 1.1$ to determine precisely the nuclear structure separately from the magnetic contributions in the reflection intensities which vanish at $Q = 0.7$.

Polarized diffractometer at SR9

The development of the polarized diffractometer at SR9 is supposed to extend the capabilities of single crystal investigations with hot neutrons at FRM II to zero field 3d polarization analysis and to spin density analysis using the spin flip method. To polarize the hot neutrons ^3He spin filter cells are used which get their helium from the HELIOS facility at FRM II.

In 2006 we focused our efforts on the development and testing of components for polarization analysis, e.g. ^3He spin filter cells with large relaxation times, magnetic cavities for stabilising the cells and shielding them from external fields and zero field polarization analysis devices (PAD). One of the most important experiments in this framework was the test of the muPad, a device for zero field polarization analyses

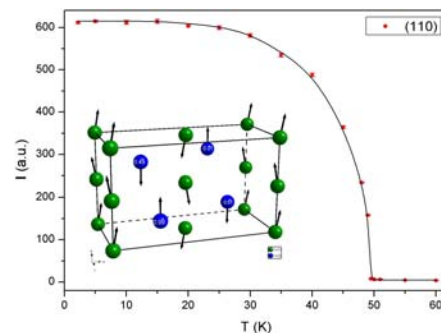


Figure 3.5: Temperature dependence of the magnetic (110) reflection of Co_2SiO_4

developed at PSI and E21/TUM using the complete HEiDi diffractometer unit as polarization analyser and detector (fig. 3.6). This was also the first time, ^3He spin filter cells were used as polarizers and analysers as well. More details about the polarized diffractometer at SR9 can be found in the section 3.2 in this annual report.

Outlook

The successful extension of HEiDi with sample environments like cryostat and furnaces was an important step forward to fulfil the needs of our scientific users. Developments to solve minor problems like the limited $T_{max} = 850$ °C of our large furnace are in progress and should be solved in 2007. Altogether, in 2006 HEiDi has proven to be an extremely efficient tool for multiple scientific cases in the area of detailed structural analysis.

The development of the new polarized neutron diffractometer took a big step forward in 2006. A large number of new components were successfully tested (^3He spin filter cells, magnetic cavities, etc.), others are currently under construction. For 2007 the assembly of all these components and the successful commissioning of this new device for zero field 3d polarization analysis is a major goal.



Figure 3.6: Test of components for polarization experiments

3.2 Progresses in the development of the polarized neutron diffractometer POLI-HEiDi

V. Hutanu^{1,2}, M. Meven², G. Heger¹

¹Institut für Kristallographie, RWTH Aachen

²ZWE FRM II, TU München

In fall 2004, the Institute of Crystallography at the RWTH Aachen started a BMBF supported project to extend the existing new single crystal diffractometer HEiDi at the new research neutron source Heinz Maier-Leibnitz (FRM II) with a polarized neutron option to allow detailed investigations on the magnetic order of single crystals. The evaluation of the problems connected to a direct implementation of the polarized neutron option on the existing instrument lead to the decision to build a new instrument especially designed for this purpose, called POLI-HEiDi (**P**olarisation Investigator – HEiDi). Both options, zero-field spherical polarization analysis in complex magnetic structures and spin density distribution analysis using a high magnetic field for flipping ratio measurements should be available at the new

instrument. Several components for this new polarized diffractometer were developed, produced and successfully tested in 2006.

³He spin filter cells

Taking into account the existing polarized ³He production facility “Helios” at FRM II and the advantages of ³He spin filters for hot neutrons [1, 2], it was planned to use NSF cells as polarizers and analyzers as well. Two spin filter cells specially optimised by maximising the quality factor for neutrons with wavelengths of 0.68 Å and 0.87 Å were realised. The dimensions of the cells are 60 mm in diameter and 130 mm inner length. The maximum thickness of the windows is 4 mm. The working pressure can be chosen up to 3 bar, while the

burst pressure is not less than 5 bar. In the Fig. 3.7 a picture of the cells *Heidi1* and *Heidi2* is shown. Both cells are made of HOQ 310 quartz glass and were coated inside with Cs.

The final preparation and Cs coating was done by S. Masalovich and O. Lykhvar from the neutron optics group at FRM II. After the preparation the relaxation time constants T_1 measured in the cells were 137(3) h for cell *Heidi2* and 114(3) h for cell *Heidi1*. Minor variations of T_1 in the cells are probably due to exposures to slightly different magnetic environments as observed during the tests in 2006. Nevertheless repeated degaussing of the cells and “refreshing” of the Cs coating inside the cells even improved the relaxation time constant of the cell *Heidi1*



Figure 3.7: a) Spin filter cell *Heidi2*: Small metallic Cs droplets in the lower part of the cell and in the appendix are visible; b) Cell *Heidi1*: The dark spots inside the cell are traces of Cs sub-oxide which is liquid at room temperature.

up to about 165 h. The transmission of our empty quartz glass cells at a neutron wavelength of 0.55 \AA was found to be between 0.85 and 0.88 depending on the window thicknesses.

Magnetostatic cavities

Two compact magnetic cavities based on permanent magnets and mu-metal sheets were constructed in 2006 and are dedicated for 130 mm cells use. The design of our cavities is similar to that of the “magic box” cavities recently developed at the ILL [3] but more compact. The outer dimensions are (L×B×H) $380 \times 250 \times 100 \text{ mm}$. Calculations by means of a finite element magnetic simulation software promised a field homogeneity of $(dB/dr)/B < 2 \times 10^{-5} \text{ cm}^{-1}$ in the central region. In spite of the smaller experimental value of about $2 \times 10^{-4} \text{ cm}^{-1}$ obtained from our ^3He relaxation measurements, this result guarantees a $T_{1\text{magn}}$ value of about 400 hours, representing the relaxation time constant due to magnetic field gradients in the cavity. The deviation between the simulation and the experimental result can be explained by imperfections of the mu-metal parts and by inhomogeneities of the used permanent magnets. In Fig. 3.8 “magic box” one *MB1* is presented.

To assure the parallelism between the polar pieces and to avoid deformations of the sensible mu-metal sheets the box

is fixed in an aluminium frame, which serves also for easy installing in the Euler cradles in the front of detector on the instrument HEiDi during our experiment. In Fig. 3.9 “magic box” two (*MB2*) is presented.

The frame is fixed on an aluminum front flange which can be rotated 180° by pneumatic drives and a tooth belt. The time for a 180° rotation (flip) is less than 0.5 seconds. Such a device with reliable fixed ^3He spin filter cell inside permits the transversal polarization of the transmitted neutron beam in any direction in the plane perpendicular to the propagation direction of the beam. We call it “HERO-Pol” [4] as abbreviation for (Helium Rotating Polarizer).

Non-magnetic support unit

The concept and design of the new non-magnetic diffractometer basic unit was completed. The support unit is con-

ceived as a single massive part for two reasons:

One is to reduce the total dimensions and to assure shortest drive-times for the detector, the other one is the capability to support bulky and heavy components like cryomagnet or MuPAD.

It consists of a massive Al-alloy made mounting plate with two concentrically fixed rotating tables, one for the analyzer/detector and one for the sample. The first one moves a detector plate which is designed to bear two exchangeable setups, one for an analyzer-detector unit for 3D polarimetry and one for a lifting-counter for flipping ratio measurements with a magnet. Between the two rotating tables a support plate for the sample environment devices as well as for the polarizer unit is foreseen. A 2D tilting table is positioned on top of the sample rotation table. In Fig. 3.10 a draft of the support unit with lifting counter is presented.

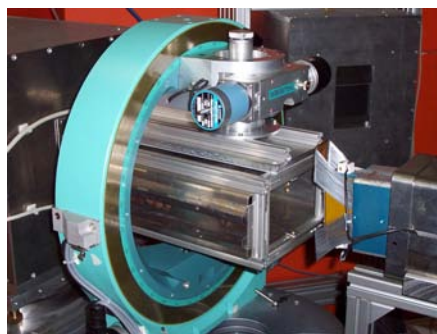


Figure 3.8: Compact magnetostatic cavity *MB1* during the test measurements fixed in the Euler cradles of instrument HEiDi



Figure 3.9: Magnetostatic cavity *MB2* fixed on the rotating flange permitting 180° “flipping”

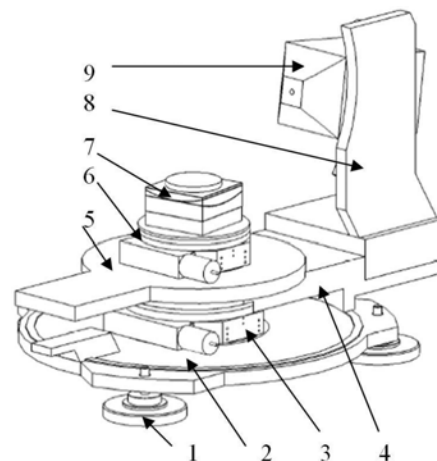


Figure 3.10: Non magnetic support unit and its parts: 1 – Air cushions (load capacity $\geq 1.5 \text{ t}$); 2 – Mounting plate; 3 – Turn table/goniometer for detector plate (min. load — 700 kg); 4 – Detector plate (load 150 kg); 5 – Support plate (load 100 kg); 6 – Sample turn table; 7 – 2-direction tilting table and manual flat turn table with vertical axis min. load per axis: 600 kg up to $\pm 5^\circ$ tilt max. tilt $\geq \pm 10^\circ$; 8 – Mounting unit for the detector mechanics; 9 – Lifting counter system $+5^\circ / -25^\circ$ vertical tilt and about 0.60 m radius to sample position.

First test experiments

Two experiments with neutrons for components to be tested for the new polarized instrument POLI-HEiDi were done in 2006 at the diffractometer HEiDi. The characterization of the ^3He spin filter cells and the test of the magnetostatic cavity *MB1* at different wavelengths were performed in June 2006 (Exp. Nr. 523 at FRM II). Fig. 3.11 shows the experimentally measured time dependence of the transmission in the ^3He filter cell *Heidi2* situated in *MB1*.

From the data of this experiment all important parameters of the filter cell like ^3He polarization rate, polarizing efficiency, relaxation time constant, cell opacity, etc. could be extracted. A relaxation time constant of about 90 h was measured for this setup.

Another important experiment was performed in August to September 2006 in order to test the feasibility of the MuPAD in combination with a ^3He spin filter polarizer and analyzer for 3D spherical polarimetry with the hot neutrons. During this experiment all three components of the polarization vector for the incident and scattered beam were measured. Polarization matrices for two Bragg reflections of an oriented Si sample were determined.

Fig. 3.12 presents a picture of the experimental setup.

The unpolarized neutron beam with a wavelength of 1.165\AA from the focused Ge-(311) monochromator came from the right hand side in fig. 3.12. The rotating magnetic box HERO-Pol with filter cell *Heidi1* was used as polarizer. The MuPAD was fixed on a support table specially designed for this experiment and was used as zero field sample environment for a cubic silicon single crystal (size about 120mm^3). The existing diffractometer HEiDi was connected to the outgoing arm of the MuPAD and worked in combination with the *MB1* and second spin filter cell fixed in the Eulerian cradle as an analyzer-detector unit.

In both cells relaxation time constants T_1 about 100 h were found. This assures in combination with the typical ^3He start-polarization of the “fresh filled” cells of 70% a mean neutron

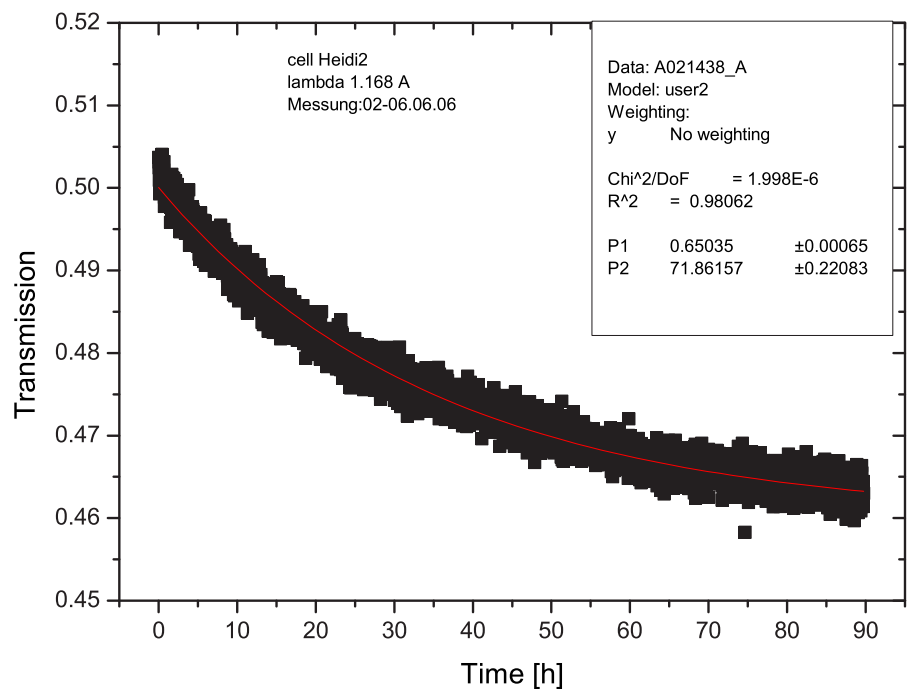


Figure 3.11: Time dependence of the transmission of cell *Heidi2* filled to 1.7 bar, measured in the direct beam

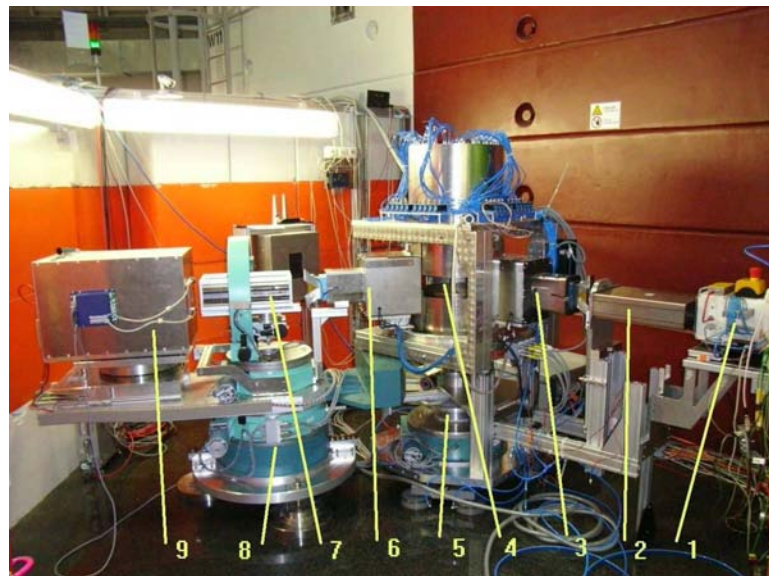


Figure 3.12: Instrumental setup of the MuPAD test experiment. 1 – aperture of the unpolarized monochromatic beam, 2 – HERO-Pol (rotated polarizer with ^3He spin filter cell inside), 3 – fixed incoming arm of the MuPAD with three coils, 4 – Si sample in the zero-field chamber of MuPAD, 5 – support table, 6 – movable outgoing arm of the MuPAD with three coils, 7 – analyzer (with ^3He filter cell inside), 8 – diffractometer basis HEiDi, 9 – detector.

polarization efficiency of about 0.8 during the one day before the new filling is performed. Both analyzer and polarizer cells were repeatedly refilled during the eight days of experiment. High reproducibility of the cells parameters

were experimentally proved. Moreover the function of the rotated polarizer as a mechanical spin flipper was tested. The flipping efficiency of this novel flipper in combination with the coupling coil of

MuPAD was found to be as good as that of the precession coil of the MuPAD.

Further detailed investigations are planned for 2007 (Exp. Nr. 808, FRM II).

Acknowledgements

We would like to thank S. Masalovich and A. Lykhvar from the FRM II neutron optics group for the cooperation in the cell preparation and the engagement during the test experiments. We also would like to thank G. Langen-

stück and F. Tralmer from the construction department and S. Egerland for the work on the MuPAD experiment. Special thanks to J. Krüger for substantial support in the all automation and software questions.

The work is supported by the German Federal Ministry for Education and Science (BMBF project 03HE6AA3).

[1] Lelievre-Berna, E., Tasset, F. *Physica B*, 267, (1999), 21.

[2] Cussen, L. D., Goossens, D. J., Hicks,

T. J. *Nucl. Inst. Meth. Phys. Res. A*, 440, (2000), 409.

[3] Petoukhov, A. K., Guillard, V., Andersen, K. H., Bourgeat-Lami, E., Chung, R., Humblot, H., Jullien, D., Lelievre-Berna, E., Soldner, T., Tasset, F., Thomas, M. *Nucl. Inst. Meth. Phys. Res. A*, 560, (2006), 480.

[4] Hutanu, V., Meven, M., Heger, G. *PNCMI 2006, Berlin, to be published in Physica B*, (2007).

3.3 RESI – The single crystal diffractometer

B. Pedersen¹, G. Seidl¹, W. Scherer², F. Frey³

¹ZWE FRM II, TU München

²Inst. f. Physik, Universität Augsburg

³Sektion Kristallographie, GeoDepartment, LMU München

Status

During the last year RESI was operating without major problems. We installed and commissioned the heavy goniometer with Eulerian cradle option successfully. This allows the use of different sample environments. In the Eulerian cradle geometry the RDK-101 coldhead can be used to reach temperatures down to 2K. Used with the tilting head, the FRM II standard furnace and the sample tube cryostat have been used successfully. This cryostat also allowed the use of a piston-cylinder type pressure cell.

Results

In the last year, commissioning of the single counter option has been started. To gain optimum performance we performed extensive tests on our counter tube together with the detector group. The tests showed a high efficiency of the chosen 17 cm end-window ³He counter tube. The linearity has been tested and a low dead time can be achieved up to count rates of about 30kHz.

With the analyser option installed, first scans on some selected test samples could be performed. The results show a reflectivity of 30% for the Ge-(111) analyzer.

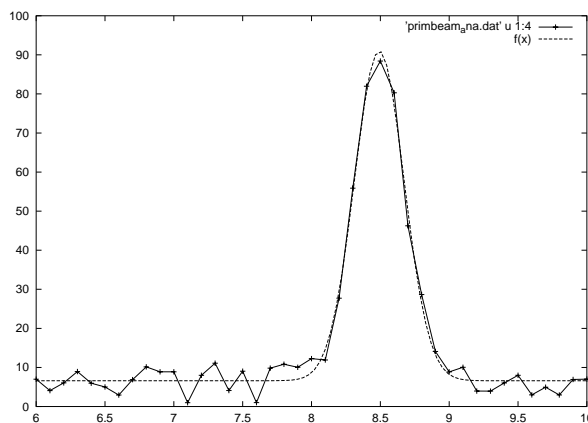


Figure 3.13: Analyzer rocking scan of the primary beam.

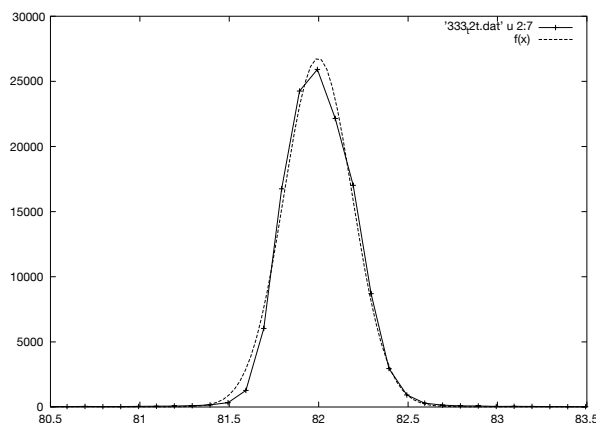


Figure 3.14: $\theta - 2\theta$ -scan of the [333] reflection of quartz with analyzer

In the last year we also performed an intensive study on quasi crystal structures together with T. Weber and W. Steurer (ETH Zürich). A $3 \times 3 \times 3 \text{ mm}^3$ sized sample of a decagonal $\text{Al}_{72}\text{Co}_8\text{Ni}_{20}$ quasicrystal was used and 7277 reflections could be integrated. The data was used for higher-dimensional structure refinement (Th.

Weber, ETH Zürich). Structure solution by the charge-flipping method gave a clear real space picture of the atomic distribution, in particular of the transition metals Ni and Co. A second specimen of the sample was prepared and measured by x-rays. A comparison of the neutron and x-ray data gave for the first time a clear indication of transition

metal order, which was unknown so far, as Co and Ni are hard to discriminate with x-ray-methods.

Outlook

The next big step to finish is the commissioning of the single counter option with analyzer.

3.4 Structure Powder Diffractometer SPODI

M. Hoelzel^{1,2}, A. Senyshyn^{1,2}, R. Gilles², H. Boysen³, H. Fuess¹

¹TU Darmstadt, Material- und Geowissenschaften

²TU München, ZWE FRM II

³Ludwig-Maximilians-Universität, Depart. für Geo- und Umweltwissenschaften, München

Results

In the beginning of 2006 two major improvements lead to a significant increase in the efficiency of the Structure Powder Diffractometer SPODI. A secondary wavelength contamination ($\lambda = 1.983 \text{ \AA}$ with relative intensity of ca. 4 %), existing together with the nominal wavelength, has been eliminated by the replacement of a faulty wafer stack crystal. Thus, a purely monochromatic neutron beam is now available for Ge(551) setting. For the standard configuration with a monochromator take-off angle of 155° the Ge(551) yields a wavelength $\lambda = 1.548 \text{ \AA}$. At the same monochromator take-off angle, additional wavelengths can be selected using different (*hkl*) planes by a ω -rotation of the monochromator: Ge(331) results in $\lambda = 2.537 \text{ \AA}$, Ge(771) in $\lambda = 1.111 \text{ \AA}$. Further, the installation of additional shielding for each of the 80 detectors resulted in drastic improvements in the signal to background ratio.

All components of the sample environment available at SPODI have been set into operation in the frame of user measurements. The closed-cycle cryostat ("Kaltkopf-Kryostat"), the closed-cycle refrigerator ("Probenrohrkryostat") as well as the high temperature vacuum furnace are now in routine operation. In summer 2006 first experiments using a high-pressure cell of the Paris-Edinburgh VX3 type have been successfully carried out, allowing

pressures up to 10 GPa. Additionally, a load frame for materials testing has been set into operation and used for *in-situ* analysis of shape memory alloys. The load frame allows flexible programming for materials testing, e.g. in the determination of stress-strain curves. Its application at SPODI enables the simultaneous study of mechanical behaviour and structural changes, such as phase transformations, lattice expansion/contraction and evolution of microstresses. About 2/3 of the total beam time was given to external users. Within this beam time a number of structural studies have been carried out for a variety of different materials. Some results have either appeared in publications or have been submitted to pertinent journals. For example, in a ZrO_2 sample, partially substituted by Sc and N, the nitrogen position and amount of phase fractions have been determined as a function of temperature together with probable diffusion pathways [1]. Similarly, for zeolite-like sodianite the diffusion processes of lithium [2] were determined. In the oxygen ionic conductor mayenite ($\text{Ca}_{12}\text{Al}_{14}\text{O}_{32}\text{O}$) the positions of "free" mobile oxygen and other ions have been localized within the framework structure using difference Fourier maps, and the diffusion was found to proceed via a site exchange process with framework oxygen [3]. The proper tilt systems have been determined for the high-temperature quantum paraelectrics $\text{Na}_{0.5}\text{Nd}(\text{Pr})_{0.5}\text{TiO}_3$

and $(\text{Na}_{0.5}\text{Nd}_{0.5})_{1-x}\text{Sr}_x\text{TiO}_3$, whose perovskite structures undergo very weak distortions from the prototype cubic structure [4, 5]. In order to reveal the correlations between high ionic conductivity and disorder in AgCuSe and AgCuS, high-temperature structural studies have been done in the temperature range 298-723 K using neutrons and synchrotron radiation. The obtained data were analysed by a combination of whole-pattern decomposition procedure and Rietveld refinement [6]. Proton localization in cement-class material $4\text{CaO} \cdot 3\text{Al}_2\text{O}_3 \cdot 3\text{H}_2\text{O}$ has been performed [7] by analysis of differential Fourier maps for diffraction patterns collected at room temperature and at 5 K.

- [1] Lerch, M., Boysen, H., Rödel, T., Kaiser-Bischoff, I., Hoelzel, M., Senyshyn, A. *J. Sol. State Chem.* Submitted.
- [2] Park, S.-H., Hoelzel, M., Senyshyn, A., Boysen, H., Schmidbauer, E. *J. Sol. State Chem.* Submitted.
- [3] Boysen, H., Lerch, M., Stys, A., Senyshyn, A., Hoelzel, M. *Acta Cryst. B.* Submitted.
- [4] Ranjan, R., Agrawal, A., Senyshyn, A., Boysen, H. *J. Phys.: Condens. Matter*, 18, (2006), 9679.
- [5] R. Ranjan, A. A., Senyshyn, A., Boysen, H. *J. Phys.: Condens. Matter*, 18, (2006), L515.

- [6] Trots, D., Senyshyn, A., Mikhailova, D., Knapp, M., Hoelzel, M., Fuess, H. *J. Phys.: Condens. Matter*. Accepted.
- [7] Peters, L., Knorr, K., Evans, J., Senyshyn, A., Rahmoun, N.-S., Depmeier, W. *Z. Kristal*. Submitted.

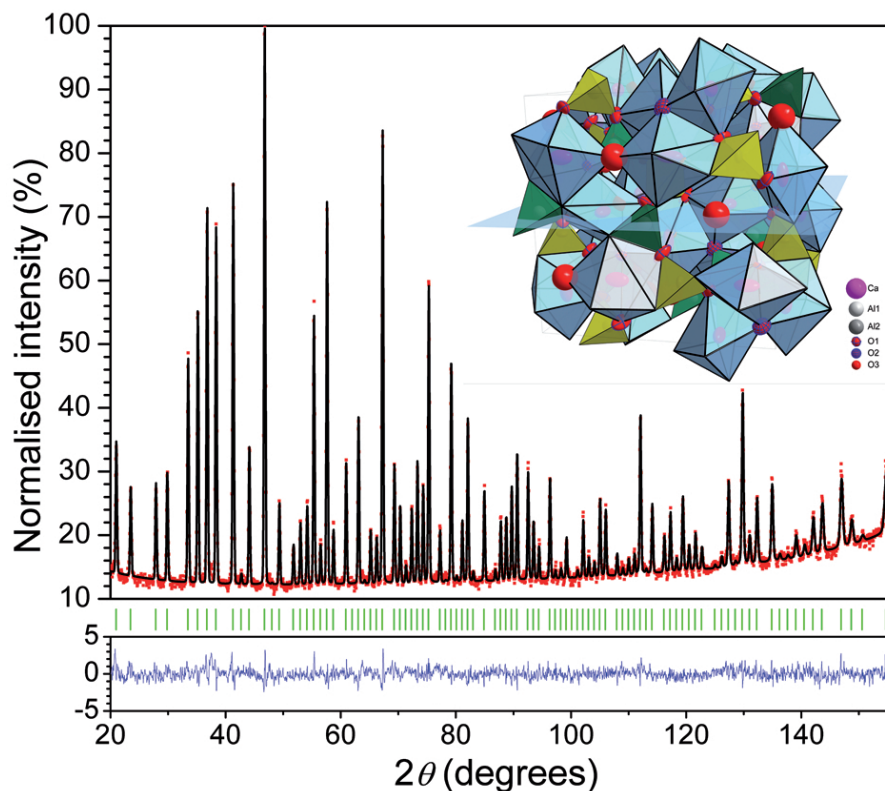


Figure 3.15: Observed, calculated and differential powder diffraction patterns for mayenite at 700 °C. Bragg reflection positions are indicated by vertical bars.

3.5 STRESS-SPEC Materials science diffractometer

M. Hofmann¹, U. Garbe^{1,2}, G.A. Seidl¹, J. Rebelo-Kornmeier^{1,3}, J. Repper¹, R. Schneider³, H.G. Brokmeier⁴

¹ZWE FRM II, TU München

²GKSS, Geesthacht

³BENSC, Hahn-Meitner-Institut, Berlin

⁴TU Clausthal, Clausthal-Zellerfeld

Introduction

The Materials Science diffractometer Stress-Spec is located at the thermal beam tube SR3 and is optimized for residual stress analysis and texture measurements of new materials and engineering components. Its main characteristics and components have been described elsewhere [1, 2] and here only the most relevant developments of the last year will be reviewed.

New hardware

In the beginning of the user cycles 2006 the faulty PG monochromator has been repaired, reinstalled and realigned. Since then it works according to specifications and is now used routinely for texture measurements and experiments which require only medium resolution but a very high neutron flux on the sample. During commissioning experiments it was found that eccentricity of the original z-stage of the heavy sample table was too large with heavy loads. It was therefore replaced by a new z-stage from Huber GmbH

allowing now 320 mm travel (formerly only 220 mm) of the sample in vertical direction. In course of this replacement the distance from the top of the sample table to the beam centreline was increased to 520 mm which allows now to accommodate even larger samples. A 4-point bending test machine and 50 kN load frame (figure 3.16) were specifically developed and build for the diffractometer. The load frame environment kit can be used for in-situ tension/compression strain and texture measurements and low-cycle fatigue experiments.

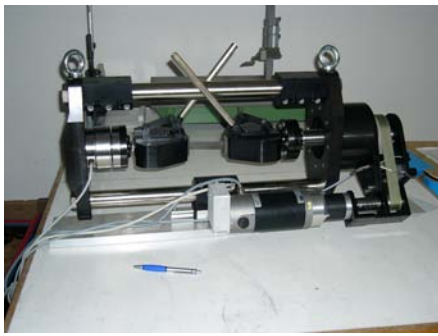


Figure 3.16: 50 kN load frame with grips for flat samples attached.

Experiments

A total of 21 user experiments have been conducted during the year. They covered a wide area of applications in residual stress analysis and texture measurements. Examples in the field of residual stress analysis included residual stress analysis in welds to improve model calculations of postweld heat treatments (J. Francis, University of Manchester), studies of the influence of surface treatments on the strain development in steel rods for construction work (J. Ruiz, University of Madrid) and investigations of strain distribution in geometrically complex components (C. Kremaszky, TUM). Other experiments showed the potential of STRESS-SPEC to investigate large samples such as very thick aluminum plates (M. Fox, University of Manchester) or large steel pipes (L. Edwards, Open University). Also highlighted during 2006 was the ability to produce complete strain maps due to the high neutron flux of the diffractometer. For instance figure 3.17 shows the through thickness transverse residual strain distribution mapped along the centreline of a weld bead on a steel plate (M. Turski, Open University). Here the interest was to investigate weld start and stop effects, where evidence exists for further increases in residual stress for those regions. The results show indeed such an increase and are thought to be significant as such features are common in welded structures. The data will be used to evaluate and improve existing FEM models.

Roughly one third of all experiments

on STRESS-SPEC have been texture measurements. This included the texture development in Mg-Si-Al alloys under ECAP pressing (W. Gan, TU Clausthal), quantitative texture analysis of deformed natural quartz samples (H. Sitepu, Virginia Tech) and texture development and its influence on shape memory properties of Fe-Mn-alloys (R. Bolmaro, University of Rosario). The enhanced flux due to the realigned PG monochromator allowed to continue with the development of methods to measure locally resolved textures. Figure 3.18 shows as an example the local texture of the VAMAS TWA 20 shrink-fit ring and plug sample used before as round robin standard for neutron residual stress analysis [3, 4]. The global texture of this sample was already determined during the stress round robin, however, no information of the local texture was available. For the local tex-

ture analysis on STRESS-SPEC three positions within the sample were chosen to measure the (222) pole figure using a gauge volume of $2 \times 2 \times 2 \text{ mm}^3$. The first point is in the centre of the whole sample giving texture information of the cylinder. Point 3 shows the texture of the ring, at the border between ring and plug (point 2) a mixture of both texture components will be found. Because of the negligible absorption cross section of aluminum it was possible to get reasonable results for pole figures even without a proper absorption correction. The pole figures in figure 3.18 observed at the three points show very similar intensity distributions. Comparing the first and the third pole figure one can recognise a small shift of the maxima around the pole figure normal. Pole figure 2 shows, as expected, a mixture of the texture components in point 1 and 3 [5].

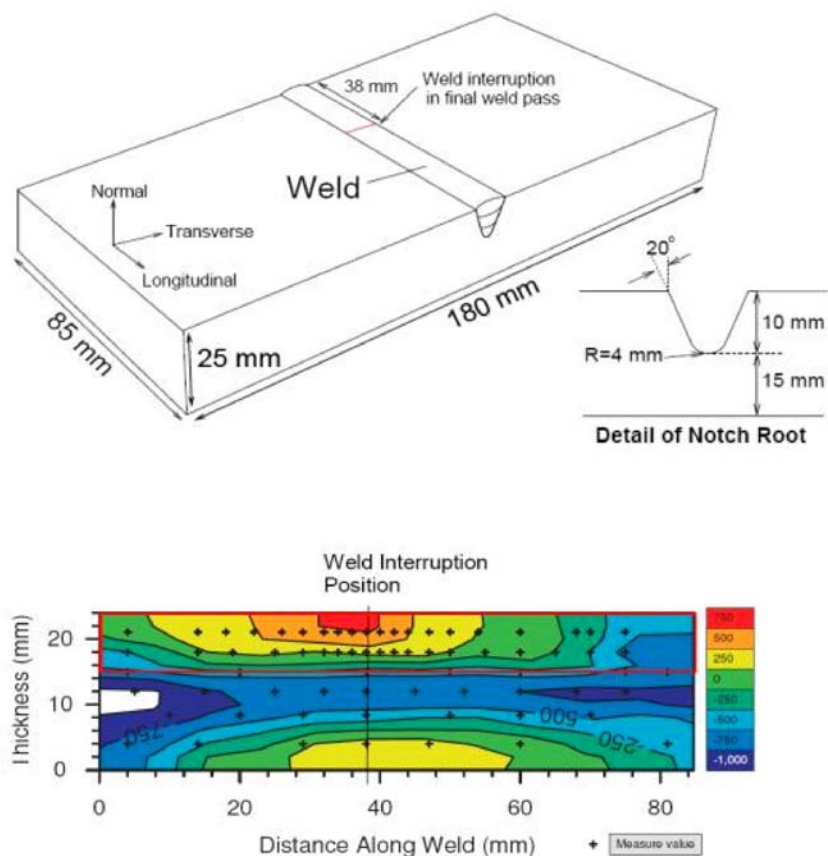


Figure 3.17: Map of transverse residual strain measured in the through thickness/longitudinal plane, along the centre line of the weld bead. Note: The weld metal region has been highlighted with a red box.

Besides the user experiments STRESS-SPEC was also used commercially to investigate strain profiles in different industrial components such as crankshafts, wheel bearings or satellite nozzles.

Outlook

In the new year first experiments with the new sample environment kit are planned to measure samples in-situ with applied loads.

For texture measurements the time to position samples has to be decreased. Developments on a new instrument control software are ongoing and it is planned to test it for the first time with a routine to take texture data continuously while rotating the sample around the rotation angle ϕ at the earliest possible date in 2007. The data analysis software is also further developed with the aim to accommodate texture and strain analysis in one package.

[1] Hofmann, M., Seidl, G., Schneider, R. *Ann. Report FRM-II*, (2003).

[2] Hofmann, M., Seidl, G., Rebelo-Kornmeier, J., Garbe, U., Schneider, R., Wimpory, R., Wasmuth, U., Noster, U. *Mat. Sci. Forum*, 524-525, (2006), 211.

[3] Webster, G. *Proceedings ICRS-6*, 1, (2000), 189.

[4] Hofmann, M., Garbe, U., Seidl, G., Schneider, R., Rebelo-Kornmeier, J. *Ann. Report FRM-II*, (2005).

[5] Garbe, U., Hofmann, M., Brokmeier, H.-G. *Z. Krist.*, (2006).

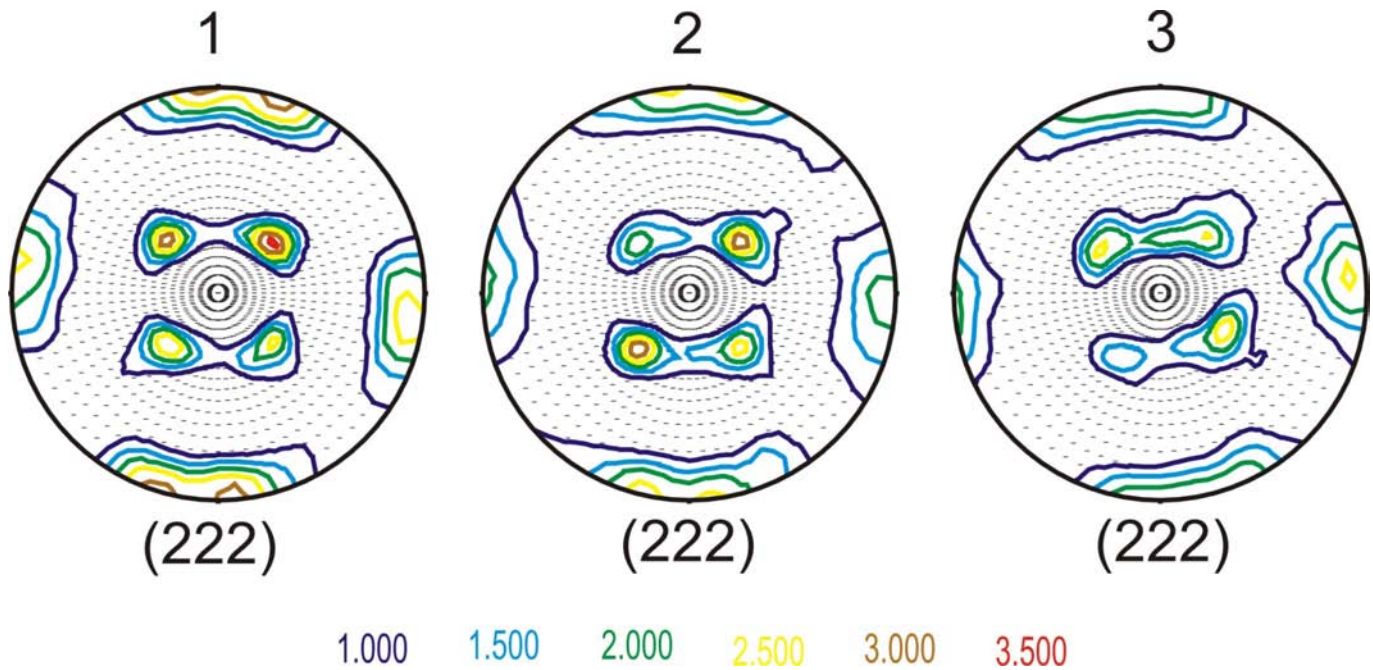


Figure 3.18: (222)-pole figure of the VAMAS sample measured at three different positions as discussed in the text.

4 Inelastic scattering, high resolution

4.1 DNS - A versatile multi-detector time-of-flight spectrometer with polarization analysis

Yixi Su^{1,2}, Werner Schweika², Eckhard Küssel², Klaus Bussmann², Thomas Brückel^{1,2}

¹JCNS, outstation at FRM II, Forschungszentrum Jülich

²Institut für Festkörperforschung (IFF), Forschungszentrum Jülich

Introduction

The diffuse neutron scattering (DNS) instrument is among several selected instruments being transferred from the Jülich research reactor to FRM II. Meanwhile, a substantial upgrade and modernization on most of its major components is being carried out. This will transform DNS into a worldwide competitive instrument in its kind. DNS is a cold neutron multi-detector time-of-flight (TOF) spectrometer with both longitudinal (i.e. XYZ-method) and vector polarization analysis (LPA/VPA) [1, 2, 3]. This allows the unambiguous separation of nuclear-coherent, nuclear-spin-incoherent and magnetic scattering contributions simultaneously over a large range of scattering vector \mathbf{Q} and energy transfer E . With its compact size (only 80 cm distance from sample to detector), DNS is optimized as a high intensity instrument with medium \mathbf{Q} and energy resolutions. DNS is therefore ideal for the studies of elastic and inelastic diffuse scattering that may arise from short-range magnetic and structural correlations and disordering phenomena in a wide range of emergent materials, such as frustrated magnets, highly correlated electrons, molecular magnets and complex nano-structured compounds. Furthermore, interesting applications to soft matter physics by separating coherent and spin-incoherent scattering can also be found at DNS.

Instrument description

DNS uses a vertically and horizontally adjustable double-focusing pyrolytic graphite monochromator, installed in the cold neutron guide NL6a. A schematic layout of DNS at FRM II is shown in Fig. 4.1. Monochromatic neutron beams with a wavelength ranging from 2.4 to 6 Å are available at DNS. The neutron beam is polarized using a $m = 3$ Schärpf bender-type focusing supermirror polarizer. The neutron spins are manipulated using a Mezei-type π -flipper, followed by a set of orthogonal XYZ-coils situated around the sam-

ple position for providing guide fields. The polarization analysis (PA) is performed by using $m = 3$ supermirror analyzers in focusing arrangement in front of each ^3He detector. 128 new position-sensitive ^3He detector tubes will be installed in additional detector banks for non-polarized experiments. This will increase the covered solid angle up to 1.9 sr. Two new high-frequency (rotation frequency up to 300 Hz corresponding to a repetition rate of 900 Hz for 3 slits) chopper systems will be used at DNS, as shown in Fig. 4.1. Chopper-1 is used for selecting a single harmonic from the reflected orders of neutrons

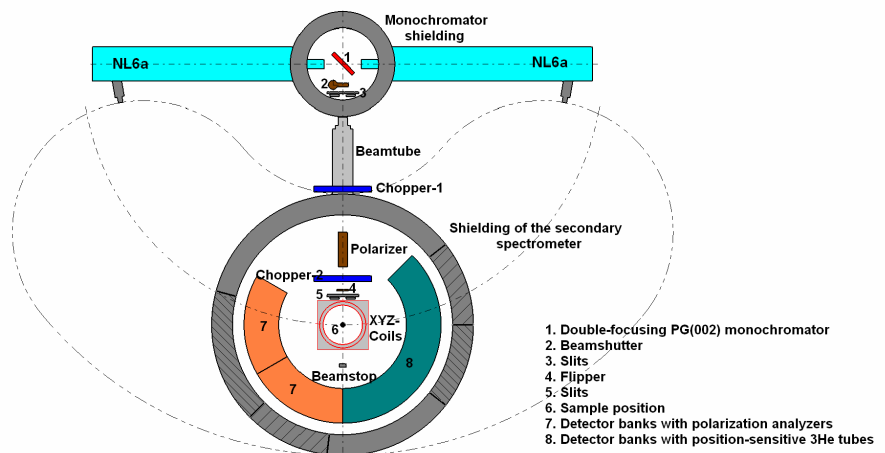


Figure 4.1: The schematic layout of DNS at FRM II

from the monochromator and also for reducing the background. Chopper-2 is the TOF chopper. Various sample environments e.g. cryostat, furnace, dilution cryostat and cryomagnet can be mounted on a heavy loading Huber goniometer on the sample rotation table. The two perpendicular arcs of the goniometer can be used for the orientation of single-crystal samples. The instrument data is summarized in Table 4.1.

In addition to high intensity, the unique strength of DNS lies on its extreme versatility. DNS can be operated in a number of modes for a wide range of samples. There are three PA modes at DNS: *uniaxial* – PA for separation of coherent and spin-incoherent scattering in non-magnetic samples; *longitudinal* – PA (XYZ-method) for separation of magnetic scattering in paramagnetic and antiferromagnetic samples; (*spherical* or) *vector* – PA for determination of

complex magnetic structures. All of these PA set-ups can be operated either in diffraction or in a TOF measurement. With installations of 128 position-sensitive ^3He tubes and double choppers, the performance of DNS as a TOF spectrometer will be drastically improved, thus allowing $\mathbf{S}(\mathbf{Q}, E)$ to be measured simultaneously over a large range of \mathbf{Q} and E on single-crystal samples. As a high intensity cold neutron single-crystal TOF spectrometer, DNS is well suitable for investigations of magnon and phonon excitations in magnetic model systems and complex oxides.

Current status and outlook

In 2006, an increasing number of activities of the DNS project took place at FRM II. The Tanzenboden was built in spring. The monochromator shielding was successfully installed and passed for radiation protection during the

summer break. The improvement of the monochromator shielding was made. Another major development is the permanent placement of the instrument responsible at Garching. The year of 2007 will be crucial for DNS. The installation of the double-focusing monochromator and the relocation of the secondary spectrometer are expected in spring 2007. The delivery of the first neutrons and the starting of the commissioning phase are targeted before the next summer break. The installations of new double choppers and position sensitive ^3He detector tubes are expected to follow suit.

- [1] Schweika, W., Böni, P. *Physica B*, 297, (2001), 155–159.
- [2] Schweka, W. *Physica B*, 335, (2003), 157–163.
- [3] Schweka, W., Easton, S., Neumann, K.-U. *Neutron News*, 16, (2005), 14–17.

Monochromator	horizontal- and vertically adjustable double-focusing crystal dimensions wavelengths	PG(002), $d = 3.355 \text{ \AA}$ $2.5 \times 2.5 \text{ cm}^2$, 5×7 crystals $2.4 \text{ \AA} \leq \lambda \leq 6 \text{ \AA}$
Double-chopper system	chopper frequency repetition rate chopper discs	$< 300 \text{ Hz}$ $< 900 \text{ Hz}$ Titanium, 3 slits, $\phi = 420 \text{ mm}$
Expected neutron flux at sample ($\text{n/cm}^2\text{s}$)	non-polarized polarized	$\sim 10^8$, $\lambda = 3 \text{ \AA}$ $\sim 10^7$, $\lambda = 3 \text{ \AA}$
Detector banks for non-polarized neutrons	position-sensitive ^3He detector tubes	128 units, $\phi = 1.27 \text{ cm}$, height 101 cm)
Detector banks for polarized neutrons	total solid angle covered covered scattering angles polarization analyzers	1.9 sr $0^\circ < 2\theta \leq 135^\circ$ 24 units, $m = 3$ supermirrors)
Q_{max}	^3He detector tubes covered scattering angles $\lambda = 2.4 \text{ \AA}$ ($E_i = 14.2 \text{ meV}$) $\lambda = 6 \text{ \AA}$ ($E_i = 2.28 \text{ meV}$)	24 units, $\phi = 2.54 \text{ cm}$, height 15 cm) $0^\circ < 2\theta \leq 120$ 4.84 \AA^{-1} 1.93 \AA^{-1}
Expected energy resolution	$\lambda = 2.4 \text{ \AA}$ ($E_i = 14.2 \text{ meV}$) $\lambda = 6 \text{ \AA}$ ($E_i = 2.28 \text{ meV}$)	1 meV 0.1 meV
Suitable samples	single crystals, powders, soft matters (e.g. polymer, liquid etc.)	
Sample environments	closed-cycle cryostat, orange-type L-He cryostat, furnace, dilution cryostat, cryomagnet (up to 4T)	

Table 4.1: Instrument data of DNS at FRM II

4.2 J-NSE – The Jülich neutron spin echo spectrometer

O. Holderer¹, M. Monkenbusch¹, R. Schätzler¹, D. Richter¹

¹JCNS, outstation at FRM II, FZ-Jülich

Introduction

The Neutron Spin Echo Spectrometer was successfully in operation at the FRJ-2 since 1996. Routine use there was limited to neutron wavelengths around 8 Å and up to a magnetic field integral of 0.25 Tm, giving access to a max. fourier time τ of 22 ns. It has been moved from the Jülich Research reactor FRJ-2 to the FRM II at the beginning of 2006. Since then, mechanical, electrical and electronical installations have been carried out.

Activities

To adapt to the beam height at the FRM II which is about 24 cm below that at Jülich, the carrier structure of the spectrometer arms has been reconstructed. The correction elements are now mounted on motor controlled positioning devices enabling more precise adjustment. The neutron guide system had been designed and installed as reported earlier [1]. Extra lead shielding around the neutron entrance into the instrument has been installed, first measurements indicate that –after positioning mobile lead walls on the boundary to the Mephisto area– the radiation levels outside the Tanzboden stay within $3\mu\text{Sv}/h$. The electrical installations, cabling of all coils, sensors and motors, took place in 2006. Electrical power and water cooling that comply to the 200KW maximum power consumption of the main coils has been passed to the instrument position. The electronics of the spectrometer has been modernized. In particular new power supplies (except that for the main coils) have been installed, all current sources as well as the SPS modules for hardware control are equipped with profibus interfaces. The hardware (powersupplies, motors, sensors) is now controlled with Taco servers according to the "Jülich Münchner Standard".

Performance of J-NSE

The performance of the spectrometer will largely improve at the FRM II due to several reasons. The spectrometer is now located at the end of the neutron guide NL2a-o[1], which enables us to select the wavelength in the range of about 4.5 to 16 Å. Short wavelengths (up to about 8 Å) will be polarized in a bent FeSi polarizing neutron guide inside the casemate. For larger wavelengths, a polarizer will be employed that is installed at the end of the neutron guide. The cross section of the guide at exit is 60x60 mm. New correction coils have been designed and manufactured, the new backplate avoids loss of geometrical precision and yields better heat removal, use of pure Al instead of AlMg3 results in smaller electrical resistance and better heat conduction. This allows the use of higher currents corresponding up to a maximum field integral of 0.5 Tm of the main precession coils. Tests in Jülich during the last NSE cycle there showed the path to a further necessary modification in the correction coil shape that will improve the correction efficiency. The thus designed coil generation with oblique cuts is under production at the FZJ and will replace the current generation after the first operation cycle.

The neutron flux at the exit of the neutron guide NL2a-o has been measured with gold foil activation analysis (in collaboration with K. Zeitelhack, TUM). The results are presented in Figure 4.4. At $\lambda = 7 \text{ \AA}$, the flux is about 15 times higher than it was at the neutron guide exit at the FRJ-2, in addition the beam cross section at FRM II is 2.7 larger than that in Jülich. The flux has been compared to McStas simulations (although made with a simplified cold source). The simulated flux agrees reasonably well with the measured values. At higher wavelengths, the neutron flux is smaller than predicted, an observation made also with more sophisticated models of the cold source.

The larger neutron guide exit, the higher flux and the better correction elements push the performance of the instrument to fourier times $\lambda = 1 \text{ ps}$ to $\sim 350 \text{ ns}$, with a q-range of $q=0.02-1.5 \text{ \AA}^{-1}$

Outlook

First test with neutrons have been performed at the end of 2006. Currently we work on the final function tests and parametrization of the new software and hardware modules which then will be integrated into the operation software according to predefined and prepared routes. The first experiments with neutrons will be used to complete the parametrization and testing work and will allow final adjustment of the corrections. In addition circuitry for maintaining He-atmosphere along the neutron flight path has to be installed and the detector shielding must be optimized. If the thus obtained resolution functions are satisfactory first test experiments may be performed.

[1] Breunig, C., *et al.* *Annual Report 2005 FRM-II*, 18–19.



Figure 4.2: One of the two main precession coils of the J-NSE spectrometer entering the neutron guide hall



Figure 4.3: The NSE spectrometer during installation in the neutron guide hall.

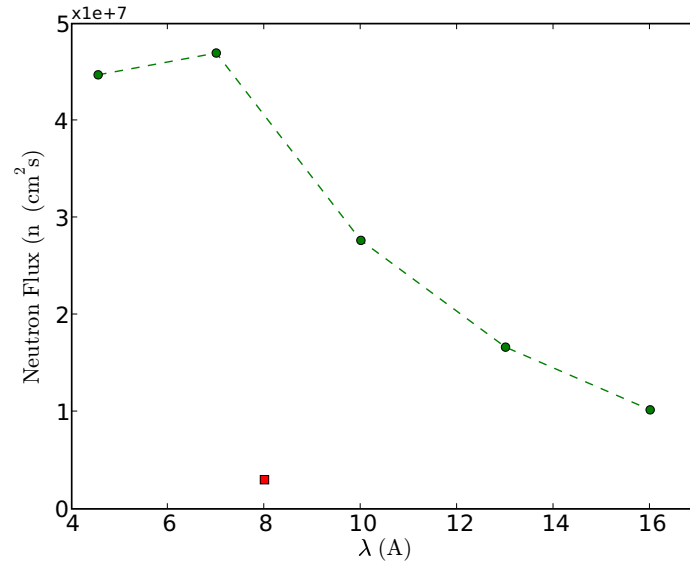


Figure 4.4: Neutron flux at the end of the neutron guide NL2a-o. For comparison, the flux at the FRJ-2 is shown (red square).

4.3 First quasielastic measurements at RESEDA

Wolfgang Häußler², Dominik Streibl¹, Reinhard Schwikowski², Andreas Mantwill¹, Bodo Gohla-Neudecker², Rodrigo Caballero², Peter Böni¹

¹Physik-Department E21, TU München

²ZWE FRM II, TU München

In 2006, first quasielastic scattering measurements at the Resonance Spin Echo (NRSE) Spectrometer RESEDA have been performed. In order to prepare RESEDA for these experiments, intensity and polarization of the primary beam were optimized. At first, high radiation background produced in the first spectrometer arm and at the sample region (4.5) was shielded with movable lead walls. Now, usage of the full beam is possible at RESEDA, in contrast to previous measurements using attenuators in front of the spectrometer. Test measurements of the polarization as a function of the wavelength of the primary beam and its divergence were performed. Thereafter, the guide field

around the polarizing guide was enforced from 80 G to 250 G. These measures improved the polarization. However, it was still not perfect, especially at high beam divergence.

Nonetheless, the performance of RESEDA could be demonstrated by first quasielastic test experiments. The sample consisted of the protein Cytochrome C (140 mg/ml) in aqueous solution. The velocity selector was operated at 22000 rpm, providing the mean wavelength 5.3 Å with a wavelength spread of 12 % (FWHM). We used the NSE setup at small spin echo times (0.01-0.064 ns), the NRSE setup at intermediate (0.16-1.2 ns) and the BNRSE setup at large spin echo times. The RF

frequency was tuned to values between 35 kHz and 371 kHz leading to spin echo times up to 4 ns. Typical intermediate scattering functions are shown in 4.6, together with exponential fit functions. All data have been normalized by the resolution function determined by using a standard elastic scattering sample (graphite). As seen from 4.6, the decay rate of the relaxation function increases with increasing scattering vector values Q , as expected for center-of-mass diffusion. The decay rates are in good agreement with the Cytochrome particle size (15x17x17 Å³). The size of the error bars is comparable to the symbol size, and this is due to the still not optimum primary beam polarization.



Figure 4.5: The instrument RESEDA with its two secondary spectrometer arms. The mu-metal shielding of the left arm is removed and gives free view on the NSE and NRSE coils.

Further optimization of the polarization was abandoned, however, because the whole guide system was anyhow removed after the quasielastic test experiments, due to non-tolerable activation of the polarizing guide. A new guide system is in preparation, and a new polarizer (cavity) will be installed in early 2007 in front of RESEDA. Therefore, the measurements at RESEDA were stopped in July 2006 and, consequently, the progress at RESEDA during 2006 was only possible thanks to efficient use of available neutrons.

During the second half of 2006, several improvements have been

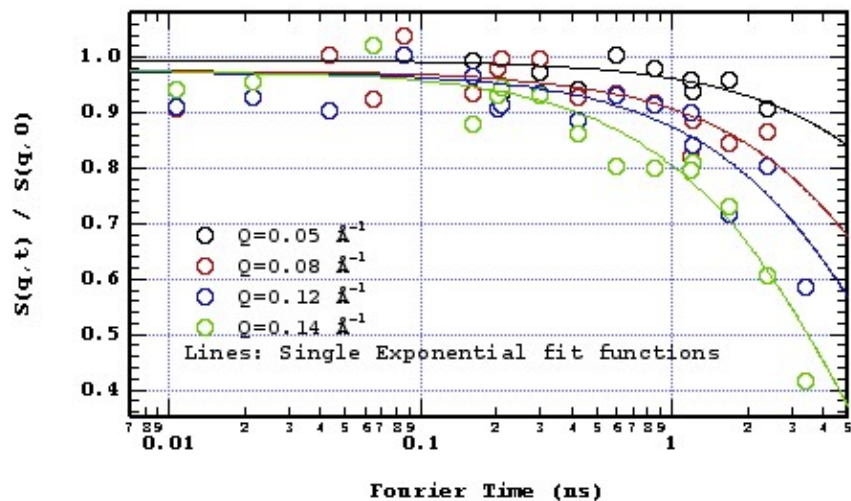


Figure 4.6: Intermediate scattering functions of Cytochrome C measured by means of NSE, NRSE and BNRSE. The scattering angle is varied between 2.5 and 7 degree, leading to the scattering vector values as indicated in the plot.

performed at RESEDA. Almost all axes were supplied with encoders, in order to prevent uncontrolled movement of instrumental components, for example of the sample environment and the detectors. In addition, the NRSE coils are going to be supplied with motorized goniometers and turntables, in order to provide fast and efficient positioning of the coils. Finally, new NSE coils, used for measurements at small spin echo times are in preparation. The previ-

ously used coils produced relatively inhomogeneous magnetic field integrals provoking a resolution gap between the NSE and the NRSE spin echo times. The new coils possess better field integral homogeneity, and, in addition, are designed more compact.

As soon as the new guide system, including the polarizer, is installed in early 2007, RESEDA will be finally commissioned and usable for routine user experiments.

4.4 Commissioning of the backscattering spectrometer SPHERES

Joachim Wuttke¹, Peter Rottländer¹, Wilhelm Bünten¹, Peter Stronciwilk¹, Alexander Ioffe¹, Michael Prager², Dieter Richter², Hans Kämmerling³, Matthias Drochner⁴, Franz-Josef Kayser⁴, Harald Kleines⁴, Frank Suxdorf⁴

¹JCNS, outstation at FRM II, FZ Jülich

²Institut für Festkörperforschung, FZ Jülich

³Zentralabteilung Technologie, FZ Jülich

⁴Zentralinstitut für Elektronik, FZ Jülich

A signal-to-noise ratio of 165:1 is achieved. The energy resolution with unpolished Si[111] crystals is $\delta E_{res} = 0.69 \mu eV$. As a test experiment, the tunneling spectrum of *m*-xylene was measured. A preliminary comparison with the performance of the HFBS instrument at the NIST, USA, is made.

Starting point

The commissioning of the backscattering spectrometer SPHERES (Spectrometer with High Energy RESolution) was continued in 2006. The initial status was:

- A neutron flux of $1.9 \cdot 10^9 \text{ n/cm}^2 \text{ sec}^{-1}$ was determined at the exit of the neutron guide. This is more than estimated originally.

- First test experiments were done.
- The data contained a huge neutron background.
- A large γ background allowed to use the beam only in the presence of radioprotection personnel.
- Shielding restricted the available solid angle.

Technical changes and developments in 2006

- A standard FRM II beamshutter replaced the old one. This shutter is placed more upstream the neutron guide. This operation was necessary to minimize spatial constraints for another Jülich instrument, MARIA. The new shutter improves also the safety instrumentation. It closes automatically on power failure or on interruption of the pressurised air supply.
- The selector has got its dedicated new lead shielding.
- Lead shieldings were installed around the main γ sources in the spectrometer, the PST chopper, the beamstop and the Doppler monochromator.
- A vacuum flight path between PST chopper and Doppler monochromator was implemented, Fig. 4.7. This flight chamber is a prerequisite for a later argon flooding of the instrument, as it reduces argon activation by about an order of

magnitude. The vacuum chamber also increases the neutron flux at the sample by around 20% which were otherwise lost by air scattering.

- Collimations between chopper and monochromator shall prevent primary neutrons from bypassing the chopper.
- A similar collimation is ready to be installed between chopper and sample.
- Diaphragms restricting the view from the sample onto the monochromator were installed.
- Most inner surfaces were covered by boron absorber, either as B_4C/PE composite, or in form of a paint. The result of these measures was, that the γ background outside the spectrometer went almost everywhere below the required $3 \mu Sv/h$. This allows autonomous working with the instrument.
- At the expense of flux a signal-to-noise ratio of 165:1 is obtained.

Systematic measurements revealed two main sources of the remaining background:

- An instantaneous, sample-independent component due to fast neutrons originating from the LiMg absorber in the chopper rotor.
- A retarded background proportional to the scattering power of the sample from neutrons that somehow bypass the chopper while it is closed.

For a 20% scatterer the two sources are of similar importance. The fast neutrons background can be avoided if the absorber on the PST will be exchanged against boron. This will be a major action but will improve the signal-to-noise ratio by a factor of almost 2 for reasonably thin samples. A further factor 2 can be gained if the chopper which for technical reasons actually runs at only 1/3 of its final speed reaches its full operation frequency. Finally, an argon atmosphere will allow about 20% more analyzed neutrons to reach the detectors. With these factors in mind and cautious extrapolation, we can expect for the final state of the instrument a signal-to-noise ratio above 500. Ways of further improvement are obvious, though technologically challenging, e.g. coating the backside of the chopper with absorber. The effects of such actions on the signal-to-noise ratio cannot be estimated reliably, however.

Progress is also achieved on the side of the data acquisition software. In addition to the Doppler velocity histograms we are ultimately interested in, we now also collect chopper phase histograms. The acquisition program was developed into a daemon that can be controlled and parametrized through a simple TCP interface. Similarly, sample temperature can be set and read by a simple daemon. Parameters like chopper frequency etc are now regularly written to a log file. Another process logs human interventions and error states. The entire software is designed such that a graphical user interface can easily be added on top of it.

The actual status of the instrument is presented by two spectra. The elastic spectrum, Fig. 4.8, documents the signal-to-noise ratio of 165:1 at an energy resolution of $\delta E_{res} = 0.69 \mu eV$



Figure 4.7: Newly installed vacuum flight chamber between the PST chopper (right side) and the Doppler monochromator (left side).

FWHM. The measuring time was ~ 12 h. Fig. 4.9 shows a tunneling spectrum.

M-xylene was used as test sample since it was previously measured on the equivalent HFBS instrument at the NIST, USA. In both experiments the signal-to-noise ratio was rather similar and below 100:1. The energy resolution, FWHM, is better on SPHERES while the low intensity wings of the resolution function is less pronounced on HFBS. For SPHERES the energy resolution looks rather independent on energy transfer. This is due to our Doppler monochromator drive based on air bearings, which allows an almost friction free movement compared to the more vibration sensitive cam drive of HFBS.

The improvements of the instrument are going on.

[1] O. Kirstein, R. D., M. Prager, Desmedt, A. *J.Chem.Phys.*, 122, (2005), 14502.

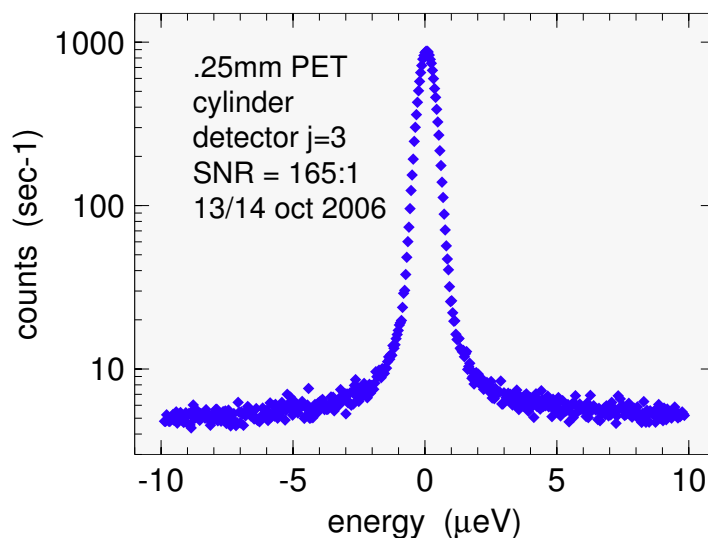


Figure 4.8: Resolution curve, measured on a 0.25mm thick polyethyleneterephthalat sample.

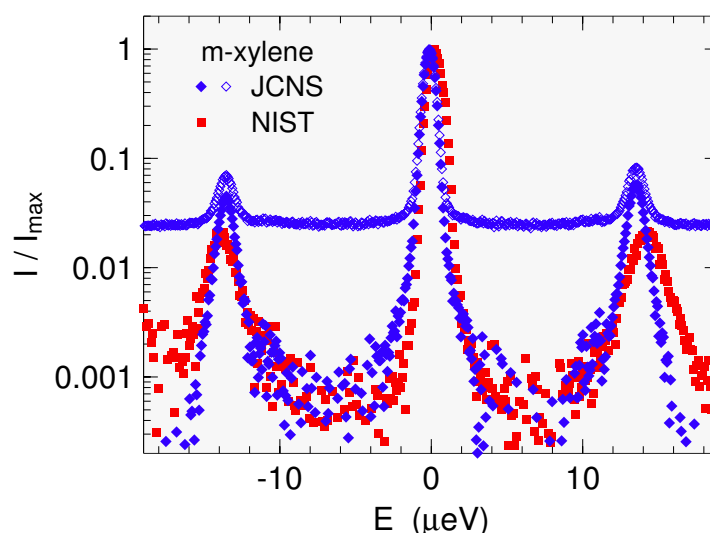


Figure 4.9: Tunneling spectrum of *m*-xylene measured on SPHERES (blue) and HFBS (red) [1]. Normalization to same peak intensities. Sample temperature $T=5$ K. Momentum transfer: $Q \sim 1.7 \text{ \AA}^{-1}$. Open symbols: raw data; closed symbols: after subtraction of a flat background.

4.5 TOFTOF back in successful operation

T. Unruh¹, J. Ringe¹, J. Neuhaus¹, W. Petry^{1,2}

¹ZWE FRM II, TU München

²Physik Department E13, TU München

After the successful startup of user operation of the TOFTOF spectrometer in July 2005 a damage of the very first part of the neutron guide, which feeds TOFTOF and the reflectometer REFSANS with neutrons from the cold source of the FRM II, interrupted the operation of both instruments for half a year. With the reactor cycle no. 6, which started at the end of March 2006,

TOFTOF came back to full operation. A lot of exciting experiments were performed already in this cycle, as e.g. the first TOF experiment on highly supercooled Ni-melts held and heated by electromagnetic levitation (cf. section 9.5).

Although TOFTOF restarted only in March 28 different experiments could be performed in 2006 in addition to

the work on instrument maintenance and optimization. A major task during the experiments was to optimize the sample environment for the needs of the experimentalists. Thus a “bio-furnace” for the medium temperature range (-30°C–180°C) was developed and successfully tested. With this furnace it is now possible to control the temperature of a sample with an accuracy of about 0.1°C in the specified temperature range. The furnace can be pre-cooled or heated and therefore the sample can be inserted at a well defined temperature. The space around the sample can be evacuated, flushed with gas and controlled for humidity, which has, however, not yet been tested.

First experiments on magnetic systems were performed. Using the ³He-insert inside the standard closed cycle cryostat temperatures below 0.5 K could be achieved. A measurement at 0.5 K on the spin dynamics of an Fe₆-Cluster is displayed in figure 4.10. According to the incident neutron wavelength of 1.8 Å energy transfers up to -23 meV can be detected on the neutron energy loss side of the spectrum. It should be pointed out here that within only 4 h of measuring time very good statistics can be achieved due to the particular high neutron flux of the TOFTOF spectrometer in the wavelength range between 1.6 Å and 3 Å.

At the beginning of 2007 it was decided to provide TOFTOF with 400 additional detectors, which will increase the performance of the spectrometer by a factor of about 1.7. The detectors will be purchased in 2007. As it can be seen in figure 4.11 there is space left for the additional detectors on the racks in the 3rd and 4th row, respectively. Thus a significant upgrade of the instrument is already under way.

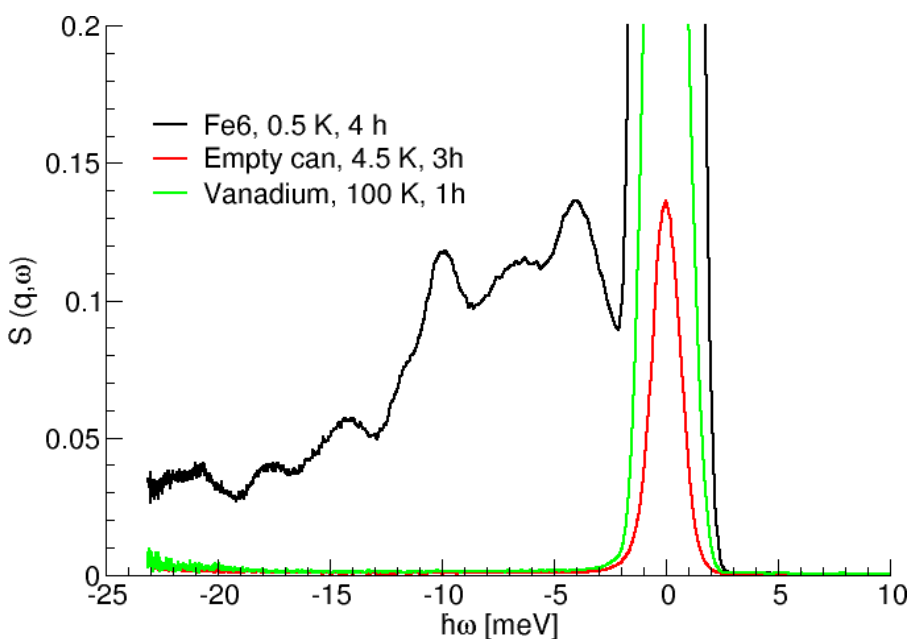


Figure 4.10: TOFTOF spectrum of the compound Fe₆O₂(OH)₂(O₂CMe₃)₁₂·(THF)₂ at 0.5 K. The measurement was performed to investigate the spin dynamics of an Fe₆-Cluster. For comparison a vanadium and the empty can measurement are displayed too. The sample temperatures and the recording times are given in the legend for all spectra. The data is shown here by courtesy of Tatiana Guidi and Grigore Timco.



Figure 4.11: Panorama of the detector bank of the TOFTOF spectrometer. The detectors are oriented tangentially to the intersection line of the Debye-Scherrer cones and a virtual sphere with a radius of 4 m around the sample position. Beside the detectors only cadmium sheets are visible shielding the detectors against neutrons not coming from the direction of the sample position.

5 Three axes spectroscopy

5.1 PANDA – cold neutron three-axes spectrometer

P. Link¹, A. Schneidewind^{1,2}, D. Etzdorf¹, M. Frontzek², O. Stockert³, M. Loewenhaupt²

¹ZWE FRM II, TU München

²Inst. f. Festkörperphysik, TU Dresden

³Max-Planck-Institut für Chemische Physik fester Stoffe Dresden

Introduction

In the year 2006 PANDA entered into routine operation. Already a broad user community has benefited from the special characteristics of the PANDA spectrometer. Apart from numerous user experiments performed, quite some time on PANDA was dedicated to improve the instrument and the sample environment. In the following a brief summary of the main characteristics and improvements on PANDA will be given. This will be complemented by examples of scientific research performed on PANDA in 2006.

Instrument

Current status and characteristics

Starting with the first neutrons on PANDA in 2005 and the experience with different working options improvements were initiated. Sets of parameters for different working conditions and instrument setups were collected to help users to decide on the best suitable operation mode of PANDA. In February 2006 the monochromatic flux at the sample position was determined by gold-foil activation analysis and using a calibrated monitor for $k_i = 1.5 \text{ \AA}^{-1}$ and $k_i = 2.662 \text{ \AA}^{-1}$. The measurements were carried out with the monochromator being vertically focused and horizontally flat, the virtual source set to 40 mm width using no collimation and the appropriate higher order filters in the incoming beam (170 mm Be Filter, LN₂ cooled and 60 mm PG Filter; 3.5° mosaicity, respectively). The obtained values of $1.9 \times 10^7 \text{ n/cm}^2/\text{s}$ ($k_i = 1.5 \text{ \AA}^{-1}$) and

$5.5 \times 10^7 \text{ n/cm}^2/\text{s}$ ($k_i = 2.662 \text{ \AA}^{-1}$) agree well with our expectation for this operation mode. The measured experimental background was decreased to less than 1 count/min for small $k_i \leq 1.5 \text{ \AA}^{-1}$ and standard TAS scattering angles. To further reduce the background especially at small scattering angles a vacuum box with a diameter of 60 cm around the sample was built and successfully tested during an experiment on a multilayer system. This vacuum box substantially reduces air scattering which otherwise would give rise to an increased background at small \mathbf{q} .

To increase the incoming intensity the PG monochromator focus drives were reconstructed and prepared for automatic tracking with k_i changes. A user test experiment was performed with a prototype of an elliptic neutron guide to focus the neutron beam on a tiny sample size suitable e.g. for high pressure cells. The peak intensity in the obtained central spot of $2 \times 2 \text{ mm}^2$ showed an increase by a factor of ten in comparison to the absence of the elliptical guide. Measuring nuclear and magnetic Bragg peaks of a NiS₂ [1] single crystal with dimensions $1 \times 1 \times 0.1 \text{ mm}^3$ the signal gain was about a factor of two.

Two magnets are now available for experiments on PANDA, the 7.5 T and the 15 T magnet. The special sample environment of PANDA, the 15 T cryomagnet including the dilution low temperature insert, was commissioned and put into user operation mode. It was successfully used for about 25% of the total beam time (in close arrangement with the positron source group). Very recently, the 7.5 T cryogen free verti-

cal magnet of the FRM II sample environment was tested for the first time on PANDA and necessary technical improvements for inelastic scattering experiments were initiated.

The alignment of the instrument and of the sample in its cryogenic environment was strongly simplified by adapting the DELCam 2D neutron camera developed by the FRM II detector group. Such a camera is now permanently available on PANDA.

Future upgrades

Apart from routine operation for user experiments the first half of 2007 will see the commissioning and test of the polarisation analysis option using both Heusler monochromator and analyser. In addition a BeO filter has been ordered. Such a BeO filter option was requested by many users and will be used at $k_f \leq 1.3 \text{ \AA}^{-1}$ when high energy resolution is required. As a new sample environment component a VariOx cryostat will be delivered end of March to allow experiments with 1.5 K base temperature and to serve as a "host cryostat" for the Kelvinox dilution insert.

Science

The PANDA spectrometer has seen in 2006 an already broad user community which is still growing. So far, 17 external user experiments have been performed. Not only German user groups but also a large number of European experimentalists and even guests from the United States were hosted. The scientific subjects covered by the users range from ferro-electric substances, low dimen-

sional quantum magnets, frustrated magnets to strongly-correlated electron systems like High- T_c superconductors or heavy-fermion systems. For most of the experiments the special sample environment available on PANDA, i.e., the 15T magnet together with the dilution insert, was indispensable for the success of the experiments. The two examples given below are in the fields of frustrated magnetism and spin dynamics in heavy-fermion systems where the measurements on PANDA revealed new insight into the complex behavior of magnetism in condensed matter physics.

Temperature and field dependent magnetic structures in Tb_2PdSi_3

The series of $R_2\text{PdSi}_3$ (R = rare earth) compounds has been in the focus of interest for over 15 years [2]. The compounds crystallize in an AlB_2 -derived hexagonal structure ($P6/mmm$) with a latent geometric frustration. Tb_2PdSi_3 orders antiferromagnetically below $T_N = 23.6\text{ K}$ and exhibits in addition a spinglass like (SGL) phase transition around $T_2 \approx 8\text{ K}$ observed predominantly with ac- and dc-susceptibility measurements [3]. Neutron scattering was performed at E2, HMI Berlin, and PANDA to study the magnetic structures of Tb_2PdSi_3 and to shed light on the origin of the SGL phase transition. In Tb_2PdSi_3 the antiferromagnetic LRO is squared-up in the whole temperature range below T_N . All magnetic satellites of the LRO have a similar temperature dependence. No features of the LRO can be correlated with the temperature T_2 of the additional phase transition. However, antiferromagnetic SRO with a characteristic temperature of $T_2 \approx 8\text{ K}$ was found. Thus, the disorder to SRO transition correlates to the observed SGL phase transition. The SRO is likely to originate from geometric frustration of magnetic moments which are not able to fulfil the antiferromagnetic coupling to all neighbours simultaneously. This frustration effect seems to affect the LRO arrangement only slightly. Applying magnetic fields, the intensities of the LRO reflections decrease dramatically and change fully

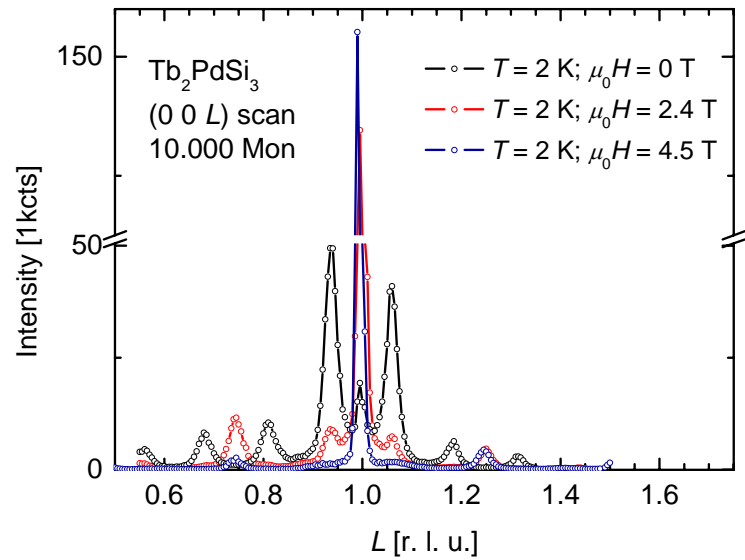


Figure 5.1: (00L) section of Tb_2PdSi_3 at $T = 2\text{ K}$ at different magnetic fields. In zero field (black) the magnetic reflections are on $n/16$ position and relative intensity according to a squared-up arrangement. In intermediate magnetic fields (red) coexistence of two magnetic propagations is observed. Above 3 T (blue) only the antiferromagnetic propagation with the L component of $1/4$ remains.

into a different LRO structure above $\mu_0H = 3\text{ T}$ (see Fig.5.1). The SRO structure vanishes at $\mu_0H = 1.5\text{ T}$, but on equal positions reflection due to an incommensurate arrangement are found. The preliminary results of the investigations in Tb_2PdSi_3 encourage to continue the investigation in the (H, T) -phase space to understand the rich magnetic phase diagram.

Magnetism and superconductivity in the heavy-fermion system CeCu_2Si_2 close to quantum criticality

The heavy fermion compound CeCu_2Si_2 attracts special attention due to the interplay between antiferromagnetic order and superconductivity. Both phenomena exclude each other on a microscopic scale. The system is located close to a quantum phase transition at the disappearance of the antiferromagnetic order. By small differences in crystal growth CeCu_2Si_2 samples can be produced which show either S(uperconductivity),

A(ntiferromagnetism), or both (A/S type). The antiferromagnetic order was previously determined on an A-type single crystal to be an incommensurate spin-density wave below $T_N = 800\text{ mK}$ [4]. The aim of a first experiment on PANDA was to study the superconducting phase of an S-type crystal. Since superconductivity appears below $T_c \approx 600\text{ mK}$, a dilution refrigerator had to be used to reach temperatures well below T_c . Surprisingly, in elastic scans short-range magnetic correlations have been found at the same \mathbf{q} positions where in the antiferromagnetic phase of A-type crystals superstructure peaks have been observed. Fig. 5.2 shows elastic scans taken well inside the superconducting phase of CeCu_2Si_2 at $T = 50\text{ mK}$ and in the paramagnetic phase at $T = 800\text{ mK}$. In the paramagnetic regime these correlations have completely disappeared. The linewidth of these magnetic correlations point to a correlation length of $50 - 60\text{ \AA}$. However, it is so far an open question how these correlations are related to the superconductivity in CeCu_2Si_2 . Further

measurements are planned to look for the response and temperature dependence of these newly discovered correlations in detail.

- [1] Niklowitz, P. G., Mühlbauer, S., Link, P., Böni, P. *FRM II Experimental Report*, (2006).
- [2] Kotsanidis, P. A., Yakinthos, J. K., Gamari-Seale, E. *J. Magn. Magn. Mat.*, 87, (1990), 199.
- [3] Frontzek, M., Kreyssig, A., Doerr, M., Schneidewind, A., Hoffmann, J.-U., Loewenhaupt, M. *J. Phys: Cond. Matter*, 18, (2006), 1.
- [4] Stockert, O., Faulhaber, E., Zwicknagl, G., Stüsser, N., Jeevan, H. S., Deppe, M., Borth, R., Küchler, R., Loewenhaupt, M., Geibel, C., Steglich, F. *Physical Review Letters*, 92, (2004), 136401.

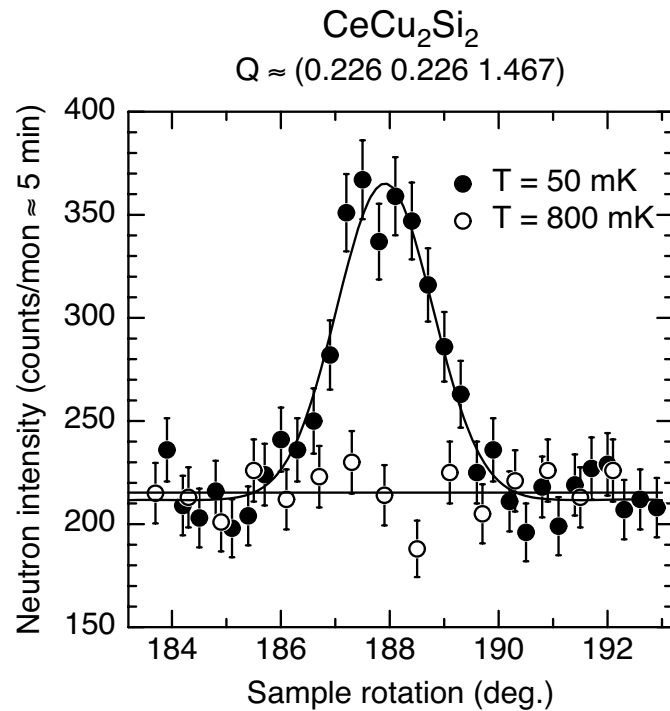


Figure 5.2: Elastic scans taken well inside the superconducting phase of CeCu_2Si_2 at $T = 50$ mK and in the paramagnetic phase at $T = 800$ mK

5.2 PUMA – The thermal triple axis spectrometer

K. Hradil^{1,2}, R.A. Mole², H. Schneider^{1,2}, J. Neuhaus², G. Eckold¹

¹Inst. f. Physikal. Chemie, Universität Göttingen

²ZWE FRM II, TU München

The thermal triple axis spectrometer is installed at the beam tube SR7. During the last year PUMA in its basic version with the single detector began routine operation. Approximately 150 days have been assigned to external users (for results see experimental reports). Additionally the first time resolved measurements in dependence of an applied electrical field both on satellite and phonon scattering could be performed.

New hardware and characterisation

The new Cu(220) monochromator bending device built in the workshop of the University Göttingen could be implemented and allowed measurements

of energy transfers up to 20 THz. Fig. 5.3 shows the monochromator within the exchange unit of the four monochromators (left) and on the test device (right). The high quality of the monochromator proven by rocking scans with a FWHM of 0.4° measured on the PUMA instrument illuminating a horizontal and vertical area of the monochromator of 70 by 150 mm respectively, for $k_i = 2.662 \text{ \AA}$. The performance of the individual Cu crystals as mounted on the bending device were analysed on the STRESS SPEC instrument by rocking scans which revealed a mean FWHM of $0.37^\circ \pm 0.03^\circ$. High energy excitations investigated during a test measurement on a $\text{La}_{1.95}\text{Sr}_{0.05}\text{CuO}_3$ crystal result in comparatively short measurement

times and excellent resolution characteristics.

During the start-up phases of the individual reactor cycles we continued to characterise both the PG(002) and the Cu(220) monochromator. The energy resolution characterisation as determined by using a vanadium standard



Figure 5.3: left: Cu(220) monochromator within the change unit; right: with the bending test unit

sample for different instrument configurations are shown for PG(002) in fig. 5.4 and Cu(220) in fig. 5.5 respectively. The comparison to resolution calculations clearly demonstrates the outstanding quality of the monochromator devices.

The focussing options for the Cu(220) monochromator were also investi-

gated by using a CCD camera developed for tomography. The neutron beam profiles on sample position obtained for both a flat and focussed Cu(220) monochromator are shown in fig. 5.6 and fig. 5.7, respectively. The homogeneity of the intensity distribution on the sample position for the

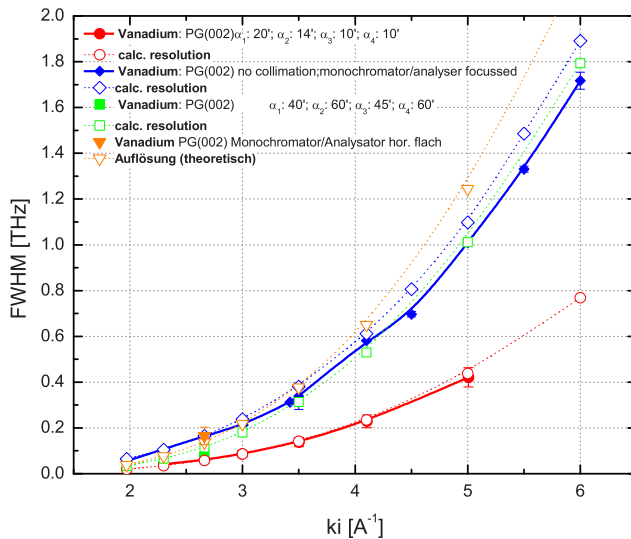


Figure 5.4: energy resolution of the PG(002) monochromator for different instrument configurations

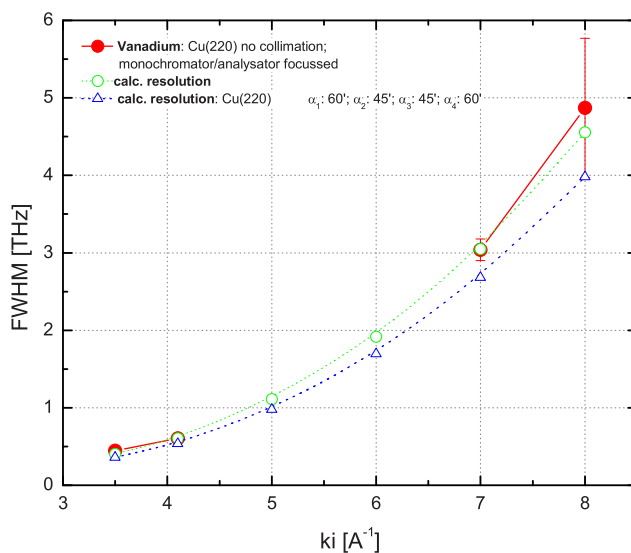


Figure 5.5: energy resolution of the Cu(220) monochromator for different instrument configurations

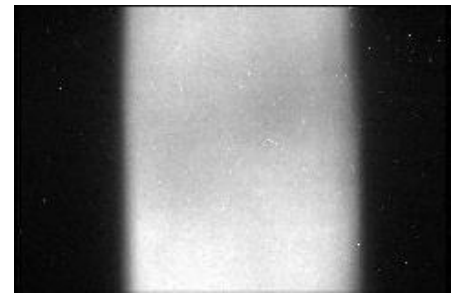


Figure 5.6: CCD camera picture of the beam profile on sample position for flat monochromator

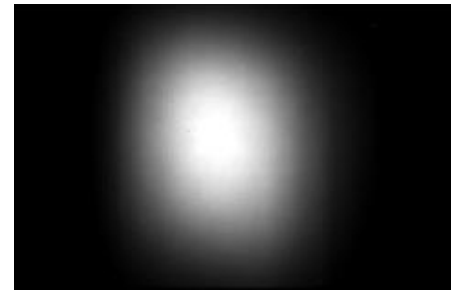


Figure 5.7: CCD camera picture of the beam profile on sample position for focussed monochromator

flat monochromator as well as the focussing properties prove also the excellent quality of the monochromator setup.

Beside the 2 cryostates (3-300K, 15-800K) and a furnace (up to 1200K), we succeeded in putting the Paris Edinbrough pressure cell into operation which allows us to investigate excitations with an applied pressure up to 10 GPa. The cell mounted on the goniometer of PUMA for an external user experiment is shown in fig. 5.8. Although the experiment results in data with reasonable statistics, the intensity for higher pressures was reduced by a factor 3-4 due to the small opening of the anvil cell in comparison to the large dimensions of the beam. To overcome this problem we plan to install special focussing ($m > 5$) in front of the sample.

Apart from the user program, several measurements using the stroboscopic measurement technique could be performed on the instrument. Fig. 5.9 shows the intensity distribution for different time channels for a satellite reflection in K_2SeO_4 at 94.7 K with/without applied electrical field.

The reaction time for the lock-in transition was found to be temperature dependent and varies between 0.5 and 2 ms.

Outlook

Further developments of the instrument will include the full implementation of the stroboscopic measurement technique and the implementation of the multianalyser/-detector.

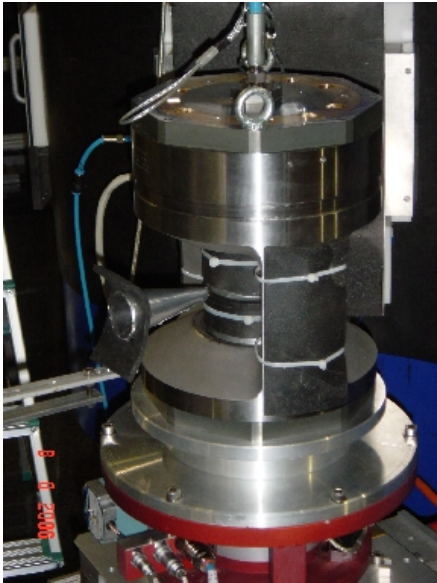


Figure 5.8: Paris Edinborough pressure cell on the goniometer table

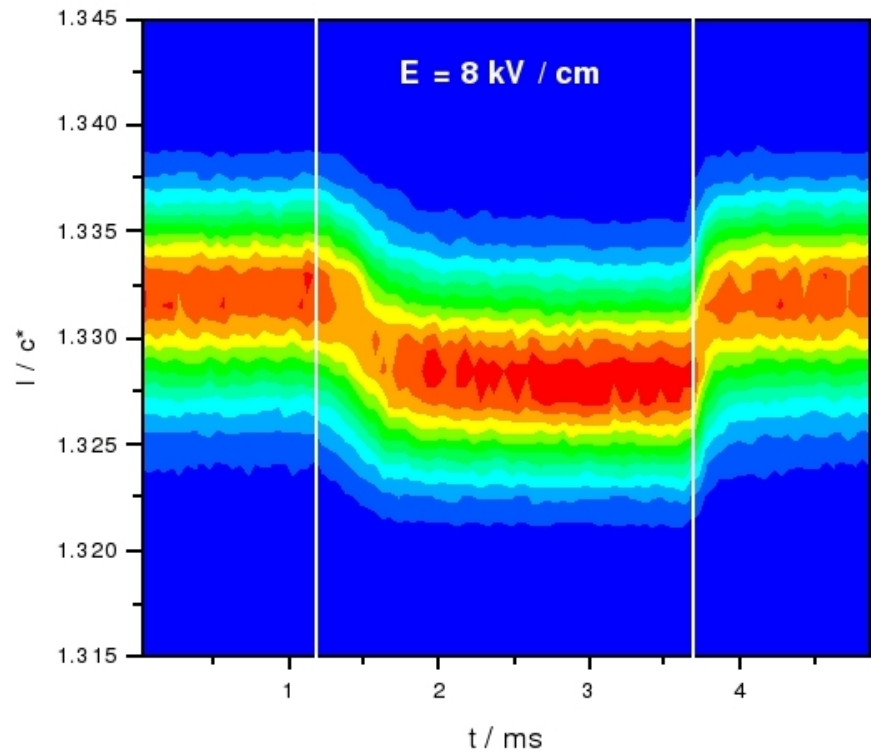


Figure 5.9: time resolved intensity distribution for the first order satellite reflection ($2\ 0\ 4/3-\delta$) in dependence of an applied electrical field

6 Imaging at ANTARES and NECTAR

6.1 Observation of the filling level of the FRM II cold source by pinhole neutron radiography

B. Schillinger¹, Elbio Calzada¹, Christian Müller¹

¹ZWE FRM II, TU München

Abstract

The ANTARES facility for neutron imaging is situated at beam port SR4 facing the cold source. By using a 2 mm pinhole, the surface of the cold source was imaged onto the detector. At low power during reactor startup when the liquid D_2 was not boiling yet, the filling level of the cold source was observed. From the geometrical parameters of this projection, the filling level of the cold source was calculated.

The cold source and the ANTARES facility

During reactor shutdown, the liquid D_2 filling of the cold source of the FRM II reactor is transferred to a hydride storage system. The refilling of the cold source before startup is a difficult process, where the exact amount of deuterium filling of the cold source is not easy to determine.

The ANTARES facility is situated on beam port SR4b facing the cold source (fig. 6.1).

ANTARES possesses an external secondary shutter outside of the drum shutter in the biological shielding. Behind this secondary shutter, a selector wheel is mounted containing different pin hole apertures for phase contrast imaging (Fig. 6.2).

The cold source is a slightly tilted container filled with liquid D_2 . To homogenize the flux and to minimize self-absorption, it contains a hollow displacement body shaped like an inverted cup (Fig. 6.3, Fig. 6.4). After filling, the container and the cup contain liquid D_2 to a certain filling level. When

the reactor reaches power, the D_2 starts to boil. The displacement body fills with gas and displaces the liquid inside, thus raising the liquid level outside the cup. The beam tube SR4 feeding the ANTARES facility faces the surface of the cold source. In normal operation, the effective pinhole camera geometry of ANTARES images an unsharp projection of the surface of the cold source onto the sample area, leading to a homogenous flux distribution. If one of the small pinhole diaphragms intended for phase contrast imaging is used, a sharp well-defined projection of the surface itself is imaged onto the camera.

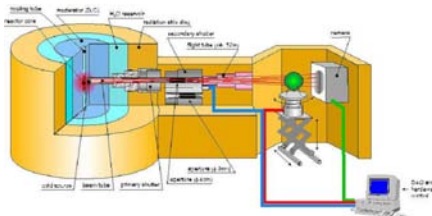


Figure 6.1: Schematic view of the ANTARES facility. The whole imaging facility is built in a pin hole camera geometry, imaging the surface of the cold source onto the sample area.

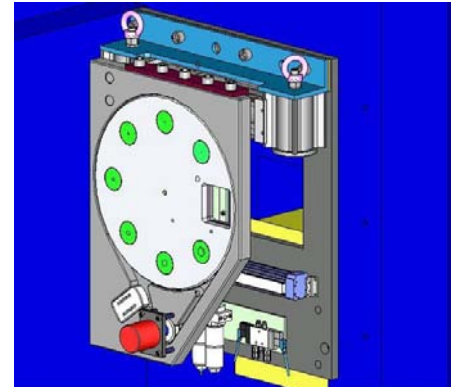


Figure 6.2: Selector wheel for various pinholes.

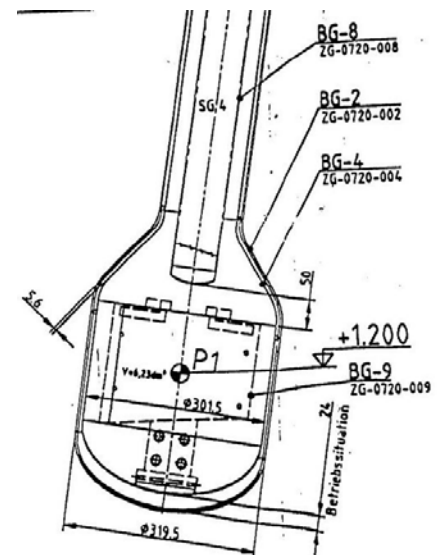


Figure 6.3: Drawing of the displacement body inside the cold source.

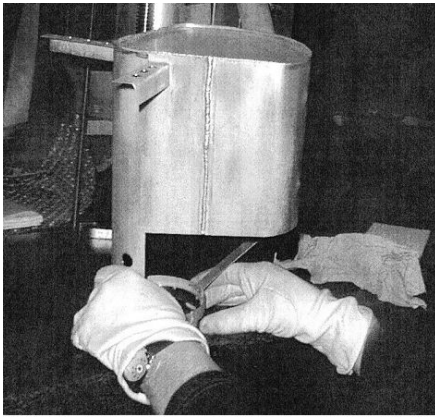


Figure 6.4: Photo of the displacement body.

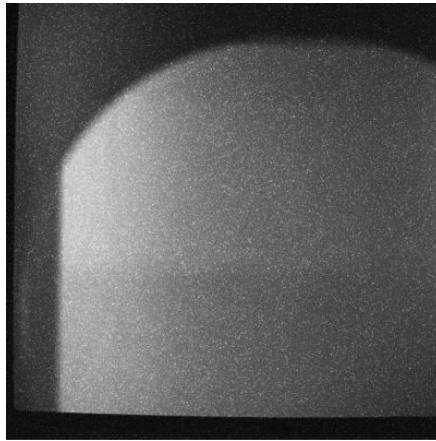


Figure 6.5: The cold source at 3 MW with the filling level visible.



Figure 6.7: The cold source at 3 MW with polyethylen strips in the beam, with the geometric center marked by the upper corner of the horizontal strip.

Visualization of the filling level of the cold source

During a first reactor startup, reactor power was halted at several power levels between 300 kW and 5 MW. Pinholes with 1, 2, and 7 mm diameter were tested. Best results were obtained with the 2 mm pin hole at 3 MW reactor power. The very small pinhole required exposure times between 10 and 30 minutes.

Since the pinhole camera shows an inverted image, the cold source is shown upside down with the liquid level from top to bottom. The liquid is seen as darker (less intensity) because neutrons emitted from the liquid D_2 are moderated to lower average wavelength. On the way to the detector, the neutrons have to pass several walls and windows: The ZircAlloy wall of the cold source, the Aluminium beam tube nozzle and the vacuum windows of the beam tubes. The absorption and scattering cross sections increase with increasing wavelength, causing higher attenuation for cold neutrons than for thermal neutrons.

Fig. 6.5 shows the upside-down image of the liquid level in the cold source at 3 MW reactor power, Fig. 6.6 shows the same field of view at 5 MW, with the visible liquid level gone as the cold source boils at this power.

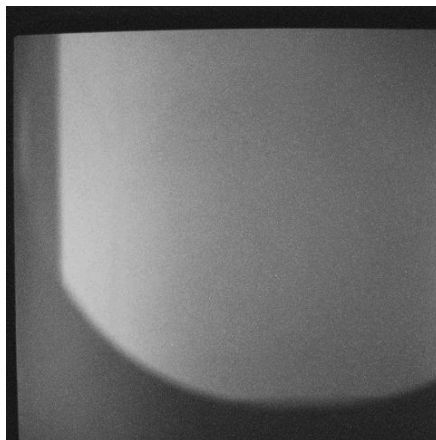


Figure 6.6: At 5 MW, the visible level is gone.

Measurement of the filling level of the cold source

At a following reactor startup, the experiment was repeated for attempted quantitative measurement. For gauging the image scale, and marking the beam center, two strips of borated polyethylen of known width were fastened at the beam exit. The horizontal strip was tilted to make the image asymmetric so there would be no doubt about the correct orientation of the image. Fig. 6.7 shows the image of the cold source with the polyethylen strips in the beam, Fig. 6.8 has the dimensions inserted.

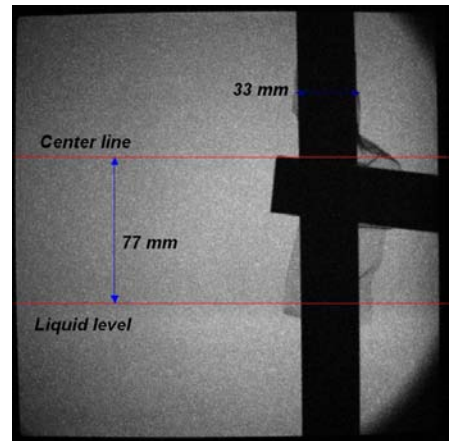


Figure 6.8: Gauging of scale and projection ratio from measured distances.

With the strip width of 33 mm, the scale of the image was determined. The liquid level was thus measured at 77 mm distance from the center line (Fig. 6.8). With the known distances between the cold source and the pinhole and the pinhole and the detector, the projection ratio was calculated. The 77 mm distance at the detector correspond to 28 mm at the cold source. From the CAD model of the cold source, the filling volume of the cold source at the center line of the beam was determined as 10636 cubic centimeters or roughly 10.6 liters, with one centimeter height difference corresponding to 704 cubic centimeters. The determined filling level

was then calculated as 12626 cubic centimeters, or roughly 12.6 liters.

Only after these calculations, we asked the operators for the cold source for their estimate of the actual filling. They assumed that the best filling they obtained was 12.5 liters.

Conclusions

The surprising apparent accuracy of this measurement in spite of so many inaccuracies involved may be pure coincidence and luck. At the time of writing, there had been no opportunity yet

to repeat the measurement on a consecutive reactor startup. The results will be verified by a new experiment as soon as possible.

6.2 Implementation of the new multi filter at ANTARES

Klaus Lorenz¹, Elbio Calzada², Martin Mühlbauer², Michael Schulz², Burkhard Schillinger², Karl Zeitelhack²

¹Physics Department E21, TU München

²ZWE FRM II, TU München

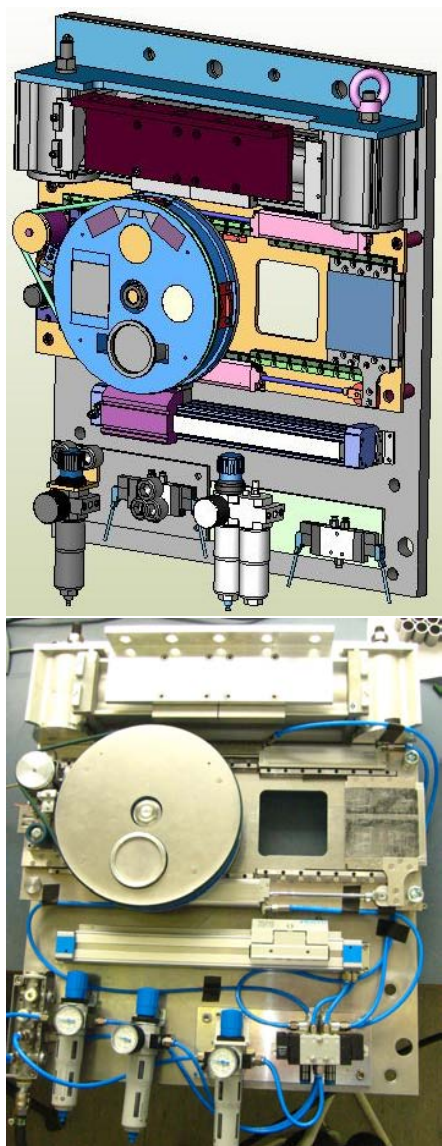


Figure 6.9: The new multi-filter (schematic (top) and photograph (bottom)).

Design efforts

A new multi-filter is ready for application at the ANTARES facility at FRM II. Between fast shutter and aperture wheel [1] a very compact filter package was installed (fig. 6.9) allowing the quick and precise positioning of four different crystal filters in the neutron beam. Due to the limited space at this position, the maximum thickness for the filters was 50mm, which is the thickness of all but the beryllium filter (only two 20mm thick beryllium plates were available, which were combined to a 40mm filter). The effect of the different filters on the neutron spectrum was investigated with TOF measurements (fig. 6.10). The cause for the offset in the raw TOF data are epithermal and also a fraction of the thermal neutrons, that penetrate the Gd coating of the chopper wheel. Sapphire single crystals are well known as good filters for epithermal neutrons [2, 3] and the TOF measurement confirms that the installed filter efficiently blocks epithermal neutrons without remarkable modifications of the spectrum in the thermal and cold range. This is e. g. very useful for phase contrast imaging with a LiF-scintillator [1, 4], where epithermal neutrons are a major cause for noise. Another reason for background noise is X-ray and gamma radiation. Because of its high atomic number and transparency for cold and thermal neutrons, bismuth is a very good gamma filter.

Beside the single crystal gamma filter a polycrystalline bismuth filter was installed to investigate the utilization of

certain bragg edges in neutron imaging. Finally a beryllium filter was installed to suppress thermal neutrons below 3.96\AA [5]. This modification of the spectrum is on the one hand useful for measurements, where only cold neutrons contribute to the measured signal (e. g. phase contrast imaging with gratings), on the other hand it can be used in a primitive way for energy selective radiography (fig. 6.11).

Applications

In fig. 6.11 neutron radiographies of step wedges of different materials are shown. The upper was done without a filter, the one below with the beryllium filter and the lowest picture displays the result of the division of the upper two. In the radiography without a filter the attenuation of the neutron beam by iron is only slightly higher than of the lead. With the beryllium filter this changes and the lead attenuates the beam stronger than the iron. The contrast is still not high, but if the radiography without filter is divided by the radiography with beryllium filter, the contrast becomes clearly visible. This method is an easy way to increase the contrast for certain materials in neutron radiographies.

- [1] Lehmann, E., Lorenz, K., Steichele, E., Vontobel, P. *Nucl. Instr. and Meth. in Phys. Res. A*, 542, (2005), 95–99.
- [2] Born, R., Hohlwein, D., Schneider, J. R., Kakurai, K. *Nucl. Instr. and Meth. in Phys. Res. A*, 262, (1987),

359–365.

[3] Stamatelatos, I. E., Messoloras, S. *Rev. Sci. Instr.*, 71, (2000), 70–73.

[4] Cowley, J. M. In *Diffraction Physics* (Elsevier, Amsterdam, Netherlands, 1995), 3 edition.

[5] Webb, F.J. *Nucl. Instr. and Meth.*, 69, (1969), 325–329.

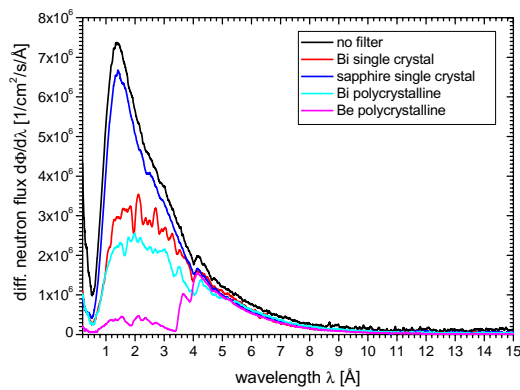
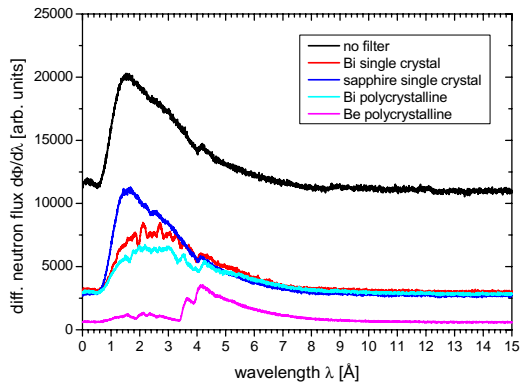


Figure 6.10: TOF measurements of the neutron spectrum at ANTARES with the different crystal filters (top: raw data, bottom: corrected).

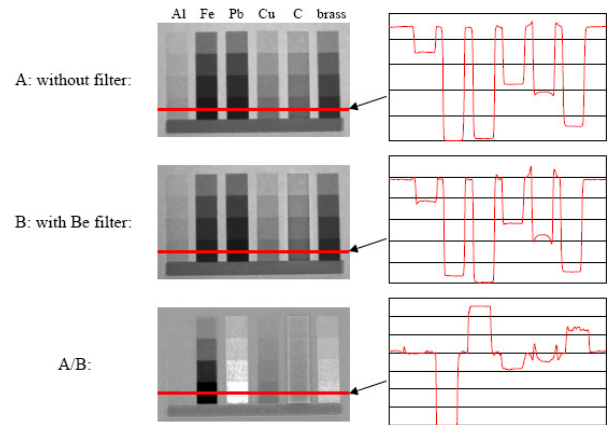


Figure 6.11: Method to increase the contrast for certain materials in neutron radiographies with a beryllium filter.

6.3 Neutron phase contrast tomography

Klaus Lorenz¹, Burkhard Schillinger²

¹Physics Department E21, TU München

²ZWE FRM II, TU München

Experimental setup

In neutron phase contrast imaging the variation δ of the real part of the refractive index $n = 1 - \delta + i\beta$ from unity is used to get an additional contrast besides absorption contrast. The easiest way to get this phase contrast is to use

a propagation based method. Unlike interferometric measurement methods, no complicated experimental setup is necessary. Basically the same setup as for conventional neutron radiography can be used with two additional requirements: The neutron beam must have a high transversal spatial coher-

ence at the sample position and the detector must have a certain distance from the sample [1]. The high coherence is achieved by the introduction of pinhole apertures with a diameter of 2mm and less in the beam in a distance of 14m to the sample position (see fig. 6.12). Due to the

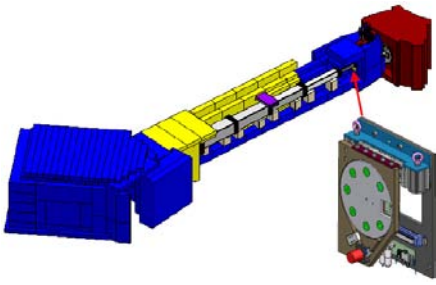


Figure 6.12: Implementation of the pinhole apertures at ANTARES.

drastically reduced neutron flux, exposure times in phase contrast measurements are much longer than in conventional neutron radiography, what makes this method much more sensitive to background noise.

Main causes for noise are epithermal neutrons and gamma radiation in the beam, secondary radiation due to activation and inherent noise of the detector system. Until recently, the noise level in long time exposure radiographies with a CCD detector system was much too high for phase contrast imaging. Good results were only achieved with image plate detectors [2], which have the big disadvantage of not allowing normalization and tomographies. After some modifications of the pinhole apertures, the improvement of the shieldings in the sample and detector area and the installation of the new multi filter (see corresponding report), the signal-to-noise-ratio in long time exposure measurements with the CCD detector improved significantly and allowed the step from phase contrast radiography to phase contrast tomography.

Applications

In figure 6.13 the results of a conventional tomography are compared with those using the phase contrast effect. The effect is only used in a qualitative way for contrast enhancement at edges and interfaces, the phase shift is not measured directly (no phase retrieval).

The test sample is a step wedge out of $\text{AlMg}_{4.5}\text{Mn}$ with another aluminum alloy (AlSi_9Cu_4) cast around it (see fig. 6.14). Both alloys have very similar at-

tenuation coefficients. Because of this and the fact, that the sample has a constant thickness in beam direction, there is no contrast between the different steps in conventional neutron imaging. Under phase contrast conditions, due to the fact that Manganese causes a negative and Copper a strong positive phase shift, phase contrast occurs at the inner interfaces which are parallel to the direction of the neutron beam.

- [1] Cowley, J. M. In *Diffraction Physics* (Elsevier, Amsterdam, Netherlands, **1995**), 3 edition.
- [2] Lehmann, E., Lorenz, K., Steichele, E., Vontobel, P. *Nucl. Instr. and Meth. in Phys. Res. A*, 542, (2005), 95–99.

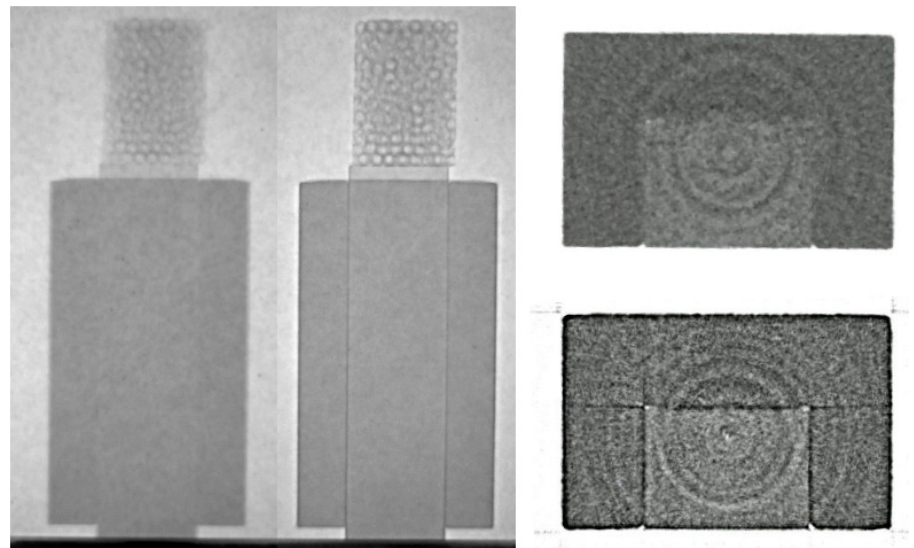


Figure 6.13: Comparison of conventional and phase contrast radiography (left) and tomography (reconstructed slice, right).

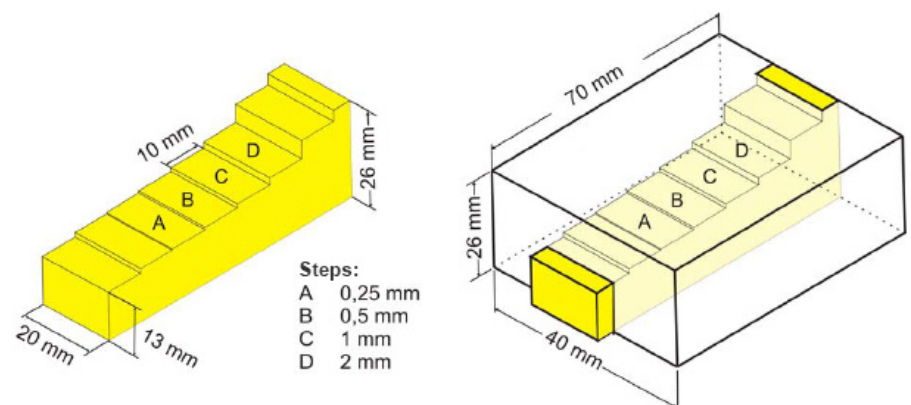


Figure 6.14: Schematic of the test sample.

6.4 NECTAR – Neutron Computer Radiography and Tomography facility

T. Bücherl¹, Ch. Lierse von Gostomski¹

¹Institut für Radiochemie, TU München

General

The NECTAR facility is designed for radiography and tomography using fission neutrons. Its general layout and first results have already been published [1, 2, 3]. In this report improvements and measurement results achieved during the last months of 2006 are presented.

Improvements

In 2006 a significant improvement of the image quality was achieved by replacing the liquid nitrogen cooled CCD-camera (512 x 512 pixels) by a new CCD-camera with 1024 x 1024 pixels (ANDOR DV424-BV). With its thermo-electrical cooling system the detection efficiency now remains constant during a complete measurement cycle, being an essential requirement for tomographic measurements which take several hours.

The control software was modified, now integrating the control of the object manipulator and the detector system within one program, i.e. improving its usability.

Results and discussion

In a number of radiographic measurements possible fields of application were investigated. In principle these measurements can be subdivided in the categories

- standards,
- technical objects and
- wooden objects.

Examples of each category are given below.

During all measurements a large number of scattered gamma rays and neutrons directly hit the CCD chip causing randomly distributed signals (sparks, glitches) in individual pixels. Thus, for each radiograph a set of typically five frames in total was measured. The measuring time per frame was 60 s.

These five frames were filtered applying a median filter and then summed up. By dark image subtraction and normalization with the open beam image the resulting radiograph of the object was calculated.

Standards

Step wedges are often used to investigate the penetration, scattering and contrast characteristics of materials. The results for step wedges made of lead, iron, aluminum and polyethylene having a maximum thickness of 50 mm were already presented [4]. The high penetration power of fission neutrons for polyethylene (as an example of a

material having a high content of hydrogen) was investigated in a further experiment using ten plates made of plexiglas of 10 mm thickness each, i.e. having a maximum thickness of 100 mm to be penetrated (figure 6.15 left). In the normalized radiograph (figure 6.15 right) all 10 steps can be separated clearly, thus proofing that fission neutrons are an extremely valuable tool for inspection thick materials having a high hydrogen content, like oils, water etc.

The contrast properties were investigated in more detail by means of a special test object. In a plexiglas block of 30 mm thickness five (hollow) cylinders, partly filled with other materials, were inserted. Additionally a lead shield of

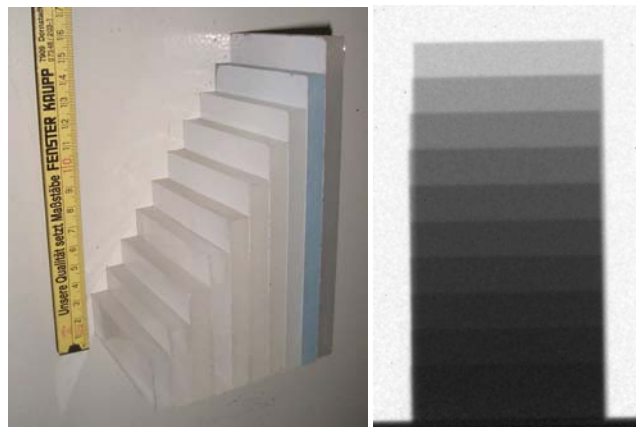


Figure 6.15: Left: Photograph of a step wedge set up of ten plates made of plexiglas of 10 mm thickness. Right: Normalized radiograph.

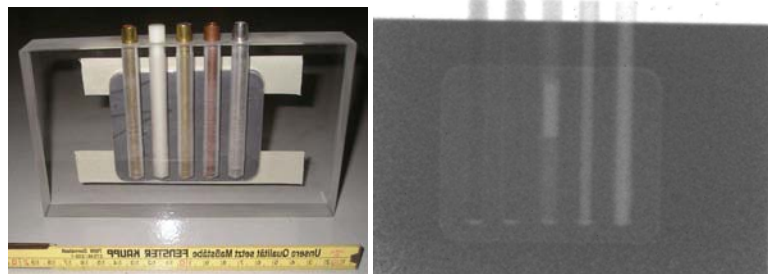


Figure 6.16: Left: Photograph of a standard set up of a plexiglas block containing (hollow) cylinders partly filled with other materials and a lead shield of 1 mm thickness that is placed in front of the block. Right: Normalized radiograph.

1 mm thickness was placed on the outer side of the block (figure 6.16 left). The corresponding normalized radiograph is shown on the right side of figure 6.16. All cylinders are clearly visible as well as the fillings of the hollow cylinders. The lead shield does not effect the contrast.

Technical objects

The non-destructive inspection of turbine blades often fails when using X-rays, gamma-rays or thermal neutrons due to low contrast and/or penetration power of these probes. Here fission neutrons can be applied as demonstrated in figure 6.17. A massive turbine

blade of about 260 mm in height was successfully radiographed for different angular positions. In figure 6.17, middle, one of these radiographs is shown. All cooling channels as well as inner cavities can be seen clearly. A tomogram for one height position of the turbine blade is shown in figure 6.17(right). As it is one of the first results of applying tomography at NECTAR, the image still shows many artefacts (e.g. ring and line artefacts). An improvement of the measurement and the reconstruction parameters will drastically enhance the image quality for the next measurements. Nevertheless, the position of the cooling channels and their dimension

can be determined from the tomogram.

Taking into account the good penetration of hydrogen containing materials as shown by the measurements of the standards, these results suggest itself the application of fission neutron radiography/tomography on dense materials containing oil distributions.

Wooden objects

Figure 6.18 shows on the left side the photograph of a timber with the approximate dimensions 150 mm x 150 mm x 500 mm. Slightly off centred a drilling of about of 40 mm diameter was realized. For the radiography mea-

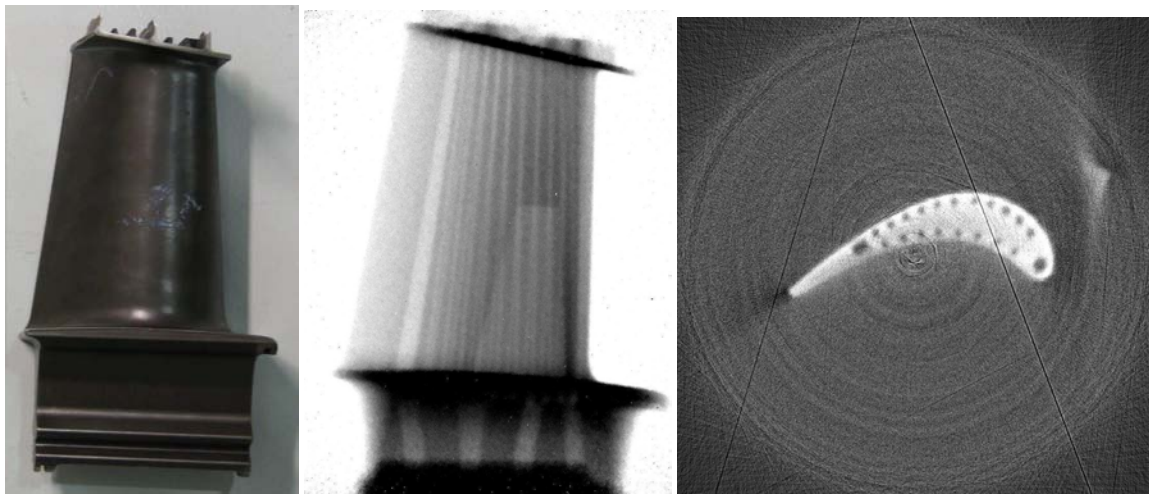


Figure 6.17: Left: Photograph of a turbine blade (height about 260 mm). Middle: Normalized radiograph. Right: A two-dimensional tomogram of the turbine blade.

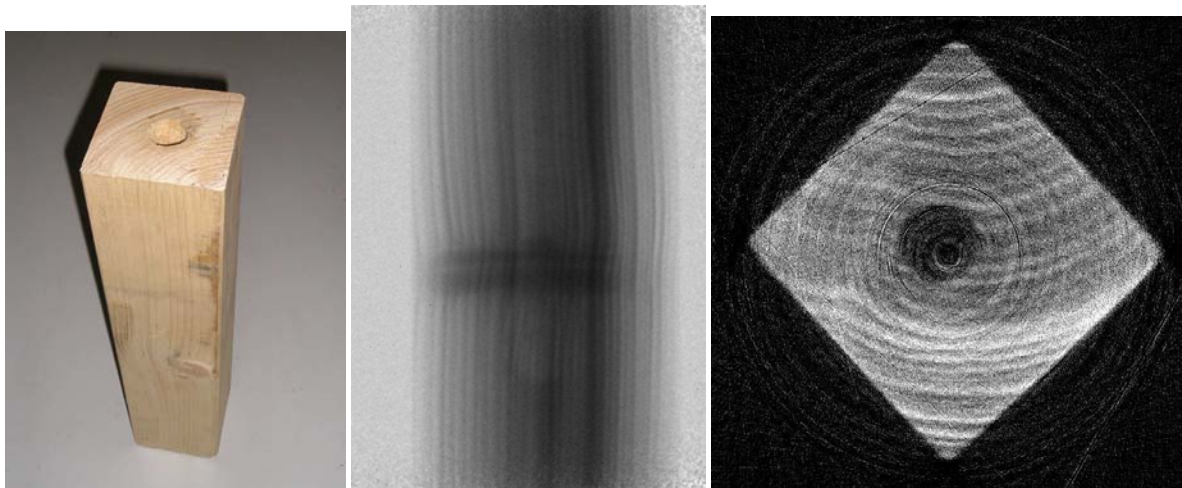


Figure 6.18: Left: Photograph of a timber (150 mm x 150 mm x 1000 mm). Middle: Normalized radiograph of a part of the timber. Right: Two-dimensional tomogram of the timber.

surement the timber was placed with its edge facing the incoming fission neutrons. The normalized radiograph (figure 6.18, middle) shows the section of the timber containing the knob. The knob and the annual rings are clearly visible. The drilling is visible, too, when changing the gray scale of the image. A tomograph of a section above the knob is shown in Figure 6.18(right). Although the annual rings and the drilling are clearly visible, the image quality of the tomograms will be further optimized for the next measurement period begin of 2007.

Outlook

The results achieved at the NECTAR facility during the last months of 2006 demonstrated its great potential for non-destructive inspection of many types of objects, but also detected areas for improvement. Especially image processing for tomography needs some further developments, which will be finalized at the beginning of 2007, enabling high quality three-dimensional tomography.

Several new areas of application will be investigated in more details. For example, first investigations on the sensitivity of fission neutron radiography

on the time dependent distribution of water in (thick) wooden objects showed promising results.

- [1] Bücherl, T., Kutlar, E., *et al.* *Applied Radiation and Isotopes*, 61, (2004), 537–540.
- [2] Bücherl, T., Lierse v. Gostomski, C., *et al.* *Proceedings of the Seventh World Conference, Rome, Italy, September 15-21*, 401–410.
- [3] Bücherl, T., Lierse v. Gostomski, C. *International Workshop on Fast Neutron Detectors and Applications Proceedings of Science*, (2006).
- [4] *Annual Report FRM II 2005*, 44.

7 Nuclear and particle physics

7.1 The positron beam facility NEPOMUC and instrumentation for positron physics

Christoph Hugenschmidt¹, Thomas Brunner², Günther Dollinger³, Stefan Legl², Benjamin Löwe², Jakob Mayer², Philip Pikart², Christian Piochacz¹, Reinhard Repper¹, Martin Stadlbauer¹, Klaus Schreckenbach²

¹ZWE FRM II, TU München

²Physik Department E21, TU München

³Institut LRT2, UniBw München

The low-energy positron beam of high intensity at NEPOMUC

In 2006 various experiments were performed at the high intensity positron beam facility at NEPOMUC –NEutron induced POsitrone source MUniCh– in order to improve the beam characteristics such as intensity, available energy range and beam brilliance. The maximum positron yield is up to $5 \cdot 10^8$ moderated positrons per second at a kinetic energy of 1 keV. At present, the lowest available beam energy is 15 eV with an intensity of $4 \cdot 10^7$ positrons per second. The maximum beam energy is limited to the high voltage, that can be applied at the platinum foils of the in-pile source components and amounts to about 3 kV. A survey of the beam performance and positron beam experiments can be found in [1, 2].

A decrease of the positron intensity was observed within about 20 h which is attributed to surface contaminations adsorbed at the platinum moderation foils. The regeneration of these foils is achieved by exposure to a small amount of oxygen ($\approx 10^{-1}$ mbar) for a few minutes.

In the longitudinal magnetic guide field of 7 mT the diameter of the positron beam amounts typically to 15–20 mm. Several efforts have been made to develop devices for beam enhancement, since a more brilliant beam (lower divergence and reduced beam diameter of about 2 mm) is desirable for a variety of experiments. For this

reason an additional remoderation unit based on a tungsten single crystal in reflection geometry was tested at NEPOMUC (section 7.2). Another approach is presently developed, which benefits from inelastic positron scattering in a gas-filled drift-chamber, in order to improve the beam brilliance.

Experiments at NEPOMUC

Fig. 7.1 shows experiments connected to the positron beam facility NEPOMUC.

The coincident Doppler-broadening

spectrometer (CDBS) is routinely operated with a primary beam energy of 1 keV. The beam is focused to about 1 mm and can be accelerated to 31 keV onto the sample in order to allow spatially resolved defect studies. Various experiments have been performed in order to investigate the chemical surrounding at open-volume defects of ion-irradiated metal samples (section 9.2) or defects in metals after mechanical load.

Great efforts have been made in order to reduce the γ -induced electron background for studies with positron anni-



Figure 7.1: The positron beam facility NEPOMUC and positron spectrometers in the experimental hall of FRM II: CDB spectrometer (TUM), PAES-facility (TUM, not shown), apparatus for Ps^- -production (MPI nuclear physics, Heidelberg), and components of the pulsed-beam facility PLEPS (UniBw, Munich).

hilation induced Auger-electron spectroscopy (PAES). With new parameter settings of the electrostatic beam guidance at the entrance of the analysis chamber PAES-spectra were recorded within only 3 h acquisition time. Low-energy positrons (15 eV) were focused onto Au-covered surfaces of single crystalline silicon and poly-crystalline copper in order to study sample surfaces with highest sensitivity (section 9.3).

Two additional experimental setups were installed at the multi-purpose beam port:

An apparatus for the production of the negatively charged positronium

(Ps^-) was developed at the Max-Planck-Institute for nuclear physics and connected to the open beam port of the positron beam line. This year first measurements were performed in order to improve the energy dependent production rate of Ps^- and the signal-to-noise ratio. It was shown that the production rate is at least a factor of 25 higher than in previously performed lab experiments which would allow experiments for QED-tests.

The angular correlation and the Doppler-shift of the annihilation photons were detected in coincidence with a second experimental device at the

open beam port of NEPOMUC. For this reason two segmented high-resolution germanium detectors were installed in collaboration with E12 of the physics department. At present the data analysis is in progress in order to reconstruct the electron momenta in three dimensions for each annihilation event.

- [1] Hugenschmidt, C., Schreckenbach, K., Stadlbauer, M., Straßer, B. *Nucl. Instr. Meth. A*, 554, (2005), 384–391.
- [2] Hugenschmidt, C., Stadlbauer, M., Straßer, B., Schreckenbach, K. *Appl. Surf. Sci.*, 252, (2006), 3098–3105.

7.2 Positron remoderation facility for the slow positron beam at FRM II

Christian Piochacz², Christoph Hugenschmidt², Gottfried Kögel³, Klaus Schreckenbach¹, Günther Dollinger³

¹Physics Department E21, TU München

²ZWE FRM II, TU München

³Institut LRT2, UniBw München

In order to enhance the brightness of the positron beam produced by the NEPOMUC source, a positron remoderator was developed. It has been installed at the first accessible point of the beam facility and first measurements have been done in order to obtain the efficiency of the setup and the quality of the remoderated beam. The idea of using remoderation for brightness enhancement was first described by [1] and has been realized in several table top setups [2][3]. The remoderation unit described here was designed according to the ideas of the remoderator utilized in [3] but with improvements to accept a beam with a greater phase space volume.

For the remoderation process, positrons are focused on a solid, where they stop and thermalize. There is a certain possibility that the thermalized positrons diffuse back to the surface where they can leave the solid with a sharp energy and a small angular divergence. The whole process depends on the properties of the solid, which is used for moderation. Materials, such as tungsten, nickel and platinum are known to be efficient positron mod-

erators. There are basically two possibilities for remoderating a positron beam, depending on which surface the positrons are emitted: the reflection or the transmission geometry. The presented remoderation device works in reflection geometry with a W(100) single crystal. The moderated positrons leave the crystal surface with an energy of about (3 ± 0.03) eV and an angular spread of about 0.1 eV.

Experimental setup

The remoderation setup is shown in Fig. 7.2. The positrons from the NEPOMUC source are guided by magnetic solenoid fields to the entrance of the device. At the last 60 cm in front of the setup a magnetic field gradient can be varied in order to adjust the ratio of longitudinal and transversal momentum of the beam. The longitudinal magnetic guiding field is terminated by a novel field termination, in order to avoid a complicated and unwished superposition with the electric and magnetic fields inside the remoderator. The field termination is build up of 30 $10 \mu\text{m}$ thick and in the center 2 mm broad metglass stripes. This solution has the advantage of a high transparency even for a beam with

a great diameter up to 60 mm and ensures nevertheless an abrupt termination of the magnetic field. After passing this device the positrons fly without a guiding field till they enter the field of the magnetic lens and get focused on the tungsten crystal. The remoderated positrons can pass the field of the magnetic lens adiabatically because of their low energy and are formed electrostatically to a beam. This beam is bent to the outlet by a perpendicular magnetic dipole field which is located at the beam separator. The electrodes and the dipole have nearly no effect on the primary beam due to its much higher energy in the range between 0.5 and 2 keV. On the outlet two variable apertures permit an adjustment of the remoderated beam onto the center of the axis and allow the determination of the beam diameter. After the remoderation unit the positrons are guided by magnetic solenoidal fields to the different experiments installed at the NEPOMUC facility. Additional electric lenses are installed at the outlet to ensure an optimal injection of the remoderated beam into the magnetic field. The hole setup is magnetically shielded by a mu-metal housing because the slow

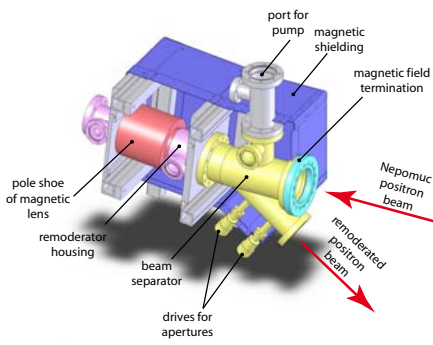


Figure 7.2: Schematic view of the positron remoderator. The magnetic dipole and magnetic correction coils are not shown.

positrons are very sensitive on magnetic disturbances.

Results

In order to measure the remoderation efficiency two equivalent and remov-

able annihilating targets in front of the remoderator and behind the outlet of the remoderator were connected. The quality of the primary and the remoderated beam could be evaluated due to pictures taken by two systems consisting of a MCP, phosphor screen and CCD camera.

We succeeded to produce very well formed remoderated positron beams at several energies of the primary beam (see fig. 7.3). At an energy of 1.5 keV a remoderating efficiency of nearly 2% was attained and the beam diameter of the remoderated beam was about 2 mm (FWHM). This beam could be guided to the open beam port of the NEPOMUC facility and to the PAES experiment for further measurements. The shape of the beam could be conserved perfectly due to the small diameter and the small energy spread of the remoderated beam.

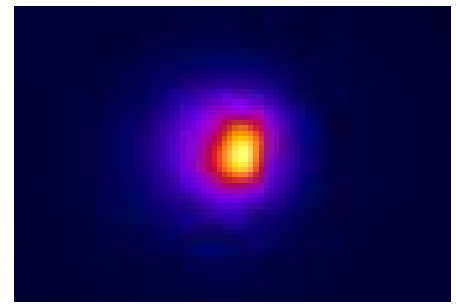


Figure 7.3: The picture of the profile of the remoderated positron beam taken with a system of MCP, phosphor screen and CCD camera. The beam has a diameter of 2 mm (FWHM).

- [1] A. P. Mills, J. *Appl. Phys.*, 23, (1980), 189.
- [2] Frieze, W., Gidley, D. W., Lynn, K. *Phys. Rev. B*, 31(9), (1985), 5628.
- [3] Kögel, G., SPM-Group. *Appl. Surf. Sci.*, 116, (1997), 108–113.

7.3 Physics at the cold neutron beam facility MEPHISTO

H. Angerer^{1,5}, F. Ayala Guardia^{3,5}, S. Baeßler^{3,5}, M. Borg^{3,5}, L. Cabrera Brito^{3,5}, K. Eberhardt^{3,5}, B. Franke^{1,6}, F. Glück^{3,5}, W. Heil^{3,5}, I. Konorov^{1,5}, G. Konrad^{3,5}, N. Luquero Llopis^{3,5}, R. Muñoz Horta^{3,5}, M. Orlowski^{3,5}, C. Palmer^{3,5}, G. Petzoldt^{1,5}, D. Rich^{4,5}, P. Schmidt-Wellenburg^{2,6}, M. Simon^{1,5}, Y. Sobolev^{3,5}, H.-F. Wirth^{1,5,6}, O. Zimmer^{1,5,6}

¹TU München, Physik-Department, E 18

²Institute Laue-Langevin, Grenoble

³Universität Mainz, Institut für Physik

⁴TU München, ZWE FRM II

⁵aSPECT collaboration

⁶Helimephisto group

During 2006, three different experiments were performed successfully at the MEPHISTO beamline: **aSPECT**, **cubeD2**, and **Helimephisto**. An introduction to the **cubeD2** experiment and its results is given elsewhere in this annual report. The other two experiments will be specified below. Furthermore, many efforts went into moving our facility from NL3a to NL1 within the neutron guide hall in the middle of 2006. The properties of both beam line positions are described in the following section.

Movement from NL3a to NL1

The neutron beam at NL3a had a cross sectional area of 116×50 mm (height \times width). It offered a cold spectrum with a thermal equivalent flux of $2 \times 10^{10} \text{ cm}^{-2}\text{s}^{-1}$, measured by gold foil activation [1]. The beam shutter was placed inside the casemate. **aSPECT** and **cubeD2** were performed at NL3a.

At its new position MEPHISTO is placed downstream of N-REX⁺. The monochromator of N-REX⁺ is placed inside a concrete bunker, which now contains 4 m of additional neutron guide and a shutter for MEPHISTO. The neutron guide cross section of NL1 is ta-

pered down from $120 \times 62 \text{ mm}^2$ to $100 \times 62 \text{ mm}^2$. The new exit of NL1 is situated at the end of the N-REX⁺ bunker. The center of the beam is 118 cm above the ground level of the neutron guide hall. An additional beam attenuator can decrease the beam intensity down to 60, 20, 4, and 2%, using borated aluminum plates with different apertures. The attenuator plates are situated in the shutter box. The spectrum of NL1 was characterized by K. Zeitelhack et al. in 2004; its intensity maximum is at 4.5 \AA [1]. MEPHISTO also provides a beam stop which was already used at NL3a.

aSPECT

An accurate measurement of the neutrino/electron angular correlation coefficient a in free neutron decay is important in order to determine precisely the element V_{ud} of the CKM quark-mixing matrix. A unitarity test of this matrix challenges the Standard Model of particle physics. *aSPECT* provides a precision measurement of the proton spectrum in free neutron decay. For kinematic reasons its shape depends on the angular correlation between the momenta of the electron-antineutrino and the electron [2, 3].

The setup of *aSPECT* is shown in Fig. 7.4 at top. The neutron beam (green arrow) is guided through the spectrometer. Some neutrons decay in the decay volume, and the decay protons are guided by a magnetic field to the proton detector. At the analyzing plane, an electrostatic potential barrier is applied. Therefore, only protons with sufficient energy can overcome the barrier and be detected. By varying the barrier potential from 0 to 750 eV one can measure the integrated proton spectrum of free neutron decay. At bottom, measured pulseheight spectra are shown for different applied barrier voltages U at the analyzing plane. At about channel 80, the protons are visible. The proton count rate decreases when increasing the analyzing plane voltage. Since the endpoint of the proton spectrum is at about 750 eV, by setting the analyzing plane to 780 V no events are detected, apart from background from decay electrons and gamma radiation. The events below channel 55 are due to electronic noise of the detector. From the dependence of the total proton count rate on the barrier voltage we will extract the correlation coefficient a .

Helimephisto – a superthermal source of ultracold neutrons

Helimephisto is a prototype of a superthermal source for ultracold neutrons (UCN). Inside the converter vessel made from stainless steel filled with

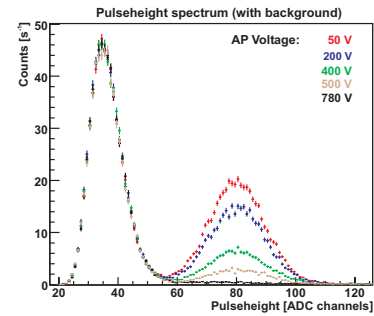
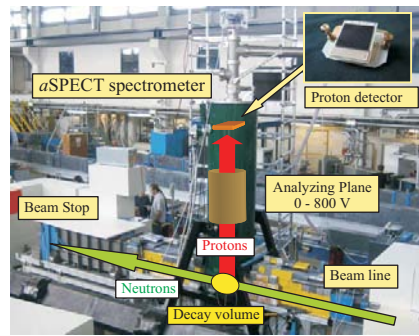


Figure 7.4: Left: Setup of *aSPECT* at NL3a. Right: Pulseheight spectra for different applied barrier voltages U at the analyzing plane (AP).

superfluid ^4He at temperatures below 1.3 K incoming cold neutrons are down-scattered to UCN energies (below approx. 170 neV). The main UCN production process is single phonon excitation by neutrons with wavelength 9 \AA [4, 5]. The UCN are then extracted via evacuated stainless steel guides for detection. The helium is liquefied within the setup itself, thus being independent of supply with cryogenic liquids. The cooling power is provided by a commercially available Gifford McMahon cold head with 1.5 W at 4.2 K and also by two Joule-Thomson evaporation stages (^4He , ^3He) (for further information on the cold head type and the liquefaction process see Ref. [6]). To produce UCN with our source, we performed measurements in two different ways: In a storage type experiment we irradiated the converter with cold neutrons for a denominated time period in order to build up a UCN density in the helium. Then we closed the beam shutter and simultaneously opened the UCN outlet-valve. UCN time histograms obtained for different irradiation times are shown in Fig. 8.4. Integrated count rates up to 1450 counts were achieved (with the beam attenuated to 20 %). The second way was to irradiate the converter while the UCN outlet-valve was open, such that the produced UCN could continuously leave the converter vessel to the detector. Count rates up to 190 s^{-1} were obtained.

Note that the goal of the experiment was not to obtain maximum UCN output but to investigate the properties of the source and, in particular, to demonstrate for the first time efficient extraction of stored UCN from a superfluid helium converter. The beam was strongly collimated in order to avoid activation by scattered neutrons. A UCN production rate of $0.7 \text{ cm}^{-3} \text{ s}^{-1}$ was measured for a cold flux of $1.5 \times 10^9 \text{ cm}^{-2} \text{ s}^{-1}$, close to theoretical expectation. The results show that there is no principle obstacle to build an ex-pile UCN source using a cold neutron beam, which may provide UCN densities of several 1000 cm^{-3} .

- [1] Zeitelhack, K., *et al. Nuclear Instruments and Methods in Physics Research A*, 560, (2006), 444.
- [2] Glück, F., *et al. Europhys. Journ. A*, 23, (2005), 135.
- [3] Zimmer, O., *et al. Nucl. Instrum. Meth. A*, 440, (2000), 548.
- [4] Schott, W., *et al. Europhys. Journ. A*, 16, (2003), 559.
- [5] Golub, R., Pendlebury, J. M. *Phys. Lett. A*, 62, (1977), 337.
- [6] Schmidt-Wellenburg, P., Zimmer, O. *Cryogenics*, 46, (2006), 799.

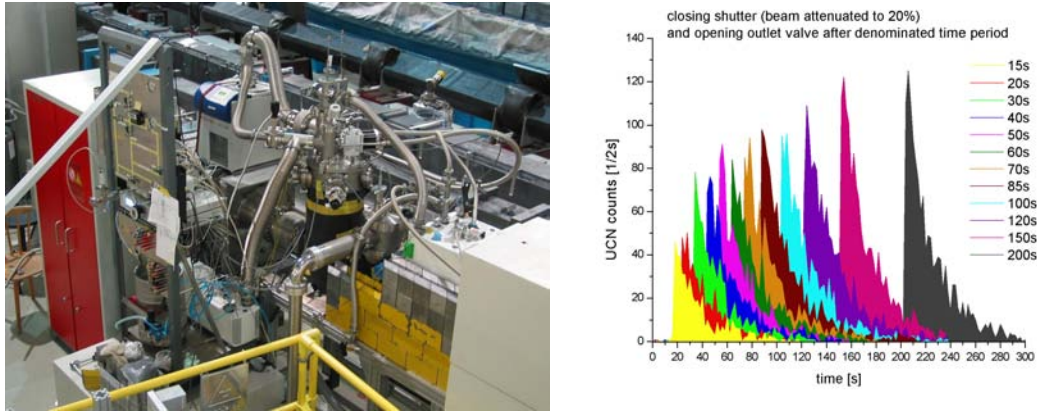


Figure 7.5: Left: Setup of Helimephisto at NLL. Right: Plots of measured UCN count rates in the storage type experiments. From the time dependence of the integral UCN numbers at 1.0 K one derives a storage time of 44(3) s of UCN in the converter vessel.

7.4 Production of ultracold neutrons at the FRM II and at the TRIGA Mainz

I. Altarev¹, P. Amos¹, A. Frei¹, E. Gutmiedl¹, F.J. Hartmann¹, A. Müller¹, S. Paul¹, H.F. Wirth¹, D. Tortorella¹, D. Rich⁴, K. Eberhardt², G. Hampel², J.V. Kratz², T. Lauer³, N. Wiehl², W. Heil³, Y. Sobolev³, Y. Pokotilovski⁶, R. Hackl⁵, L. Tassini⁵

¹Physik Department E18, TU München

²Inst. f. Kernchemie, Universität Mainz

³Inst. f. Physik, Universität Mainz

⁴ZWE FRM II, TU München

⁵WMI Garching

⁶Joint Institute for Nuclear Research, Dubna, Russia

Introduction

During the last year two basic experiments with solid deuterium (sD_2) as converter material for production of ultracold neutrons (UCN) have been performed at the FRM II and the TRIGA reactor in Mainz. The goal of these experiments was to study the main important parameters for an optimized strong sD_2 source for UCN at the FRM II [1]. These parameters are:

1. The way of freezing out the sD_2 ,
2. The optimum temperature of the sD_2 ,
3. The lifetime of the UCN within the sD_2 ,
4. Dependence of the UCN production on the cold neutron temperature,
5. Optical structure of frozen sD_2 ,
6. Comparison of measured and calculated UCN production rates

Both experiments delivered complementary information on the above mentioned parameters. For example in the TRIGA experiment only solid deuterium frozen from the gas phase at low temperature (6K), was studied. In the cubeD2 experiment the solid deuterium was mainly produced from liquid deuterium.

Experimental setup at the FRM II - cubeD2

At FRM II an experimental setup cubeD2 was installed at the MEPHISTO cold neutron beam line. The setup is composed of two main sections, the cooling stage and the gas handling system. Auxiliary parts are the para-ortho deuterium converter and the remote control system. The main component of cubeD2 is the converter cell. Deuterium is frozen in a cubic chamber

of aluminum (46 mm outer side length). Two sapphire windows ($d=12$ mm) are mounted at the side walls to allow optical inspection. The bottom of the cell is in contact with a two-stage cold head. The entrance window for the cold neutrons (thickness 0.5 mm) on the front side is machined directly from an aluminum block. The produced UCN leave the target through the rear-side window, a glued 100 μm thick aluminum foil. Two diode sensors monitor the temperature of the cell. Temperatures down to 6 K at the surface are easily reachable. A heating resistor (20 Ohm), together with a temperature controller, allows to vary the temperature over a wide range [5 - 300 K].

In Figure 7.7 a picture of solid frozen deuterium is shown. The cell was half filled with liquid deuterium and afterwards slowly frozen out below 18.7 K. The crystal was of good quality and very transparent.

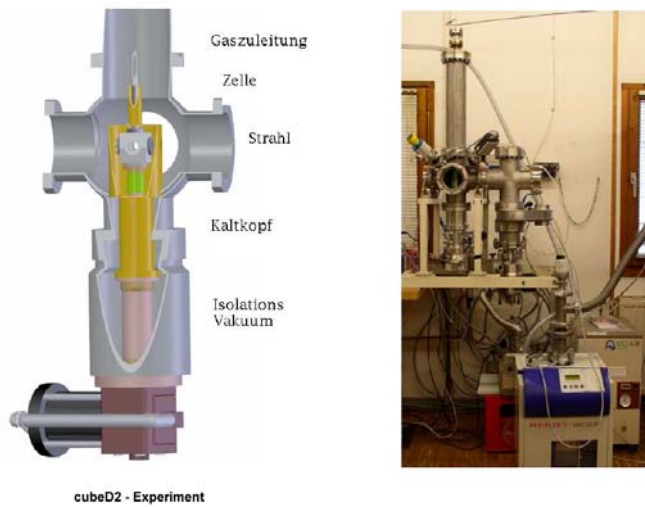


Figure 7.6: cubeD2 setup

Measurements with the cubeD2 setup

Figure 7.9 shows the measured UCN count rates for two different sD_2 sample cells (0.5 cm and 3 cm sD_2 thickness). The UCN production was measured after freezing from the liquid phase (24K - 19K). The solid was produced carefully below 18.7K and cooled down slowly to 8K/10K. The UCN production within the sD_2 is roughly 50-60% higher than that with the liquid deuterium. The UCN count rates from the 0.5 cm sD_2 sample are higher than the rates of the 3 cm sample. This effect is understood, if one takes into account that the mean free path of the UCN in sD_2 is in the range of 5-8 mm (active layer). This value can be determined by analyzing the temperature dependence of the UCN production rate at fixed sD_2 thickness, exposed to the cold neutron-beam of MEPHISTO. The key point in this analysis is the determination of the loss cross section for UCN inside the sD_2 . A model for this temperature dependent loss cross section was used in a calculation of the measured UCN count rates and the free parameters where fitted. With the aid of this loss cross section it is possible to determine the average UCN life time inside sD_2 and also the UCN mean free path. If the thickness of the sD_2 is larger than the active layer, the effective cold neutron flux, which produces UCN inside the active layer, is weakened by the inactive sD_2 behind the active layer. The incoming cold neutron flux at the entrance of the sD_2 cell was measured by gold-foil activation to be $1.55 \times 10^9 \text{ cm}^{-2}\text{s}^{-1}$.

The measured UCN count rates may be confirmed with the common model for UCN production in sD_2 [2] the Debye model for one phonon down-scattering of cold neutrons and the knowledge of the loss cross section for UCN inside sD_2 . This cross section for sD_2 , frozen from the liquid phase, was determined by an other group by an UCN transmission measurement [3] and agrees quite well with our results.

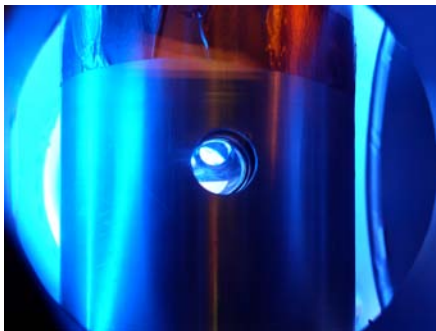


Figure 7.7: Picture of frozen solid deuterium

Experimental setup at the TRIGA reactor Mainz

A schematic view of the test facility for investigating the UCN production at the TRIGA reactor, Mainz, is shown in Figure 7.8. So far, all test measurements were performed at the tangential beam tube C where the thermal heat-load is relatively small. The very end of the in-pile part with the helium cooled converter head is positioned just in front of the graphite reflector. During the reactor pulse the thermal neutron flux amounts to $10^{15} \text{ n/cm}^2/\text{s}$. The UCN produced in the solid-D2 converter are guided outside the biological shield and finally detected. This setup is, similar to the cubeD2 setup, composed of two main sections, the liquid He cooling system and the gas handling system. Auxiliary parts are the para-ortho- deuterium converter and the remote control system. With this setup it is possible to freeze out 200 cm^3 of solid D2 (sD_2).

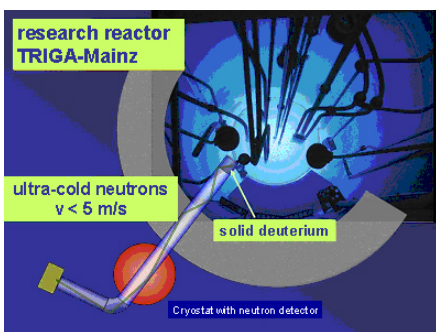


Figure 7.8: TRIGA Mainz setup

Measurements at the TRIGA Mainz setup

Figure 7.10 shows the measured UCN count rates for two different experimental setups. In one arrangement the sD_2 was exposed directly to the thermal neutron flux of the TRIGA reactor. In the second setup the sD_2 was surrounded by the frozen premoderator 1,3,5-trimethylbenzene (Mesitylene). This premoderator was kept frozen at a temperature of 21 K. Mesitylene down-scatters the thermal neutrons to the cold neutron regime. The production of UCN in sD_2 is most efficient for incoming cold neutrons with an equivalent temperature of 30K [2]. In both setups the amount of frozen deuterium was varied (0 - 200 cm³ / 0 - 9 mol). For smaller quantities of sD_2 (0 - 4 mol) the setup with the premoderator has roughly a gain of more than two, compared to the setup without a premoderator. The UCN count rate for the premoderator setup starts to saturate from 4 - 5 mol on. This behavior is not seen with the setup without premoderator. This is may be explained by the fact that sD_2 itself acts also as premoderator for thermal neutrons, but it is not as efficient as Mesitylene or other cold moderator (CD_4 or H_2). Therefore the saturation of the extracted UCN from sD_2 is compensated by adding additional sD_2 at higher quantities of sD_2 , which acts as a premoderator.

From the measurements with the premoderator it is possible to extract the average mean free path for UCN inside sD_2 . This value is about 4 - 5 cm. The mean free path of UCN, obtained from the TRIGA experiments, is a factor ten larger than the mean free path in the cubeD2 experiment. The conclusion of this is that the inelastic and elastic cross section of sD_2 for UCN in sD_2 ice, which is frozen out slowly from the gas phase, is much smaller than the sD_2 ice cross section, produced from the liquid phase. This result has to be investigated in more detail.

Outlook

The measurements on the UCN production at the FRM II and the TRIGA reactor in Mainz have demonstrated, that it is possible to use solid deuterium as a strong UCN source. The measured UCN count rates are understood and confirm the theoretical production rates of UCN inside sD_2 . The UCN losses for sD_2 crystals produced in different ways has to be further investigated, though the method of freezing from the gas phase seems the best method for producing

an efficient UCN source. Transforming the results to the situation of having this kind of UCN source exposed to the strong cold neutron flux of the FRM II inside the heavy water vessel shows that for a typical UCN experiment one can achieve a UCN density of $5 \cdot 10^{10} \text{ cm}^{-3}$.

- [1] Trinks, U., *et al.* *NIMA*, 440, (2000), 666.
- [2] Golub, R., Böning, K. *Z. Phys. B: Cond. Matt.*, 51, (1983), 95–98.
- [3] Atchison, F., *et al.* *PRL*, (2005).

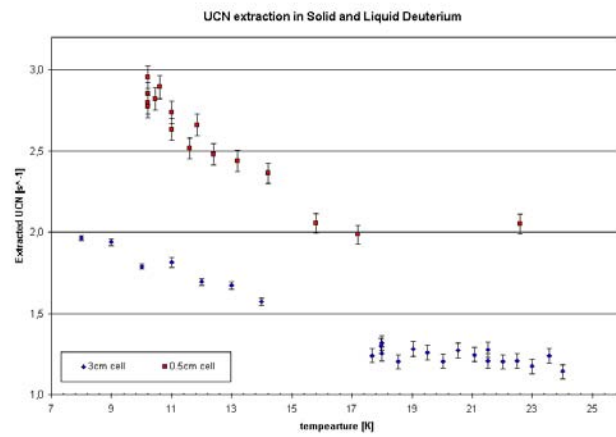


Figure 7.9: UCN count rate as function of temperature

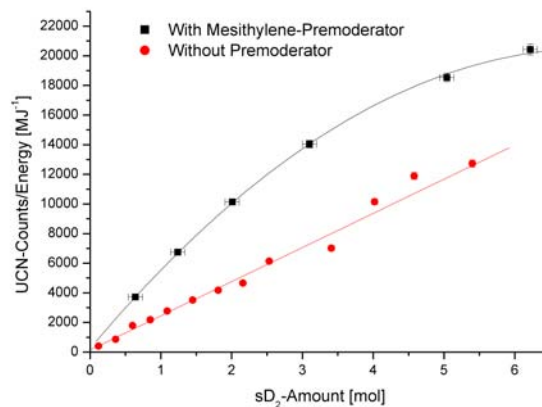


Figure 7.10: UCN count rate as a function of the amount of frozen sD_2 (with and without premoderator) normalized to the reactor power (10 MJ at full reactor power puls)

8 Industrial applications

8.1 Irradiation facilities

X. Li¹, H. Gerstenberg¹, J. Favoli¹, V. Loder¹, M. Oberndorfer¹, A. Richter¹, H. Schulz¹

¹ZWE FRM II, TU München

General

The irradiation service of the FRM II continued its routine operation successfully during the five reactor operation cycles in 2006. By means of

- the pneumatic rabbit system RPA,
- the capsule irradiation facility KBA,
- the test rig of the silicon doping facility SDA,
- the position for short term irradiations of medium volume samples (SDA1) and
- the high flux irradiation position in the central control rod (RS).

altogether 334 irradiations were carried out for different research projects and commercial purposes. Table 8.1 shows the irradiation numbers on each system. The silicon doping was the most frequently used rig and amounted to about 50% of all irradiations carried out in 2006. Some other important and interesting projects supported by our irradiation systems are described in the following text.

Irradiations for the fission track dating

Fission track dating is a radiometric dating technique based on analysis of the damage trails, or tracks, left by fission fragments in certain uranium bearing minerals and glasses. The number of tracks correlates directly with the age of the sample and the uranium content. To determine the uranium con-

tent the sample is annealed by heating and exposed to a barrage of thermal neutrons. More than 20 apatite samples from different geological institutes were irradiated in our irradiation channels in 2006. Due to the high uranium content in the geological samples, the samples were irradiated normally in the position SDA-1 with a relatively low neutron flux between 1×10^{15} and 1×10^{16} (cm^{-2}), which is achieved within few minutes. Standard neutron flux monitors (Au/Co) were usually irradiated simultaneously with the samples together and analyzed separately, in order to obtain the information about the local neutron fluxes within the sample sets, which typically consist of more than 10 single samples. Figure 8.1 shows an apatite sample with fission tracks under the microscope (Max-Planck-Institute for nuclear physics).

Production of isotopes for the nuclear medicine

In the 8th reactor cycle of the FRM II, the very high flux irradiation position in the control rod was used for the first time for the production of ¹⁸⁸W. It was the first successful radioisotope production in the FRM II with a very long irradiation time of an entire reactor cycle. The sample was loaded before the reactor was started and unloaded after the reactor was shut down, i.e. after completion of 52-days. The target sample contained tungsten en-

riched to 99.9% in ¹⁸⁶W. ¹⁸⁸W is produced via a double neutron capture reaction with thermal neutrons and decays to ¹⁸⁸Re: $^{186}W(n,\gamma) \rightarrow ^{187}W(n,\gamma) \rightarrow ^{188}W(\beta^-)(T_{1/2}=69d) \rightarrow ^{188}Re(T_{1/2}=17h)$.

The irradiation product is used in the so-called ¹⁸⁸W/¹⁸⁸Re generator for medical purposes. ¹⁸⁸Re emits beta particles ($E_{max} = 2.12$ MeV) having an ideal range for intravascular brachytherapy and certain cancer brachytherapies. The specific activity of ¹⁸⁸W in our first sample was approximately 155 mCi/g after a cooling time of 15 days. This project is a cooperation with the Institute for Radiochemistry of the TU München. Further irradiations for the production of ¹⁸⁸W are already planned in the next reactor cycles in 2007.

Another interesting radioactive isotope in the nuclear pharmacy, which is also prepared at FRM II right now, is ¹⁷⁷Lu. This radioisotope may help create the first successful radiopharmaceutical for solid tumors; it emits a low beta energy, which reduces radiation side effects and produces a tissue-penetration range appropriate for smaller tumours. As a bonus, ¹⁷⁷Lu emits gamma radiation, which allows physicians to also use it for both imag-

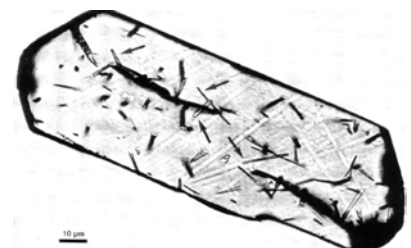


Figure 8.1: apatite sample with fission tracks under the microscope (Max-Planck-Institute for nuclear physics.)

Table 8.1: Irradiations at the FRM II in 2006

position	PRA	KBA	SDA	SDA1	RS	total
irradiation No.	62	66	173	32	1	334

ing and therapeutic purposes. In order to prepare the ^{177}Lu , Lutetium samples with enriched ^{176}Lu were irradiated on the capsule irradiation system (KBA) typically for 2 to 7 days. The Institute for Radiochemistry of the TU München is trying to develop a new and maybe a more effective way to prepare ^{177}Lu via activation of ^{176}Yb at FRM II. Several samples were already irradiated and the method of the isotope separation will be optimized. Totally about 30 samples were irradiated at FRM II for the production of ^{177}Lu .

Measurements of neutron fluxes and γ -dose

On the pneumatic rabbit system RPA, cadmium-ratio of neutron flux was measured directly by the irradiation of Cd-shielded neutron flux monitors. In order to avoid unacceptable heating of the specimens, the irradiations were performed at a low reactor power of 300kW , mostly at the beginning phase of a reactor cycle. The results are comparable to the results measured by using the standard flux monitors (Au, Co, Zr, U) in the earlier reactor cycles.

High γ -dose at the irradiation positions in reactor can be determined by using thermal luminescence detectors. For irradiation of many biological samples, the information about the γ -dose at the irradiation positions is very important. Three thermal luminescence detectors consisting of pure quartz were irradiated as test samples for short time at the RPA and the KBA. The measured data will be analyzed by the GSF - National Research Centre for Environment and Health, GmbH. Due to the influence of the high neutron dose and the heat effect on the detectors, the measurement needs to be optimised.

Silicon doping facility (SDA)

The silicon doping for a commercial production had already begun by using the prototype of the doping facility (SDA-opt) at the end of 2005. Although only this simplified system was available we entered into a business relation with 5 companies from Europe and Asia. A total of 173 batches summing up to almost 3 tons silicon ingots were irradiated in the 5 reactor cycles in 2006.

To reduce the axial inhomogeneity of the neutron flux within the ingot below 5% as required by the specification of most of clients, a special Ni-absorber is mounted on the outside of the irradiation container. Based on the values of the flux measurements, its special shape was calculated and optimised by means of Monte-Carlo calculations. According to the feed-backs of the clients, our doping quality is extremely positive. Compliance with the target resistivity and axial resistivity variation is less than 4 ~ 5%. The radial variation is below 3 ~ 4% and seems to be completely hidden in measurement noise. The lifetime of free charges is high, around 400-700 ms, what means a low content of irradiation defects. After adjustment of the calibration factors connecting the irradiation dose to the target resistivity, our doping quality can fulfill the conditions of the doping specifications for target resistivities between $20\ \Omega\text{cm}$ and $750\ \Omega\text{cm}$ very well.

Most of the irradiated ingots have diameters of 4, 5 and 6 inches. 2 batches of 8 inches ingots were irradiated as test samples for the determination of the calibration factor. Generally the starting material was predoped *n*-type Si exhibiting a resistivity of several thousand Ωcm , but also some predoped *p*-type ingots were irradiated at FRM II.



Figure 8.2: lifting unit of the doping facility mounted on the handling bridge.



Figure 8.3: new design of the coupler for the sample container.

The final silicon doping facility offering a semi automatic operation was already successfully tested in the factory and verified by the responsible surveyor TÜV Süd in summer of 2006. The lifting unit of the doping facility mounted on the handling bridge is shown in Figure 8.2. Figure 8.3 shows the new design of the coupler for the sample container.

The whole system will be completely installed at FRM II during the reactor maintenance period in January of 2007. A bunch of commissioning programs containing about 30 tests for the doping system were verified by the responsible surveyor TÜV Süd and the regulatory authority. After a successful commissioning, the new doping system will start operations in the next reactor cycle in 2007.

8.2 Fission neutron source - MEDAPP

E.M. Wagner¹, S. Kampfer¹, A. Kastenmüller¹, B. Loeper-Kabasakal¹, P. Kneschaurek²

¹ZWE FRM II, TU München

²Klinikum Rechts der Isar, München

The irradiation facility

The fast reactor neutron beam at beam tube SR10 is the successor of the Reactor Neutron Therapy beam RENT at the former research reactor FRM at Garch-

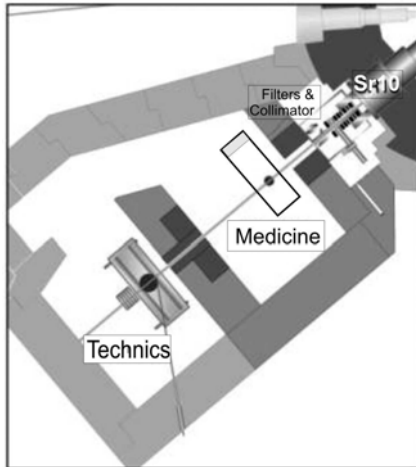


Figure 8.4: Along the fission neutron beam: the beam tube SR10, filters, collimator and the heavily shielded irradiation rooms for medical and technical use.



Figure 8.5: Medical irradiation room with treatment couch. The fixed horizontal beam enters from left, 1.45 m above the floor.

ing. The last patients out of 700 at RENT were irradiated in July 2000. The follow-up of patients is still going on and can have an impact on the choice of suitable cases at FRM II. Generally, neutron therapy is most favourably applied to slowly growing and well differentiated tumours. Most suitable sites turned out to be tumours of the head and neck, where curative treatments are possible. All shallow tumour lesions, like lymph node metastases or skin metastases from various cancer diseases, as well as chest wall metastases of breast cancer are suited for neutron irradiation, especially when pre-treated with low-LET-radiations.

The beam at SR10 has been designed for multiple use, e.g., not only for clinical neutron therapy, radiobiology, and dosimetry, but also for materials-testing, and for computerized tomography and radiography. Therefore, there are two irradiation rooms along the beam (Fig. 8.4); in the first one (Fig. 8.5) medical applications including physical and biological dosimetry are performed (MEDAPP), the second room is reserved for a permanent set-up, i.e. the neutron computed tomography and radiography facility NECTAR.

During the fission of uranium, not only fast neutrons are produced, but also hard gamma radiation. In order to establish the effect of neutrons, the gamma dose rate is decreased by a filter consisting of 3.5 cm Pb. Furthermore, a B4C-filter suppresses contaminating thermal neutrons and reduces epithermal neutrons. The beam is equipped with a multi leaf collimator (MLC). The MLC allows of the conformation of the radiation onto the contour of the tumour up to an area of 30 · 20cm².

Physical beam quality

The fast neutron flux is up to 7.108 s⁻¹cm⁻² (depending on filters and collimation); the mean neutron energy is 1.6

MeV. At 5 cm depth of a water phantom, the neutron and gamma dose rates of the medical beam with collimation 9x9 cm² are 0.33 Gy/min and 0.18 Gy/min, respectively [1, 2]. An example of depth dose curves is shown in Fig. 3 8.6. The dose distribution in the depth of a water phantom is the basis of the physical treatment planning. In order to determine the neutron and gamma components separately, two chambers are used with different sensitivities to neutrons and gammas.

With the combination of filters for therapeutic irradiations (1 cm B4C-PE and 3.5 cm Pb), the neutron-to-photon ratio decreases from about 3.6 near to the surface to 1.8 at 5 cm depth of the phantom. The half-maximum dose rate of the neutrons is at about 54 mm depth in water. The depth dose measurements have been certified by the Physikalisch-Technische Bundesanstalt Braunschweig (PTB). The steep decrease of the dose rate with depth is the reason that only superficial and near-surface tumours can be irradiated.

MCNP calculations of the neutron spectra and of the corresponding dose rates were carried out for various phantoms. Calculated neutron spectra for a PE phantom using an MCNP code are shown in Fig. 8.7.

Two current projects deal with the experimental determination of the neutron spectra at SR10. One method uses a set of passive Bonner spheres with gold probes. The activation data of the probes activated in the center of the spheres with sizes up to 15" undergo a deconvolution procedure with respect to the spectral response of the spheres. The project is carried out together with the Institut für Strahlenschutz at GSF Neuherberg, Germany (H. Paretzke, W. Rühm, S. Studeny), and is part of an ongoing PhD thesis.

For radiation protection purposes it is necessary to know the neutron spectra also outside of the heavily shielded irradiation rooms. For this sake, 16

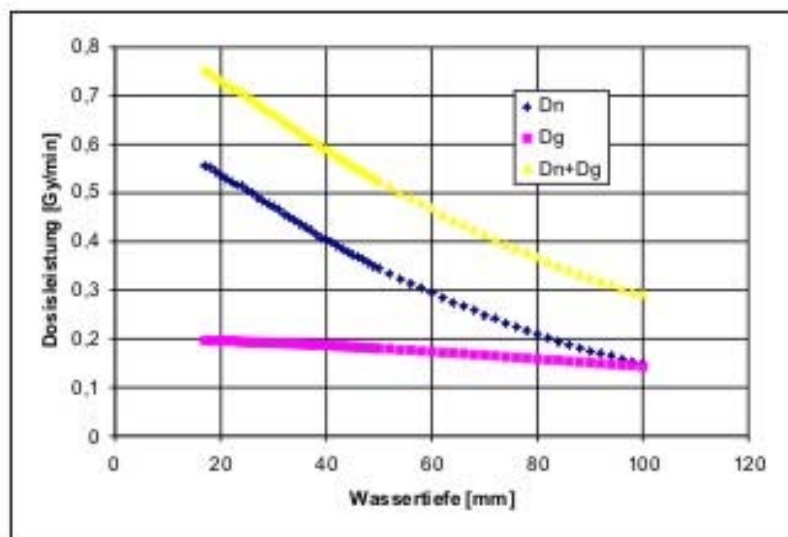


Figure 8.6: Neutron and gamma dose rates D_n and D_g , resp., vs. depth in a water phantom on the beam axis using the medical filter combination.

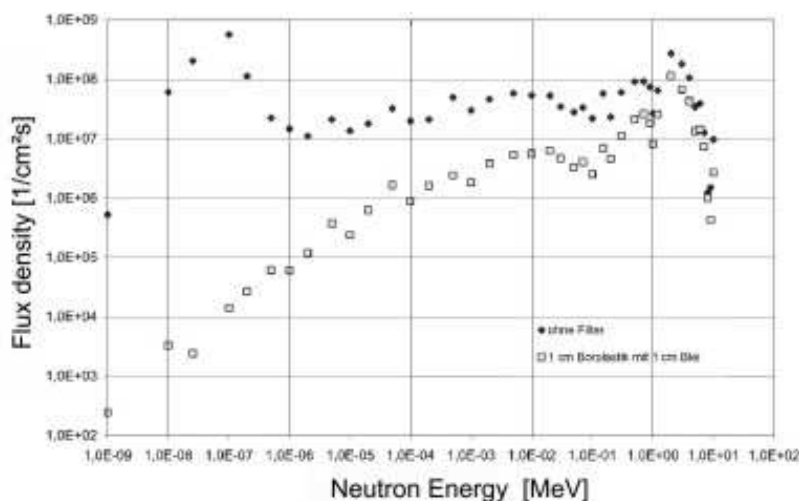


Figure 8.7: Monte-Carlo simulation of the neutron spectrum at the patient site. Closed rhombi: unfiltered beam; open squares: beam filtered by 1 cm B_4C -PE and 3.5 cm Pb

active PE spheres with sizes ranging from 2.5" to 15" were placed at 3 sites. In this case, the more sensitive He-3-counters are placed amidst of the spheres instead of gold probes.

Measurements of lineal energy transfer spectra by use of the microdosimeter AMIRA (from Strahlenbiologisches Institut, Universität München, LMU), and dose measurements with the newly developed electronic personnel dosimeter on a PMMA phantom (M. Wielunsky) accomplished the action with GSE.

Towards the end of 2006, another method to determine fast neutron spectra has been started within a diploma

thesis using threshold reactions of Rh-103, In-115, Ti-47, P-31, Zn-64, Fe-54, Al-27, and others (H. Breitreutz). In contrast to the Bonner sphere method, the use of threshold probes allows for measurements within a phantom and for spatial resolution.

Biological beam quality

In context with the clinical application of the beam, the determination of the Relative Biological Effectiveness, RBE, is of great importance. In a master thesis by V. Magaddino (University of Naples,

Italy), the dependence of the RBE of fission neutrons on dose and on gamma contamination has been investigated in megacolonies of human squamous cell carcinoma [3]. This project was conducted within the course "European Master of Science in Radiation Biology" under the auspices of the University College London (K.-R. Trott), and in co-operation with the Radiobiological Institute of the University of Munich, LMU (J. Kummermehr). It was shown that fractionation and depth in phantom give rise to a variation of the RBE from 1.4 to 4.7. The investigation will be continued.

Preparation for clinical applications

In order to be applied to humans, MEDAPP had to be checked according to the Medical Devices Directive, MDD 93/42/EEG. After an effort of about 10 man-years, the CE mark has been fixed at the facility. The permission for patient treatment is pending.

For the administration of the patients' personal data, the program RISSKA was developed in the medical faculty of TUM (Thamm) [4]. This program also allows for controlling the administered single doses, the number of fractions, and for documenting the applied irradiation field (i.e. doses, position of the multi leaf collimator, position of the patient) can be reported by words and by implemented photo documentation. RISSKA offers also data base functions and statistical features for the evaluation of patient and irradiation data.

- [1] Kampfer, S., Wagner, F., Loeper, B., Kneschaurek, P. *Medizinische Physik*, 318–319.
- [2] Loeper-Kabasakal, B., Thamm, R., Kampfer, S., Wagner, F., Kastenmüller, A., Lange, W., Kneschaurek, P. *ESTRO 25*, poster 892.
- [3] Magaddino, V. *Thesis for the Degree of Master of Science in Radiation Biology*. Master's thesis, University College London (2006).
- [4] Thamm, R., Loeper, B., Wagner, F., Molls, M. *DEGRO*, (2006).

Part II
Science

9 Scientific highlights

9.1 Solvent content in thin spin-coated polymer films

J. Perlich¹, V. Köstgens¹, L. Schulz¹, R. Georgii², P. Müller-Buschbaum¹

¹Physik-Department E13, TU München

²ZWE FRM II, TU München

The detection of remaining solvent in thin polymer films is of importance due to its effect on chain mobility and film homogeneity. Moreover, it gives an estimate on possible aging effects caused by the reduction of the solvent content, which typically yield an increased brittleness.

In the present investigation, we focus on a well controlled model system, which consists of protonated polystyrene (PS) with different molecular weights M_w of 7, 27, 207, 514, 908, 1530 kg/mol, spin-coated out of protonated or deuterated toluene (solvent) onto silicon (Si) wafer substrates. Directly after spin-coating the thin PS films were investigated with neutron reflectivity (NR) at the MIRA instrument at a wavelength of 16 Å. A narrow q_z range (0 Å^{-1} to 0.02 Å^{-1}) around the critical edge was probed with high resolution. Due to the high sensitivity of the position of the critical edge on the ratio of protonated PS and deuterated toluene (toluene-d8), the exact position of the critical edge enables to determine the solvent content. In addition to the deuterated solvent samples, samples with thin PS films spin-coated out of protonated toluene were also prepared for a direct comparison of the different sample types [1]. In order to rule out all kinds of measurement errors precautions on the sample part, e.g. preparation and repetitions with different but identical samples, are very important. With respect to the instrument, a very accurate alignment of the experimental set-up is crucial for those measurements.

Experimental results

The recent experiment focuses *on two different key parameters* which influence the solvent content: the molecular weight of PS and the film thickness investigated in the range of 10 to 100 nm. Thus, two respective sample series were prepared. Focussing on the molecular weight as key parameter, thin PS films with a fixed thickness of 50 nm are investigated: The expected shift of the critical edge position, which is observed in neutron reflectivity simulations on this model system, is verified by the MIRA measurements. Figure 9.1a shows one particular example for a molecular weight of 7 kg/mol. In direct comparison the reflectivity of the sample prepared out of deuterated and protonated solvent is plotted. The intensity is shown on linear scale to emphasize on the region of total external reflection.

The obtained reflectivity data of thin PS films with different molecular weights and a fixed film thickness are

shown in figure 9.1b. The data show a shift of the critical edge with increasing molecular weight, although the measured critical edges of much higher M_w shift not completely but rather indicate a slightly changed slope of the critical edge. For the investigation of the film thickness as the second key parameter, PS with a molecular weight of $M_w = 207 \text{ kg/mol}$ is dissolved in toluene-d8. The thickness of the thin PS film is depending on the viscosity of the solution and thus the concentration of PS in the solution. Therewith the concentration is chosen in such a way to achieve a desired film thickness [2]. The thickness series comprises thin PS films of a thickness of 10, 30, 50, and 100 nm. Figure 9.2a shows the obtained reflectivity data for films with thickness of 10, 30 and 100 nm at fixed molecular weight. The data of the critical edge indicate an influence on the film thickness, but prevent a definite conclusion about the behaviour in dependence of the film thickness without fitting the data.

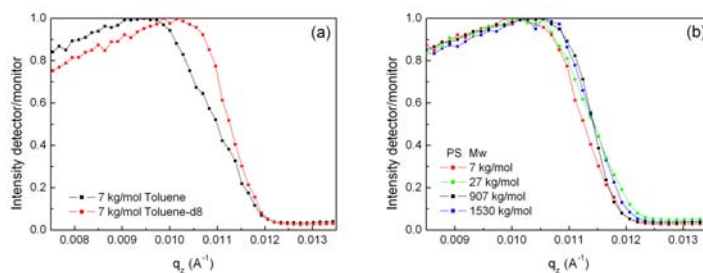


Figure 9.1: (a) Neutron reflectivity data obtained from spin-coated thin polystyrene (PS) films with a molecular weight $M_w = 7 \text{ kg/mol}$ and fixed film thickness. Depending on the use of protonated and deuterated (d8) toluene, the position of the critical edge shifts significantly. (b) Neutron reflectivity data of a selection of thin PS films prepared of different molecular weights M_w of 7, 27, 907 and 1530 kg/mol and fixed film thickness. With increasing molecular weight the position of the critical edge shifts towards higher q_z values.

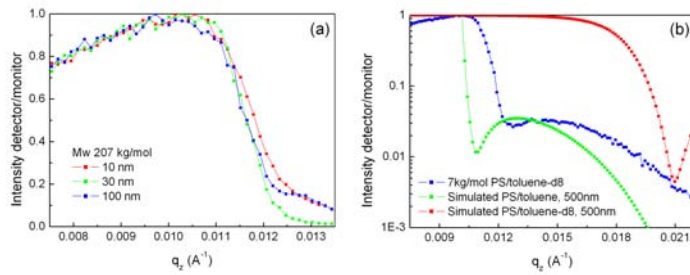


Figure 9.2: (a) Neutron reflectivity measurements from spin-coated thin films with PS molecular weight $M_w = 207$ kg/mol and film thicknesses of 10, 30 and 100 nm. An influence of the film thickness is indicated by the reflectivity data. (b) Simulated neutron reflectivity data for a single PS film on top of bulk Si. Simulated for a film SLD of protonated PS and deuterated toluene. Since the measured data is a mixture of both, the measured reflectivity lies within the simulated borders.

Data analysis

The simulation and data analysis of the neutron reflectivity measurements is performed with Parratt32, a simulation tool for neutron and x-ray reflectivity. The model layer stack in ambient air consists of bulk Si with a single layer on top, representing the PS film. In order to match the simulated curve with the measured curve of the PS/toluene-d8 film only the scattering length density of the PS film is adjusted, whereas the magnitude of the adjustment represents a measure for the ratio of protonated PS and deuterated toluene. Since the relation $SLD_{tol} < SLD_{PS} < SLD_{tol-d8}$ applies for the sample materials and since the film will be a mixture of PS

and toluene-d8, the SLD for deuterated toluene is a reasonable maximum for the adjustment. To rule out the indeterminateness of the PS film thickness, x-ray reflectivity (XRR) measurements are performed, since the NR measurements in the narrow q_z range provide no estimation of the PS film thickness. In figure 9.2b the NR simulations for a PS film are shown, whereas the measurements should lie within the regions defined by the extreme values of the SLD.

Summary and outlook

In summary, *the experiment was very successful*. A direct comparison indicates a clear distinction between thin films prepared of PS dissolved in protonated or deuterated toluene. This di-

rectly transforms into the amount of solvent remaining in the polymer film. Depending on the molecular weight of PS the shift of the critical edge is pronounced to a greater or lesser extent, but clearly visible. In total, the actual sample preparation conditions are of importance and affect the amount of solvent inside the PS films. As a consequence, well defined experimental conditions of the PS film are essential to work out the solvent content. Due to the close vicinity of the MIRA instrument and the polymer preparation laboratories, this is perfectly fulfilled.

Following MIRA experiments will be expanded to a technically more relevant sample system consisting of nanocomposite films, prepared by the combination of an amphiphilic diblock-copolymer, which acts as the templating agent, and an inorganic sol-gel chemistry. This particular nanocomposite films are employed in new photovoltaic devices. The investigation of such a system is of importance, since starting from the naturally remaining solvent content in the film after preparation and the subsequent decrease during aging alters the structural properties of the nanocomposite film and thus results in loss of performance.

[1] Spangler, L., Torkelson, M., Royal, J. *Polym. Eng. Sci.*, 307, (1990), 644–653.

[2] Schubert, D. *Polymer Bulletin*, 38, (1997), 177.

9.2 Investigation of AZ31 and ion irradiated Mg with the coincident Doppler broadening spectrometer CDBS

M. Stadlbauer¹, C. Hugenschmidt¹, K. Schreckenbach²

¹ZWE FRM II, TU München

²Physik-Department E21, TU München

The chemical vicinity of open volume defects in alloys is of great interest in material science since it is crucial for the stiffness and tensile strength. The coincident Doppler broadening spectroscopy (CDBS) with positrons allows very sensitive measurements of the electron momentum distribution in

defects due to the efficient trapping therein [1]. After annihilation with core electrons from the neighboring atoms, the Doppler shifted 511 keV annihilation radiation reveals the momentum distribution of the involved electrons which depends in particular on the periodic number of the element. A

detailed description of CDBS and the CDBS-spectrometer at NEPOMUC has been published in [2].

Sample Preparation

Samples with $20 \times 20 \times 3$ mm³ consisting of pure, polished and annealed Mg

have been irradiated with Mg-, Zn- and Al-ions at the 3 MeV-Tandetron in Rossendorf. The energy of the ions were chosen between 1.4 and 3 MeV according to $2.3\ \mu\text{m}$ mean implantation depth. Implantation of Mg-ions into a Mg-sample ensures that only defects change the CDBS-signature. Zn and Al ions were implanted into Mg in order to study the influence of these elements to the CDBS-signature in combination with defects. Single defects and dislocations created by this treatment in magnesium anneal already below 200 K but vacancy clusters survive up to 400 K [3]. For each ion type a set of 4 samples was produced with doses between 3×10^{13} and 3×10^{16} ions/cm² in order to find a sensitivity threshold for the low doses on the one hand and to get into the region of saturation trapping of positrons for the high doses on the other hand.

The diameter of the ion beam from the tandetron was reduced to 5 mm since spatially resolved positron scans with a resolution of 2 mm should image the ion beam spot on the sample.

Additional samples consisting of pure, polished and annealed AZ31 were irradiated with Mg-ions of 1.4 MeV energy. The same doses were applied as described above.

Measurements and results

The samples with the maximum ion dose were measured up to now. First, the width of the annihilation line vs. position and energy was recorded with a spacial resolution of 2 mm and positron energies between 1 and 9 keV, since

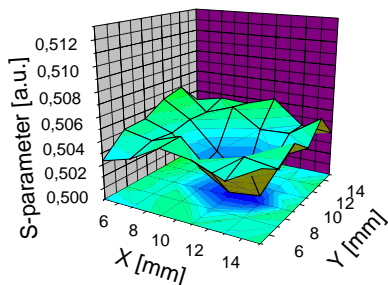


Figure 9.3: Width of the annihilation line in a.u. vs. position on the Mg-ion irradiated AZ31-sample measured with 4.5 keV positron energy.

the most obvious variation of this parameter was expected to occur at low energies due to results from previous measurements of the annihilation line width in the irradiated area (see fig.9.3) which can be clearly detected between 1 and 6 keV. For higher energies the irradiated region could not be separated from the untreated one which is an unexpected result, since the mean penetration depth of the Mg-ions was $2.3\ \mu\text{m}$ corresponding to 17 keV positrons. A possible explanation for this is the very high ion dose ($c_{\text{ion}} = 35\%$ in the irradiated region), which may have led to local annealing effects due to local heating during the irradiation procedure.

The coincident spectra of pure Mg irradiated with Mg-, Al- and Zn-ions showed a clear deviation from the pure and untreated Mg-samples (see fig.9.4). Nevertheless the signatures of the irradiated samples are statistically not distinguishable among each other within the error bars between 511 and 513 keV. In particular there is no Zn-signature in the Zn-ion irradiated Mg-sample detectable. This signature is shifted to lower values between 513 and 514.5 keV in contrary to the Zn-curve

which shows a large deviation in the high momentum region.

Outlook

Since the high ion dose may have led to local annealing effects in the samples, the next important step is to measure the samples with lower ion dose. First investigations on these samples were very promising.

- [1] Puska, M. J., Nieminen, R. M. *Rev. Mod. Phys.*, 66, (1994), 841–897.
- [2] Stadlbauer, M., Hugenschmidt, C., Piochacz, C., Strasser, B., Schreckenbach, K. *Appl. Surf. Science*, accepted for publication.
- [3] Ehrhart, P. In Ullmaier, H., editor, *Atomic Defects in Metals*, 242 (Springer-Verlag GmbH, San Diego, CA, 1991).

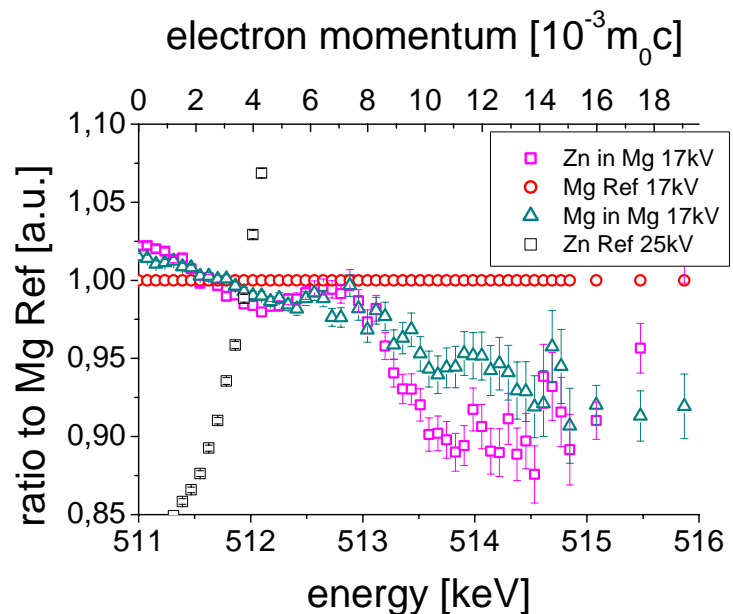


Figure 9.4: CDB ratio curves of pure Mg and irradiated Mg with Zn- and Mg-ions. The Zn-ion irradiated Mg-sample shows no Zn-signature and is clearly shifted towards the signature of the Mg-ion irradiated sample.

9.3 PAES-measurements of pure Cu and Cu coated Si(100)

Jakob Mayer¹, Christoph Hugenschmidt², Klaus Schreckenbach¹

¹Physics Department E21, TU München

²ZWE FRM II, TU München

Experimental setup

A spectrometer for positron annihilation induced Auger electron spectroscopy (PAES) has been installed at the high intensity positron beam NEPOMUC. PAES is based on the same principle as conventional electron induced Auger electron spectroscopy (EAES), but with different preceding ionization process. Since electrons in an atom are bound with high energy, the incoming electrons need an energy of at least a few keV to ionize the atoms by impact. At PAES the ionization is realized by electron-positron annihilation and hence positrons with a very low kinetic energy are sufficient ($E_{e^+} \leq 40$ eV). Due to the low positron energies, there is no background in the higher energetic regions of the Auger peaks. (n, γ)-reactions of surrounding experiments in the experimental hall at the FRM II initially led to a higher background than expected (see fig. 9.5). With the help of a lead shielding this external background has been reduced considerably.

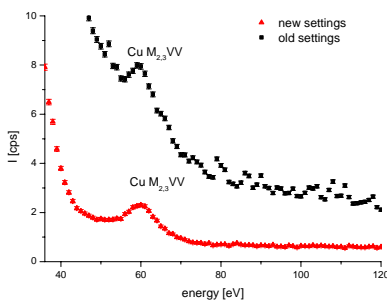


Figure 9.5: Old PAES-measurements of Cu in comparison with the new measurements (without background). The background was reduced by lead shielding and improved settings of the electric lenses at the entrance of the analysis chamber.

Characteristics of the positron beam at the sample site

The energy of the positrons is defined by the electric lenses and platinum structure in the tip of the NEPOMUC-beamtube [1]. In order to measure the energy distribution of the primary positron beam, the energy of the 30 eV positrons at the entrance of the analysis chamber was measured using a retarding grid in the longitudinal magnetic guiding field and a NaI-detector. In addition the geometric dimensions of the beam have been specified with a MCP and a CCD.

Since only a little fraction ($< 0.6\%$) of the positrons has a higher energy than the expected 30 eV the influence of them to the background is almost negligible. The diameter of the beam was determined to 20 mm.

Measurements and results

Figure 9.5 shows the reduction of the background due to the lead shielding and enhanced settings of the electric lenses at the entrance of the Auger chamber. The signal to noise ratio with PAES was increased from 1/2 to 2 and is hence a factor of 6 higher than with conventional EAES.

Another feature of PAES, the very high surface sensitivity, was demonstrated with a measurement of clean silicon and of the same sample covered with 1.5 monolayer of copper (see fig. 9.6). At the coated sample almost 1/5 of the whole Auger-signal, i. e. the sum of all detected Auger electrons, originates from copper. With EAES this quotient is only 1/13, since the electrons penetrate

deeper into the Si-substrate. This shows the high surface sensitivity of PAES.

Outlook

The results of the recent year show the high potentials of this unique facility. For a further reduction of the measurement time a new electron energy analyzer is required, since the current analyzer has an extremely low detection efficiency. With a new analyzer the detectable area will be enlarged and with nine channeltrons instead of one or even a MCP the measurement time is expected to be reduced at least by a factor of 50. With this investment and a new sample holder for the heating and cooling of the samples the PAES-spectrometer enables temperature dependent surface investigations.

[1] Hugenschmidt, C., Kögel, G., Reppe, R., Schreckenbach, K., Sperr, P., Triftshäuser, W. *Nuclear Instruments and Methods in Physics Research B*, 198, (2002), 220–229.

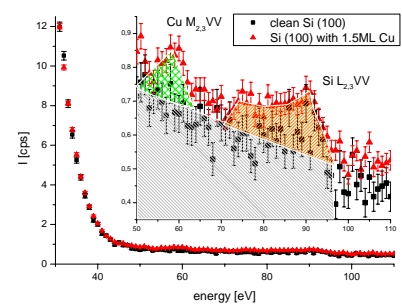


Figure 9.6: Single crystalline clean silicon and the same sample covered with 1.5 atomic layers of copper.

9.4 ANTARES – Investigation of an early medieval sword by neutron tomography

Martin Mühlbauer², Elbio Calzada², Brigitte Haas-Gebhard³, Rupert Gebhard³, Klaus Lorenz¹, Burkhard Schillinger², Michael Schulz²

¹ Physics Department, E21, TU München

²ZWE FRM II, TU München

³Archäologische Staatssammlung, München, Germany

We have studied a sword of the 6th century AC from Pforzen near Kempten, Germany. During a complex restoration parts of the scabbard that was constructed of different layers of leather and wood could be conserved. It was presumed that these parts still contain organic material. Therefore it was of interest for us to compare the results of the x-ray analysis to neutron radiography and tomography measurements, as neutrons are sensitive to the hydrogen in the remaining organic material, which is completely invisible for x-rays. This assumption could be verified by the examination results.

Introduction

The preservation of archaeological artifacts depends on the various corrosion processes of the artifacts during burial. Since wetland finds are scarce in Bavaria and dry or cold preservation is missing, organic material is very rare. There are however a few cases of preservation of organic parts sticking to metallic artifacts in early medieval burials. They are mainly conserved by iron oxides diffusion into the organic parts. In most cases the organic material was totally converted into iron or copper oxides, sometimes however organic material could remain.

The results of the neutron tomography allow a reconstruction of the organic scabbard. It was constructed of two wooden parts that have been covered at the inner side with leather or skin and leather at the outer side. This construction has been strengthened by winding a string around near the top part of the scabbard. Additionally some bronze parts are mounted at the tip of the scabbard and where it is attached to the belt. The center part of the sword blade was decorated in damask tech-

nique. This however could also be observed by x-ray techniques.

The organic parts are shown very well by neutron tomography. The attenuation of the neutron beam caused by the organic material is enhanced due to the conservation treatment by resins. The diffusion of these resins within the object is uneven. Neutron tomography could therefore be used to check the

conservation process as well. The investigated sword is property of the Free State of Bavaria and kept in the Archaeological State Collection (Archäologische Staatssammlung) in Munich [1].

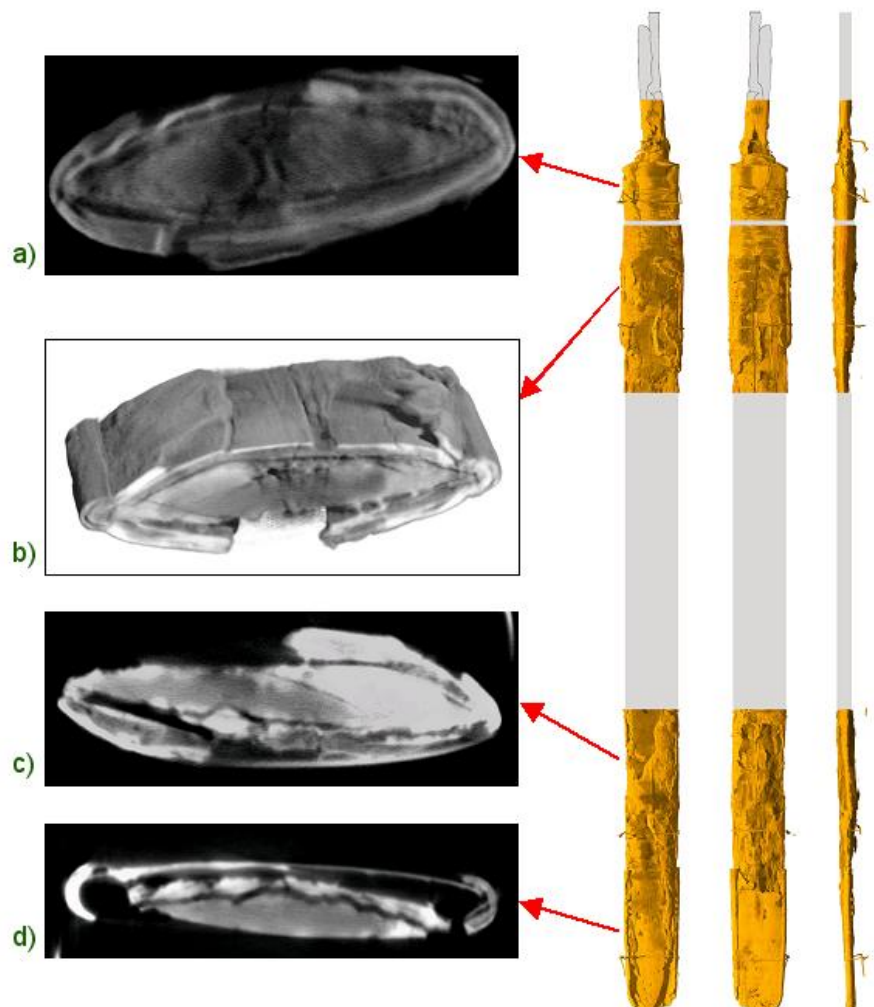


Figure 9.7: Right: overview of the four tomography data sets taken from the sword and the scabbard, left: different slices and cuts of the reconstructed data.

The neutron radiography and tomography facility ANTARES at FRM II

The measurements were carried out at the neutron radiography and tomography facility ANTARES, which is operated by the Institute for experimental physics E21.

By exchanging a part of the main collimator the effective aperture diameter of the collimator system can be reduced from 4.1 cm to 2.15 cm. Thus two main beam geometries are available at ANTARES, which result in L/D ratios of 400 and 800 respectively. The corresponding neutron flux at the sample position after a 16 m flight path is $1.0 \cdot 10^8 \text{ s}^{-1} \text{ cm}^{-2}$ or $2.5 \cdot 10^7 \text{ s}^{-1} \text{ cm}^{-2}$. Additional apertures made of cadmium allow to increase the L/D ratio up to about 16000. These apertures are used for phase contrast measurements predominantly. The energy spectrum of the neutron beam can be described by a Maxwellian distribution for thermal neutrons with an enhancement in the cold energy range due to the cold source filled with liquid deuterium at 25 K in front of the radiography beam tube. The maximum beam size at the sample position is 40 cm by 40 cm.

The detector system we used for the measurement was a CCD-camera in combination with a scintillation screen. The field of view was set to 14 cm by 14 cm and a L/D ratio of 800 was used. One scan showing the complete sword and four tomography data sets showing only parts of the sword were taken. Two of the data sets display an upper part and two form a lower part of the scabbard and the sword (fig. 9.7). The distance of the axis of rotation of the sample to the scintillator was 10 cm

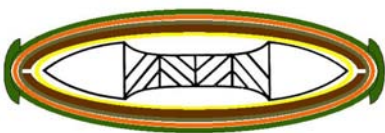


Figure 9.8: Sketch of the structure of the scabbard. From the inside to the outside it is built from fur, wood, leather, cord, bronze.

and the minimum distance of the sample surface to the scintillator was about 8 cm. For each radiograph the exposure time was 20 seconds. As 400 projections over 180 degrees were taken for each tomography data set, it required 3 hours to acquire the raw data of one tomography (readout time included). The achieved resolution was limited by the scintillator to about 0.5 mm.

Results

The scabbard is composed from the inside to the outside of different layers: fur, wood, leather, cord, bronze. The structure of the composition of the scabbard is visible in cuts through the three dimensional dataset. So it is possible to check the existence and condition of the different layers over the whole length of the sample.

These layers are not existent on the whole scabbard, e.g. the bronze strengthening is only placed at the tip of the scabbard and where it is attached to the belt of the warrior. For a sketch showing the different layers of the scabbard see figure 9.8.

The two edges of the sword are still in good condition (fig. 9.9). The corrosion process starts in the center region of the sword where different iron material was used for the damask technique. A thin intermediate layer is found between the sword and the scabbard. Here small connections are found built from the fur on the inner side of the scabbard and the corrosion products of the sword.

Cracks in the wooden parts of the scabbard or in the sword can be found and followed. The same is true for the damask structure in the core of the sword.

At the tip of the sword a small part has broken away from the rest of the sword (fig. 9.10). This is not visible from outside because of the bronze cover.

We found a heavily attenuating part at the cone end of the scabbard. At first we were wondering if it could be a part of the sword, which had been separated from the blade. We could not explain why its position was so close to the border of the scabbard. It seemed

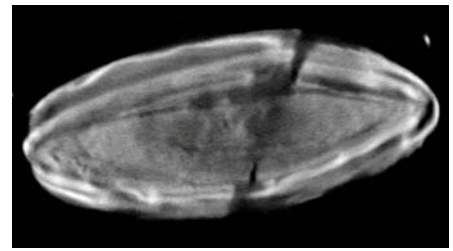


Figure 9.9: Cut through the reconstructed 3D data set showing a crack in the scabbard.

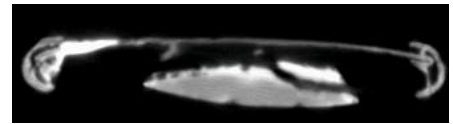


Figure 9.10: Small piece of the blade apart from the rest of the sword.

not to belong to the sword, because it was too far away from the rest of the sword and did not merge to it on either end. Then we compared the x-ray radiograph with the neutron radiograph again, and it turned out that it had to be an organic part, because it was only visible in the neutron radiograph (see fig. 9.11). The existence of this part was not known before and it was unclear why it was placed there. It is likely that it was used to fix the tip of the sword when it was placed in the scabbard. This special construction was detected on other early medieval swords for the first time. It takes further investigations to verify this construction element on other early medieval scabbards. It has to be discussed if this part was a general construction element or it was only applied at the sword of this study in connection with a repair after the loss of the bronze plate at the back side of the tip of the scabbard.

Conclusions

The application of neutron radiography and tomography methods in this field of archeology is a very useful non-destructive technique for the study of the inner structure of archaeological artifacts. Comparable results could only be achieved by mechanical removal of the different layers of the object. This

however would destroy the objects irreversibly. Neutrons are not the only tool to investigate archeological objects, but they give further information to complete the research results. In combination with x-ray measurements archeological objects can be investigated without damage or loss of material. X-rays show primarily the remains of the metallic sword while neutrons show the surrounding organic material in addition. Thus it is easy to focus on the sword using x-rays. The organic material of the scabbard is suppressed. This was very important to ensure that the strong attenuating part found at the cone end of the scabbard was wooden. Looking at the scabbard from the outside, it does not give the impression of organic material due to the heavy uptake of metal oxides during the decomposition process.

The wooden part to fix the tip of the sword is an example for a perfect complement of x-rays and neutrons.

Acknowledgment

We thank the restoration department of the Archeological State Collection Munich for sample preparation and providing the x-ray data.

[1] Archeologische Staatssammlung.
<http://www.lrz-muenchen.de/~arch/start.html>.

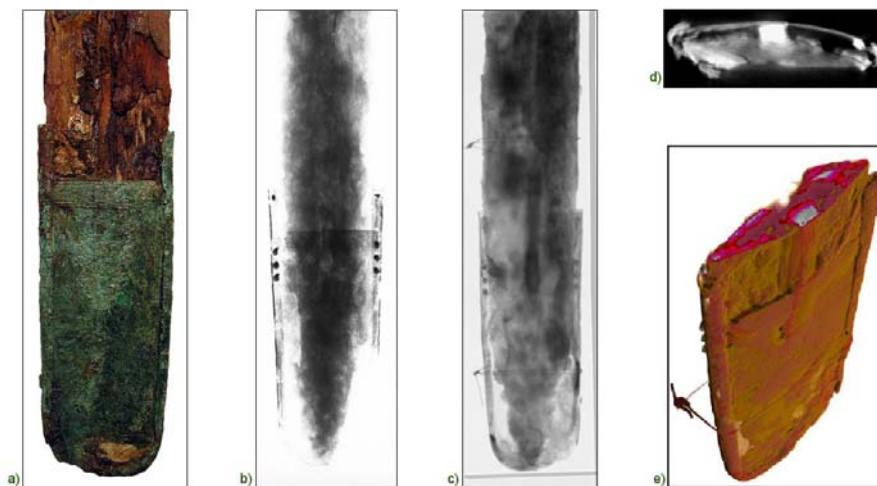


Figure 9.11: Comparison of x-ray radiography (b) and neutron tomography (c): A strip of wood could be detected under the bronze metal sheet that covers the front side of the scabbard. The bronze metal sheet of the backside has been lost in antiquity.

9.5 Containerless sample processing in combination with quasielastic neutron scattering

A. Meyer^{1,2}, S. Stüber², D. Holland-Moritz¹, O. Heinen¹, T. Unruh³

¹Institut für Materialphysik im Weltraum, Deutsches Zentrum für Luft- und Raumfahrt, Köln

²Physik Department E13, TU München

³ZWE FRM II, TU München

The study of structure and dynamics in liquid metals is often prevented by a chemical reaction of the high temperature melt with its sample holder. This can be overcome by the use of an electromagnetic levitation apparatus (EML) that allows for a containerless processing of electrically conducting samples. At the DLR in Cologne a compact and mobile EML was designed and built for

the use on neutron diffractometers [1]. The absence of a sample holder made it not only possible to extend the accessible temperature range for liquid metals research up to 2300 Kelvin, but also to undercool liquid metals and alloys several hundreds of Kelvin below their melting points. This led to new findings concerning the short range order in liquids [2].

The roughly spherical, electrically conductive samples, 6-8 mm in diameter, are levitated within an inhomogeneous electromagnetic radio frequency field.

As a result of the RF-field, eddy currents are induced in the specimen. On the one hand, this leads to an inductive heating of the sample which allows melting of the specimen. On the



Figure 9.12: Electromagnetically levitated liquid Ni droplet at a temperature of 1810 K. The water cooled copper coil is shielded with a neutron absorbing rubber. The radial collimator of ToF is on the right.

other hand, the interaction of the eddy currents with the inhomogeneous magnetic field of the levitation coil leads to a force that acts on the sample. According to Lenz's rule this force points into the direction of low magnetic field strength. If it is adjusted such that gravity is compensated, the sample is levitated. The convective stirring induced by the inductive currents in combination with a large heat conductivity of the sample results in a homogenous sample temperature that is contact-free measured with a two-color pyrometer. The temperature is controlled via the flow of ultra pure cooling gas (He/4% H_2 in the case of Ni) which is injected by a nozzle that is installed below the sample.

For the use on neutron time-of-flight spectrometers the EML was equipped with a newly developed Cu coil that provides an 8 mm gap between the upper and the lower part of the coil. This enhanced the visibility of the sample for the incoming beam and for the detectors significantly. In combination with the high flux and the excellent signal to noise ratio of the neutron time-of-flight spectrometer ToF-ToF quasielastic measurements on levitated metallic droplets are now feasible. In a first measurement campaign we investigated liquid Ni. Figure 9.13 displays the quasielastic signal that is dominated by incoherent scattering below about 2.2 \AA^{-1} . Please note the semilogarithmic representation of

the scattering law $S(q, \omega)$. The lines are fits with a Lorentz function that is convoluted with the instrumental energy resolution function. The q dependence of the quasielastic signal contains information on the mechanism of atomic transport. Via the width of the quasielastic line the self diffusion coefficient D can be derived on an absolute scale with high precision. Over a large temperature range – from more than 200 K above to more than 200 K below the melting point at 1727 K – the temperature dependence of the diffusion coefficients can be described with an Arrhenius law. The change from a liquid in thermodynamical equilibrium to a metastable liquid at large undercoolings is not reflected in its atomic transport [3].

With this new sample environment we are now able to study the interplay of structure, dynamics and properties e.g. of Fe and Ti based melts that form intermetallic phases and of Zr based melts that form bulk metallic glass at large undercoolings. In a next step we are developing an electrostatic levitator. Such a device will give access to even higher temperatures and to non metallic liquids.

It is a pleasure to thank Stephan Janssen and the FOCUS team of the Paul Scherrer Institute for their support during a first test experiment on FOCUS and Suresh Mavila Chathoth, Fan Yang, Tarik Mehaddene, Jürgen Brillo, Helena

Hartmann and Thomas Volkmann for their help. We acknowledge financial support by the German DFG (SPP Phasenumwandlungen in mehrkomponentigen Schmelzen) under Grant No. Me 1958/2-3 and Ho1942/6-3.

- [1] Holland-Moritz, D., Schenk, T., Convert, P., Hansen, T., Herlach, D. *Meas. Sci. Technol.*, 16, (2005), 372–380.
- [2] Schenk, T., Holland-Moritz, D., Simonet, V., und D.M. Herlach, R. B. *Phys. Rev. Lett.*, 89, (2002), 075507–075510.
- [3] Meyer, A., Stüber, S., Holland-Moritz, D., Heinen, O., Unruh, T. *Phys. Rev. Lett.*, (eingereicht).
- [4] Chathoth, S. M., Meyer, A., Koza, M., Juranyi, F. *Appl. Phys. Lett.*, 85, (2004), 4881–4883.

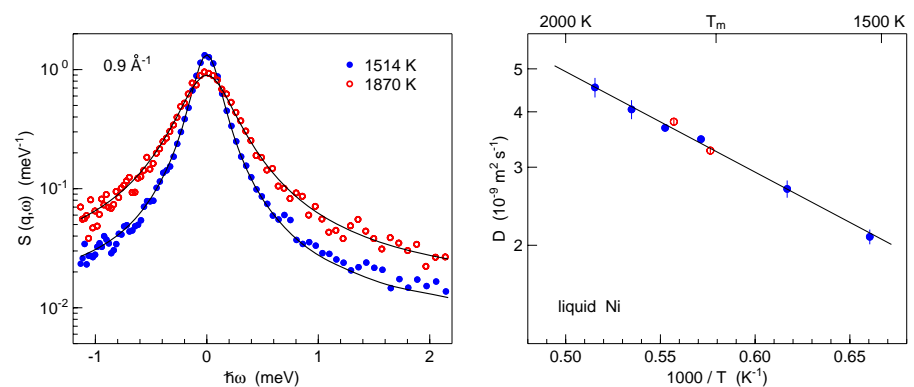


Figure 9.13: Quasielastic spectra of liquid Ni (left). Measuring times ranged from 1 h to 3 h. Ni self diffusion coefficients obtained from the width of the quasielastic line (right). The open circles are results from QENS measurements on liquid Ni in an alumina crucible [4].

9.6 Larmor diffraction at TRISP

T. Keller², K. Buchner², C. Pfeleiderer³, P. Böni³, B. Keimer¹

¹Max-Planck-Institute for Solid State Research, Stuttgart

²Max-Planck-Institute for Solid State Research, outstation at FRM II

³Physics Department E21, TU München

The TRISP (triple axis spin-echo) spectrometer at the FRM II is a thermal triple axis spectrometer incorporating the NRSE (neutron resonance spin-echo) technique. TRISP is optimized for high resolution spectroscopy of phonons and magnons with an energy resolution down to the μeV range [1, 2]. Here we report on the high res-

olution Larmor diffraction (LD) mode of TRISP, which was first proposed by Rekveldt [3, 4] and is also based on the NRSE technique with inclined field boundaries. LD at TRISP typically offers a resolution $\Delta d/d \approx 2 \times 10^{-6}$ for single crystal and powder samples, i.e. at least one order of magnitude more accurate than conventional neutron or x-ray diffractometers. LD is operated with open collimation and thus with a high intensity beam. Additionally the spread of the lattice spacing can be measured with high accuracy (typically $\Delta d/d \approx 10^{-5}$ FWHM for a Gaussian distribution). In a second mode, LD allows for accurate determination of the mosaic spread of single crystals.

During the last year, LD at TRISP was used for a series of thermal expansion measurements under extreme conditions with pressures up to 20kbar and temperatures down to 500mK (lower temperatures will be available) [5, 6]. This parameter range is interesting for a variety of systems showing unconventional phases or phase transitions. So far, no experimental technique was available to determine thermal expansion under these conditions with sufficient accuracy: Dilatometry has excellent resolution, but doesn't work in pressure cells. High resolution high energy x-ray diffraction offers typically a resolution around $\Delta d/d \approx 10^{-5}$, which is in most cases not good enough for meaningful thermal expansion measurements. Additionally it causes too much sample heating, thus the temperatures are limited to values above 4K. The resolution of conventional single crystal neutron diffraction in the order of 10^{-4} is also insufficient.

The basic idea of the LD technique is to mark each single neutron by a Larmor precession phase such that the phase only depends on the lattice spacing d and is independent of the Bragg angle or the velocity of the single neutron. Thus the resolution is inde-

pendent of the beam collimation and monochromaticity. The principle is shown in fig. 9.14a: an initially polarized neutron runs through a homogeneous magnetic field \mathbf{B} with the field boundaries oriented parallel to the lattice planes of the diffracting crystal. The initial polarization is perpendicular to \mathbf{B} . The total Larmor phase after passing \mathbf{B} twice (incident and scattered beam) is given by the time T the neutron spends in the field. T only depends on the components of $\mathbf{k}_{1,2}$ perpendicular to the field boundaries:

$$(9.1) \quad \phi_{tot} = \omega_L T = \omega_L L \frac{m}{\hbar} \left(\frac{1}{k_{1\perp}} + \frac{1}{k_{2\perp}} \right)$$

$\omega_L = 2\pi\gamma B$ with $\gamma = 2.916\text{kHz/Gauss}$ is the Larmor frequency. The Bragg condition requires that all diffracted neutrons have the same k -component perpendicular to the lattice planes:

$$(9.2) \quad k \sin \theta_B = G/2$$

where $G = 2\pi/d$ is the modulus of a reciprocal lattice vector. If the lattice planes are oriented parallel to the field boundaries, $k_{1\perp} = k_{2\perp} = G/2$ and the total phase is

$$(9.3) \quad \phi_{tot} = \frac{2m\omega_L L}{\pi\hbar} d$$

A change of the lattice spacing generates a phase shift

$$(9.4) \quad \Delta\phi = \phi_{tot} \frac{\Delta d}{d}$$

ϕ_{tot} can be as large as 10^4 rad. With a normalized distribution function $f(\Delta d)$ of the lattice spacing variations, the component of the neutron beam polarization measured by the analyzer is

$$(9.5) \quad \begin{aligned} P(\phi_{tot}) &= \langle \cos(\Delta\phi) \rangle \\ &= \int f(\Delta d/d) \cos\left(\phi_{tot} \frac{\Delta d}{d}\right) d\left(\frac{\Delta d}{d}\right) \end{aligned}$$

i.e. the cos-Fourier transform of $f(\Delta d)$. To test the performance of LD at TRISP, we measured the thermal expansion of a copper single crystal using the

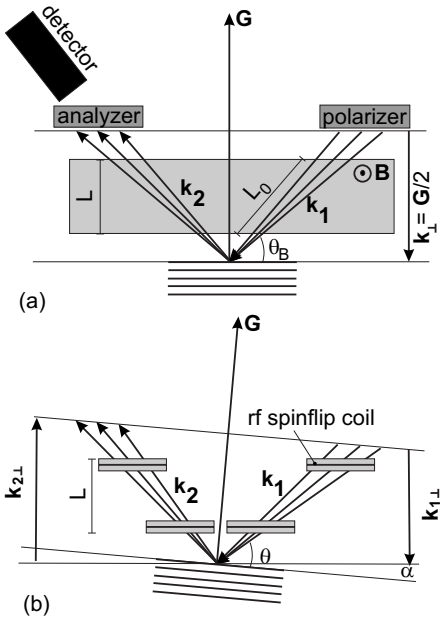


Figure 9.14: *Larmor diffraction setup* (a) basic principle: a polarized neutron beam travels through a field \mathbf{B} , where the neutron spins undergo Larmor precession. The precession phase is proportional to the component of \mathbf{k} perpendicular to the field boundaries, which is the same for all Bragg diffracted neutrons ($k_{\perp} = G/2$) if the field boundaries are parallel to the lattice planes of the diffracting crystal. Tilting the lattice planes by an angle α leaves the precession phase constant to first order ($k_{1\perp} + k_{2\perp} = \text{const}$). Thus the method also works for powder samples using beam divergencies in the order of one degree. (b) Larmor diffraction configuration at TRISP. The DC field B is replaced by two pairs of rf spinflip coils. The field boundaries are defined by the precise windings of these coils.

[111] reflection. Cu is a calibration standard for dilatometers and accurate data on the thermal expansion are available [7]. Fig. 9.15 shows the data obtained at TRISP and reference data from capacitive dilatometry (no fit!), where the accuracy of the dilatometric data is typically three orders of magnitude better than the TRISP data. The excellent agreement shows that the LD technique works reliable on a 2×10^{-6} relative error level. The accuracy of LD can be increased at least by one order of magnitude by increasing the length of the precession regions, by using longer wavelength neutrons and by careful control of the spectrometer stability, which is currently mainly limited by thermal drifts of the length of the precession regions.

- [1] Bayrakci, S., Keller, T., Habicht, K., Keimer, B. *Science*, 312, (2006), 1926.
- [2] Keller, T., Aynajian, P., Habicht, K., Boeri, L., Bose, S., Keimer, B. *Phys. Rev. Lett.*, 96, (2006), 225501.
- [3] Rekveldt, M. T. *Mater. Sci. Forum*, 321-324, (2000), 258.
- [4] Rekveldt, M. T., Keller, T., Golub, R. *Europhys. Lett.*, 54, (2001), 342.
- [5] Pfeleiderer, C., Böni, P., Keller, T., Rößler, U., Rosch, A. To be published.
- [6] Niklowitz, P., Pfeleiderer, C., Keller, T., Mydosh, J. To be published.
- [7] Kroeger, F. R., Swenson, C. A. *J. Appl. Phys.*, 48, (1977), 853.

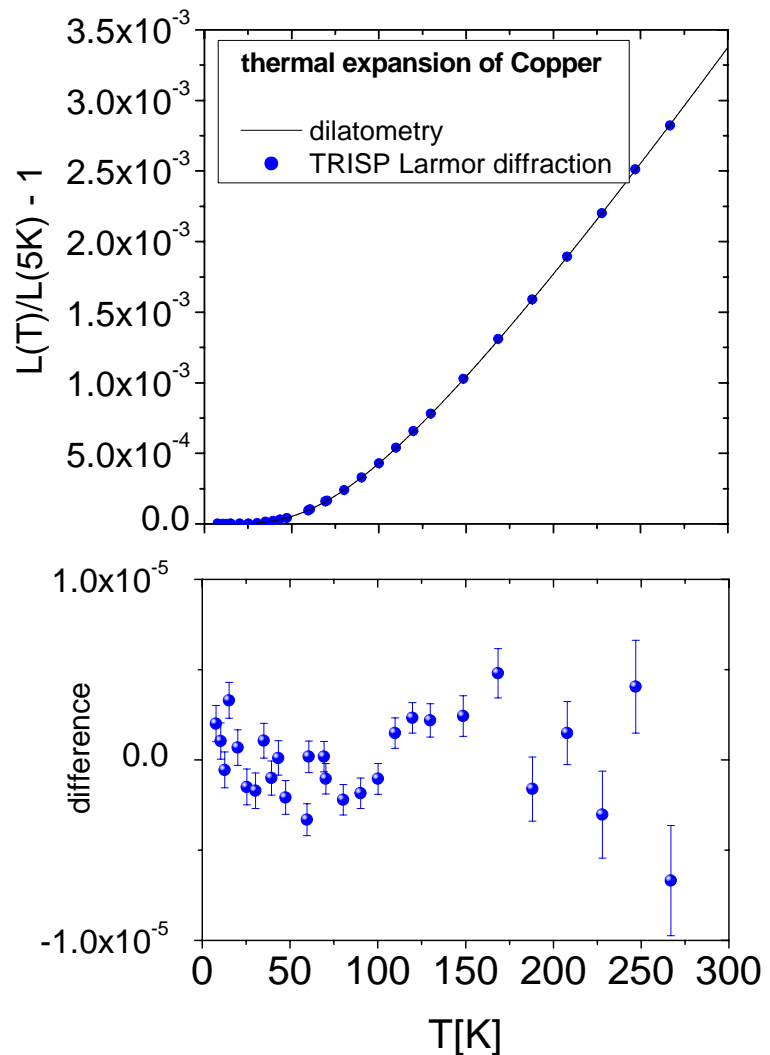


Figure 9.15: Thermal expansion of single crystal Cu [111] measured both with Larmor diffraction (dots) and dilatometry. In the lower part the difference between the LD and dilatometry data is plotted. The larger error bars above 150K result from thermal drifts in the order of 0.5K of the sample during the measurement.

9.7 Molecular dynamics in pharmaceutical drug delivery systems

C. Smuda¹, G. Gemmecker², H. Bunjes³, T. Unruh¹

¹ZWE FRM II, TU Muenchen

²Chemie Department, Organische Chemie II, TU Muenchen

³Institut fuer Pharmazeutische Technologie, TU Braunschweig

Introduction

In recent years it has been shown that the development of new drugs alone is not sufficient to ensure progress in drug therapy. Today there are many drugs which in spite of their high pharmacological potential cannot be administered using standard formulations because of e.g. side effects, targeting problems or adverse release effects. A promising strategy to overcome these problems is the development of suitable drug carrier systems [1]. Emulsions of liquid oils are under investigation for these purposes. During the development process it turned out that the material properties of the lipids used as matrix material may change dramatically upon dispersion into the colloidal state. One particular phenomenon is the highly extended supercooling range which has been observed among others for coenzyme Q₁₀. It has been proposed to use corresponding supercooled emulsions as drug carrier systems [2, 3]. For the dispersion of this substance an enhanced bioavailability has been demonstrated in cell culture experiments [4].

The dynamics of the carrier and the emulsifier molecules influence important technological properties of the formulation as the drug release rate or drug leakage. But only few investigations on the molecular dynamics of lipid drug delivery systems have been published so far. Quasi-elastic neutron scattering (QENS) is a quite unknown method in pharmaceutical science but it is a powerful tool to gain a deeper insight in the dynamics of drugs and excipient molecules leading to a better understanding of e.g. release behaviour of the drug.

In this article we present first results of QENS investigations on Q₁₀-nanodispersions which are of interest as drug carriers and exhibit an uncommon supercooling behaviour.

Further investigations on the dynamics of phospholipid molecules inside a monolayer stabilizing emulsion droplets are presented. Although phospholipids are used as stabilizers in many pharmaceutical dispersion formulations the stabilization mechanism especially during formation and crystallization of the particles, respectively, is not well understood.

Experimental details

The Q₁₀-nanodispersions were prepared by high-pressure homogenization of the molten Q₁₀ (10 weight%) and D₂O containing 1.6% phospholipid Lipoid S100 and 0.4% sodium glycocholate (SGC) as emulsifiers. The corresponding reference sample was prepared by the same procedure but contained only the two

emulsifiers and D₂O. The particle size was analyzed using photon correlation spectroscopy (PCS). The average radii (z -averages) for all Q₁₀-dispersions were in the range from 60 nm to 120 nm.

Four *n*-hexadecane-d34 (HD) nanoemulsions were prepared by means of high-pressure homogenization or ultrasonic homogenization. They contained 5% HD, 2% dimyristoylphosphatidylcholine (DMPC); 5% HD, 2% Lipoid S100; 5% HD, 1.6% DMPC, 0.4% SGC and 5% HD, 1.6% Lipoid S100, 0.4% SGC dispersed in D₂O, respectively. The reference sample was prepared by ultrasonic homogenization of a mixture of 5% HD and 2% sodium dodecylsulfate-d25 (SDS) in D₂O. The particle sizes (z -average) determined by PCS were in the range from 31 nm to 56 nm.

Neutron scattering measurements were performed with the time-of-flight

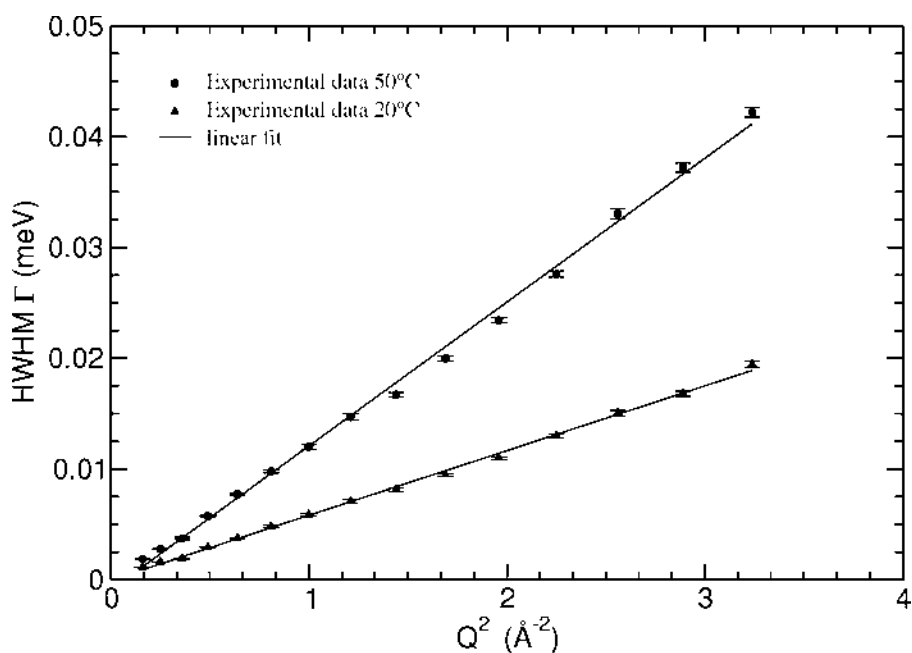


Figure 9.16: Observed half linewidth Γ of the first Lorentzian as a function of Q^2 for pure Q₁₀ at two temperatures. According to $D = \Gamma / (\hbar Q^2)$ the self diffusion coefficients could be determined from the slopes of the regression lines. For 293 K a diffusion constant $D = 8.7 \cdot 10^{-7} \text{ cm}^2/\text{s}$ and for 323 K a diffusion constant $D = 1.9 \cdot 10^{-6} \text{ cm}^2/\text{s}$ were calculated [5].

spectrometer TOFTOF at FRM II. Samples were measured with an incident wavelength of 6\AA and a chopper speed of 16000 rpm leading to an instrument resolution of about $35\text{ }\mu\text{eV}$. PFG-NMR diffusion measurements of Q_{10} dispersion and pure Q_{10} were performed on a Bruker DMX NMR Spectrometer operating at 600 MHz ^1H frequency.

Results

Self diffusion measurements of Q_{10} molecules and Q_{10} -nanodroplets in a dispersion

We have studied nanodisperse liquid Q_{10} (melting point: 320 K) in the molten and supercooled state and neat Q_{10} in the same temperature range.

The QENS spectra were fitted with a scattering function $S_{\text{inc}}(Q, \omega)$ which comprises of two Lorentzian functions, of which the first one describes the long-range diffusion and the second function approximates internal motions like methyl group rotation in Q_{10} , rotational motions of the whole Q_{10} molecule and chain motions of the Q_{10} molecule. The model function was convoluted with the resolution function of the instrument achieved from a vanadium measurement. From the first Lorentzian function a Q^2 dependence of the linewidth was obtained. The corresponding motion was assigned to a long-range diffusion. Exemplarily the Q dependence of the linewidth for two temperatures is displayed in Fig. 9.16. A physically meaningful interpretation of the Q dependence of the linewidth of the second Lorentzian function, however, could not be found so far, although a good description of the experimental data using this simple model was achieved.

Testing other models which include detailed expressions for superimposed long-range diffusion and isotropic rotational diffusion, or long range diffusion and uniaxial rotational diffusion and different models including restricted diffusion, respectively, it could be extracted as a result that the only constant and reproducible parameter achieved was the linewidth of the first

Lorentzian function, i.e. the derived self diffusion coefficients. No reasonable physical results for the other parameters of the scattering function could be obtained: e.g. the rotational diffusion coefficient has shown an unphysical Q dependence. Obviously we do not know enough about the dynamics which influences the scattering function. Therefore we started to investigate the local motions of Q_{10} in more detail which is described later in this article.

Q_{10} self diffusion coefficients determined at the same temperatures for nanoparticles and neat Q_{10} , respectively, exhibit no differences within the statistical error. Hence no "nanoeffect" owing to the dispersed state could be found. But this was not expected in the investigated size range of the nanoparticles since the size of the droplets ($\sim 120\text{ nm}$) is still large in relation to the size of a Q_{10} molecule ($\sim 6\text{ nm}$). However, it could be demonstrated that subtracting QENS spectra of the matrix (D_2O) from the spectra of the dispersion lead to nearly identical QENS spectra of dispersed and bulk Q_{10} . This is an important result for further investigations and not self-evident taken into account potential interactions of the dispersed phase with the dispersion medium and the scattering of the emulsifier.

PFG-NMR diffusion experiments for

a Q_{10} -nanodispersion and liquid Q_{10} were performed. This method provides self diffusion constants on a millisecond timescale. Interestingly the measured NMR values for neat Q_{10} are smaller compared to the QENS diffusion constants. For 293 K the self diffusion constant determined by PFG-NMR is $D_{Q_{10}} = 3 \cdot 10^{-8}\text{ cm}^2/\text{s}$ and this is 29 times smaller than the QENS value and for 323 K we found $D_{Q_{10}} = 1 \cdot 10^{-7}\text{ cm}^2/\text{s}$ which is by a factor of 20 smaller than the QENS diffusion constant.

The diffusion constant of the nanodroplets inside the dispersion medium at 293 K yielded a diffusion constant of $4 \cdot 10^{-8}\text{ cm}^2/\text{s}$. This diffusion constant is in perfect agreement with values estimated from PCS measurements [5].

Methyl group dynamics in Q_{10}

In order to get more information on the local motions in pure Q_{10} , the rotation of the methyl groups of the Q_{10} molecules in the nanodroplets was studied at low temperatures between 50 K and 200 K. This dynamics should dominate the scattering function in the given temperature range. According to the different local environment of the methyl groups in the amorphous Q_{10} samples we applied the rotation rate distribution model (RRDM) [6] to our

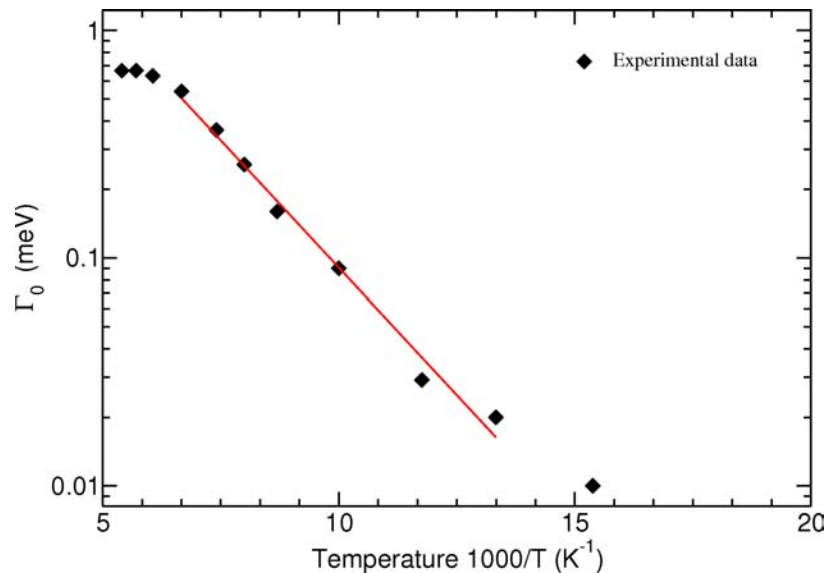


Figure 9.17: Temperature dependence of the most probable jumping rate Γ_0 obtained from fits of amorphous Q_{10} in the emulsion droplets.

QENS data. In this model a rotational jump process for the methyl group is assumed with variable rate constants distributed according to a logarithmic normal distribution around the most probable jump rate Γ_0 .

A good agreement of the model with the data was found for temperatures from melting point to 180 K. From the Arrhenius plot which is displayed in Fig. 9.17 an activation energy of 4.3 kJ/mol was extracted. This is in good agreement to values found for similar substances [7] taken into account a mixture of different types of methyl groups in the Q₁₀ molecule. The deviation of the data at higher temperature from the linear behaviour seems to be caused by the soaring recrystallization of the nanoparticles with increasing temperature. A model describing this effect is currently under investigation.

Phospholipid dynamics in monolayers

From temperature resolved QENS measurements on emulsions of perdeuterated *n*-hexadecane in D₂O stabilized with different emulsifiers information of the dynamics of the phospholipid molecules in the stabilizing monolayer could be extracted. The scattering contributions of the continuous phase and of the interior of the hexadecane droplets were removed by subtraction of the scattering curves of the reference sample. Therefore the obtained scattering curves are dominated by the scattering of the emulsifier molecules. It was enhanced even more by using phospholipids as the only protonated component of the formulation.

For our first experiments we selected DMPC which is a well investigated phospholipid and Lipoid S100 which is used as a standard emulsifier in pharmaceutical formulations. Sodium glycocholate was used as a co-emulsifier in the same samples.

In spite of a very small amount of only 20 mg phospholipid in the beam it was possible to detect changes of the phospholipid dynamics due to temperature change and temperature induced phase transitions. Exemplarily the neu-

tron scattering spectra of DMPC in the monolayer of *n*-hexadecane-d₃₄ nanoemulsions are displayed in Fig. 9.18. The reduced elastic line intensity of a dispersion stabilized with DMPC and SGC compared to a dispersion stabilized only with DMPC indicates that the addition of SGC increases the mobility of the DMPC molecules. This enhanced mobility of DMPC might be responsible for a better stabilization of lipid nanodispersions when adding SGC which could in fact be observed for similar dispersions during and after the crystallization of their liquid nanodroplets [8].

Furthermore, the temperature dependence on the elastic scattering intensity is stronger for the samples containing DMPC compared to the corresponding samples containing S100 as the phospholipid component. This effect, which is particularly obvious for the temperature step from 20°C to 30°C can be attributed to the gel/liquid-crystalline transition of the DMPC monolayer [5]. However, due to the poor counting statistics a quantitative analysis of the QENS-signal will only be possible from further experiments with

higher emulsifier concentrations and extended beam time.

- [1] Mehnert, W., Maeder, K. *Adv. Drug Del. Rev.*, 47, (2001), 165–196.
- [2] Bunjes, H., Siekmann, B., Westesen, K. *Submicron Emulsions in Drug Targeting and Delivery* (Harwood Academic Publishers, 1998).
- [3] Siekmann, B., Westesen, K. *Pharm. Res.*, 12, (1995), 201–208.
- [4] Stojkovic, M., Westesen, K., Zakhartchenko, V., Stojkovic, P., Boxhammer, K., Wolf, E. *Biol. Reprod.*, 61, (1999), 541–547.
- [5] Unruh, T., Smuda, C., Gemmecker, G., Bunjes, H. *Mater. Res. Soc. Symp. Proc.*, 137.
- [6] Chahid, A., Alegria, A., Colmenero, J. *Macromolecules*, 27, (1994), 3282–3288.
- [7] Mukhopadhyay, R., Alegria, A., Colmenero, J., Frick, B. *Macromolecules*, 31, (1998), 3985–3993.
- [8] Siekmann, B., Westesen, K. *Pharm. Pharmacol. Lett.*, 1, (1992), 123–126.

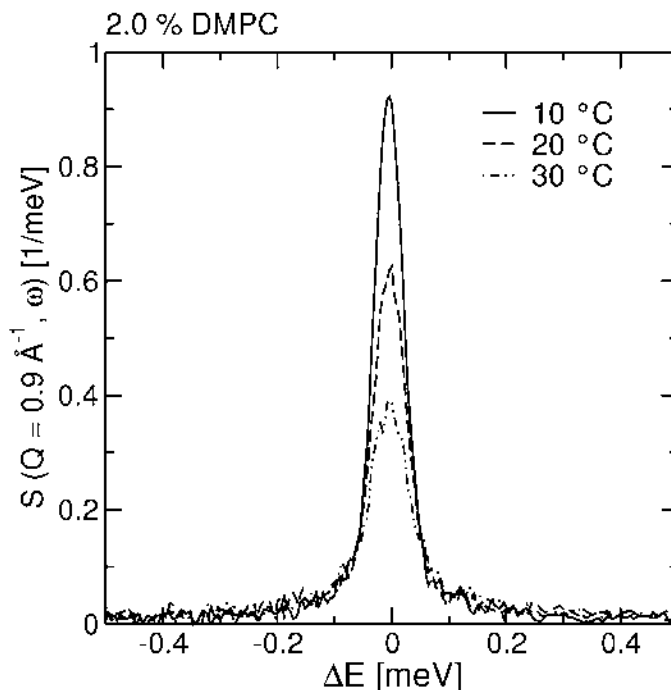


Figure 9.18: QENS spectra of DMPC in the monolayer of *n*-hexadecane-d₃₄ nanoemulsions at different temperatures. The displayed spectra were obtained after subtraction of the spectra of the fully deuterated reference sample.

10 Events

10.1 Workshop - Residual stress analysis

Michael Hofmann¹

¹ZWE FRM II, Technische Universität München

On the invitation of FRM II and the chair of metal forming of the TU München (Prof. Hoffmann) the annual meeting 2006 of the committee for residual stress (FA13 "Eigenspannungen") of the AWT (Working group of thermal treatment and materials science - Arbeitsgemeinschaft Wärmebehandlung und Werkstofftechnik e.V.) was held in Garching from the 30.-

31.5.2006. The chairman, Prof. Scholtes (University of Kassel), could welcome more than 60 participants to the two-day workshop. The talks on the first day mainly focused on possibilities and prospects of residual stress analysis using neutron diffraction methods. During the second day several aspects of the virtual institute "Photon and Neutron Research on Advanced Engineer-

ing Materials", which was introduced in the beginning by Prof. Reimers (Technical University Berlin), were presented and discussed. After the meeting most of the participants took the opportunity to visit the research reactor and to view the experimental halls and the instrumentation of FRM II.

10.2 Workshop - Neutrons for Geoscience

Jürgen Neuhaus¹

¹ZWE FRM II, Technische Universität München

The workshop Neutrons for Geoscience, organized by the Forschungsneutronenquelle Heinz Maier-Leibnitz FRM II, took place on July 14th in Garching. The aim was to bring together scientists from the broad range of earth sciences as geology, crystallography, mineralogy and others using neutron beams for their research. Invited talks as well as short contributions gave an overview of actual and future applications of neutrons in these scientific fields. Around 45 participants followed the presentations in the new lecture hall of the faculty of mathematics, where the workshop took place.

Hans Keppler from the Bavarian Geoinstitut, Bayreuth started the presentations with an overview on experiments under extreme conditions, i.e. high pressure and temperature simultaneously. These in-situ experiments can give new insights in the physics of the earth mantle. Focusing on texture investigations, Bernd Leiss from the Center of Geoscience, Göttingen gave an

impressive talk starting from the cloud building in the sky to the inner parts of the earth. Especially the large sam-

ple volumes of the rock material necessitates the usage of neutrons beams for a quantitative analysis. Simon Redfern



Figure 10.1: Participants of the workshop including the organizing team.

from the Department of Earth Sciences in Cambridge gave new insights what combined high pressure and temperature research using neutron scattering can investigate. Unconventional neutron scattering techniques were presented by Bjoern Winkler from the Institute of Geosciences, Frankfurt. He demonstrated how besides the traditional diffraction experiments investigations using inelastic, quasi-elastic and magnetic scattering as well as SANS and radiography/tomography are applied for research in the earth science. In the last presentation Karsten Knorr from the Institute of Geoscience, Kiel reviewed the development of high pressure cells and presented recent experiments taken at the FRM II.

During lunch break the poster session took place including presentations of the instruments from the FRM II. Lively discussions about recent and future experiments pointed out the large interest of the geoscience community to use the experimental facilities of the FRM II.

The workshop closed by a summary of Winfried Petry who was impressed by the large variety of methods starting from neutron diffraction to inelastic scattering, activation analysis and



Figure 10.2: Enthusiastic discussion of Winfried Petry (right) with experts from Göttingen (from left to right: Bent Hansen, pensive, Bernd Leiss, astonished and Götz Eckold, not yet convinced).

imaging techniques applied to research in the earth sciences. He emphasized the interest of the FRM II to establish the infrastructure for experiments under extreme conditions, especially for the geoscience community. These extreme conditions of high temperature

and high pressure will be made available on existing instruments and will play a major role in the future development of instruments in the new eastern guide hall which is actually under construction.

10.3 Potential industrial applications of the research neutron source Forschungsneutronenquelle Heinz Maier-Leibnitz (FRM II)

Ralph Gilles¹, Jürgen Neuhaus¹

¹ZWE FRM II, Technische Universität München

To start further co-operation between TU München Forschungsneutronenquelle Heinz Maier-Leibnitz (FRM II) and industrial partners a workshop took place on September 12th, 2006 in Garching. The workshop was organized under the auspices of the VDI-Werkstofftechnik (presented by Dr. H.J. Schäfer) settled in Düsseldorf, Germany. About 50 participants were registered at the workshop. The companies as BMW AG, DLR, Siltronic AG, MTU Friedrichshafen, Infineon, General Electrics, Hilti and Osram as well as small companies from the surrounding

of Munich were present and involved in contributions.

The scope of the workshop was to bring together different groups as people from industry, scientists working in the field of applied science with neutron scattering methods and scientists who are responsible for neutron instruments which are used for industrial relevant applications. The main topic was to work out for which industrial problems neutrons are a unique probe to solve open questions or provide an important complementary method to achieve a complete characterization of

the sample. As an introduction to the workshop a compilation of different talks were presented. Half of the presentations were coming from industry partners to present first results by using neutrons as a probe for their investigations. In the second part of the talks instrument responsables gave an overview about the potential of the instruments and the experience with industrial customers to provide information especially for novices. The main topics which were discussed rely on the possibilities to measure stress and strain in automotive components, to x-

ray objects in a non-destructive way by using tomography or radiography and the possibility to irradiate samples with neutrons. This includes the production of radioactive isotopes, the activation analysis for highly sensitive chemical analysis, the production of radioactive tracers and doping of semiconductors (transmutation doping).

After the talks a poster presentation took place where industrial customers had the opportunity to discuss in detail how to perform experiments at the different instruments and how to apply for beam time. For many participants the highlight has been the guided tour through the FRM II facility at the end of the workshop. It enabled them to look very close to the real instruments and to catch a glimpse of the heart of the facility, the reactor pool.



Figure 10.3: Spirited discussions during the lunch break and poster session.

10.4 Workshop for neutron scattering from biological and soft matter interfaces

Bert Nickel¹

¹Department für Physik, Ludwig-Maximilians-Universität München

On 22nd September 2006, the workshop on neutron scattering from biological and soft matter interfaces was held at the Forschungsneutronenquelle Heinz Maier-Leibnitz (FRM II) in Garching, Germany. The workshop was organized jointly by the REFSANS team from the LMU München and GKSS, Geesthacht, respectively. During the first talks the scientific perspectives for neutron scattering in areas such as membrane physics and surfactant chemistry were highlighted by Adrian Rennie (Uppsala U.) and Tim Salditt (U. Göttingen).

The performance of the new neutron reflectometer REFSANS at the FRM II was reported by R. Kampmann (GKSS). REFSANS is a unique time of flight instrument which allows switching from a reflectometry mode to a grazing incidence small angle neutron scattering mode (GISANS)



Figure 10.4: Participants in front of the FRM II main building.

by remote control. The first experiments in the GISANS mode using heterogeneous polymer films (group of P. Müller-Buschbaum, TUM) obtained results which demonstrate that REFSANS will be able to compete with the respective ILL instruments. Furthermore, first reflectometry experiments indicate that a dynamic range of eight orders of magnitude seems to be possible in favourable cases.

In the afternoon session presentations from M. Tanaka (U. Heidelberg), I. Köper (MPI Mainz), R. Willumeit (GKSS), P. Vandoolaeghe (Lund U.) and the group of C. Papadakis (TUM) ranged from the study of biomimetic surface architectures to bacterial defence mechanisms.

A special focus of the workshop was to discuss infrastructure and sample environment needs for such experi-

ments. In this context, a new microfluidic cell which combines fluorescence microscopy and neutron reflectometry was presented by Bert Nickel (LMU). These cells reduce the amount of liquid required for the neutron experiments to 3 ml, an important aspect if rare (e.g. deuterated) biomolecules such as membrane proteins are to be studied.

10.5 Farewell colloquium for Prof. Dr. Klaus Schreckenbach

Jürgen Neuhaus¹

¹ZWE FRM II, Technische Universität München

On the occasion of the leave of Prof. Klaus Schreckenbach as technical director of the FRM II, the Technische Universität München organized a farewell colloquium on 15th May 2006. Prof. Schreckenbach has directed the reactor department from May 1999 to December 2005. During this time he had to overcome a huge number of hurdles to obtain the nuclear license for the reactor and to put him final into operation in March 2004. The welcome address of the university was held by the vice president Prof. Rudolf Schillinger. Prof. Winfried Petry reviewed in a pleasing presentation the scientific and private life of Klaus Schreckenbach, showing aspects ranging from nuclear physics to hill climbing in the Himalayas mountains. The commemorative speech was held by Prof. Dieter Richter, FZ-Jülich on soft matter research at the JCNS.

The evening was closed by a Bavarian dinner, where numerous discussions concerning neutrons, reactors and even hill climbing have accompanied an in-

teresting event. Prof. Klaus Schreckenbach has retired from his position as technical director of the FRM II to pursue an academic task in the Physics De-

partment. He concentrates now on research with positrons and education of students.



Figure 10.5: Winfried Petry and Klaus Schreckenbach trying to display Himalaya pictures.

Part III

Facts and Figures

11 Experiments and user program

J. Neuhaus², U. Kurz², B. Tonin-Schebesta², W. Wittowetz², E. Jörg-Müller²

²Forschungsneutronenquelle Heinz Maier-Leibnitz, FRM II, TU München

The user office

The FRM II is operated as a user facility with international access to the instruments. The available beam time is shared to 2/3 for proposals which have to be approved by an international referee committee and 1/3 is given to the scientific groups which maintain the instruments. By this we ensure well maintained and technical up to date instruments which enable first-class experiments.

Business as usual might not be the right expression for the first year of full operation and 260 days neutron beams. However, in the year 2006 we had again 2 proposal rounds in January and August. This cycle in between the deadlines of other facilities seems to be an appropriate timing for our users. Altogether we got 301 proposals requesting 2700 days of beam time which lead to an average overload factor of two. So this scenario is not different from the one of the previous year.

More interestingly we performed in total, i.e. including the internal beam time for the instrument groups, 687 experiments during 3001 days of beam time, summed up over all instruments. As we were in the first year of full operation still 17% of this beam time was used for instrument development and improvement. As several instruments are still in the commissioning phase this number is expected to decrease during the next years.

The proposals originate from a large number of different countries. Summing up the statistics from 2005 and 2006 we counted 62% of the proposals from Germany, 30% from European countries, eligible for support from the FP6 NMI3 initiative and the rest of 8% from other countries, mainly from Russia and the United States.

The proposal submission is done online in the user office system (<http://user.frm2.tum.de>). Each proposer has to register for a personal account in the system. Using the module Proposal

the user is guided through a questionnaire concerning the experimental parameters. In addition a written scientific motivation in form of a pdf file with a length of maximal two A4 pages is required. A detailed guide line for proposal submission is given in the section *user guide* in the online system.

In addition to the proposal submission the user office system collects experimental reports which are requested for each experiment. The reports will be published online on our Internet pages.



Instruments

In the year 2006 the instruments could prove their performance in a large number of experiments. Nevertheless fine tuning and improvements as well as partly commissioning took about 17% of the beam time as mention above. The increasing number of publications (14.1) shows the scientific output of the experiments, even if a large number are still under preparation or to be submitted.

The table 11.1 summarizes all instruments, working, commissioning or under construction. The number given in column *position* corresponds to the position number in figure 11.2.

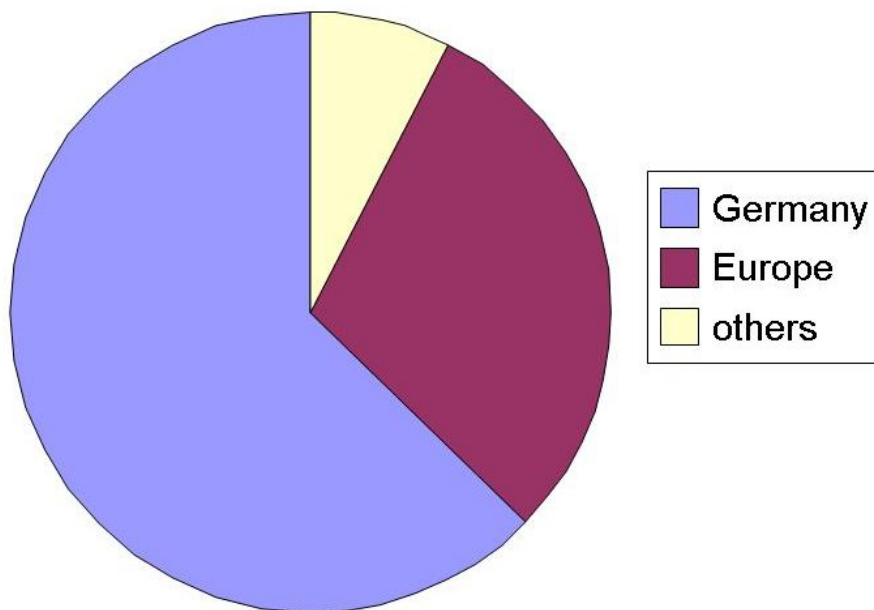


Figure 11.1: Received proposals by country of the main proposer.

Instrument	position	operated by	experiments
Experimental hall			
Panda	SR2 (17)	TU Dresden	36, 231 days
Stress-Spec	SR3 (18)	HMI	45, 238 days
Antares	SR4b (19)	TU München	93, 194 days
Trisp	SR5b (21)	MPI Stuttgart	22, 260 days
Puma	SR7 (22)	Univ. Göttingen, TU München	36, 198 days
Spodi	SR8a (23)	TU Darmstadt, LMU München	69, 231 days
Resi	SR8b (24)	Univ. Augsburg, LMU München	28, 220 days
Heidi	SR9b (25)	RWTH Aachen	29, 195 days
Nectar	SR10h (26)	TU München	42, 193 days
Medapp	SR10v (27)	TU München	commissioning
Nepomuc*	SR11 (28)	TU München, Univ. Bundeswehr	21, 139 days
Neutron guide hall			
N-Rex ⁺	NL1 (1)	MPI Stuttgart	first experiments
Mephisto	NL1 (5)	TU München	6, 260 days**
NSE	NL2ao (2)	JCNS	commissioning
TofTof	NL2au (3)	TU München	28, 160 days
Refsans	NL2b (4)	GKSS, LMU München	first 10 experiments, 208
KWS-3	NL3a (6)	JCNS	under construction
KWS-1	NL3a (7)	JCNS	under construction
KWS-2	NL3b (8)	JCNS	under construction
PGAA	NL4b (10)	Univ. Köln, TU München	commissioning
Reseda	NL5ao (11)	TU München	3, 21 days [†]
Spheres	NL6a (14)	JCNS	commissioning
DNS	NL6a (15)	JCNS	under construction
Mira	NL6b (16)	TU München	47, 248 days

Table 11.1: List of instruments at the FRM II in December 2006. Experiments in cycles 5-9 including instrument development. (*Nepomuc 3 Instruments, **including setup of the experiments, [†] partly commissioning)

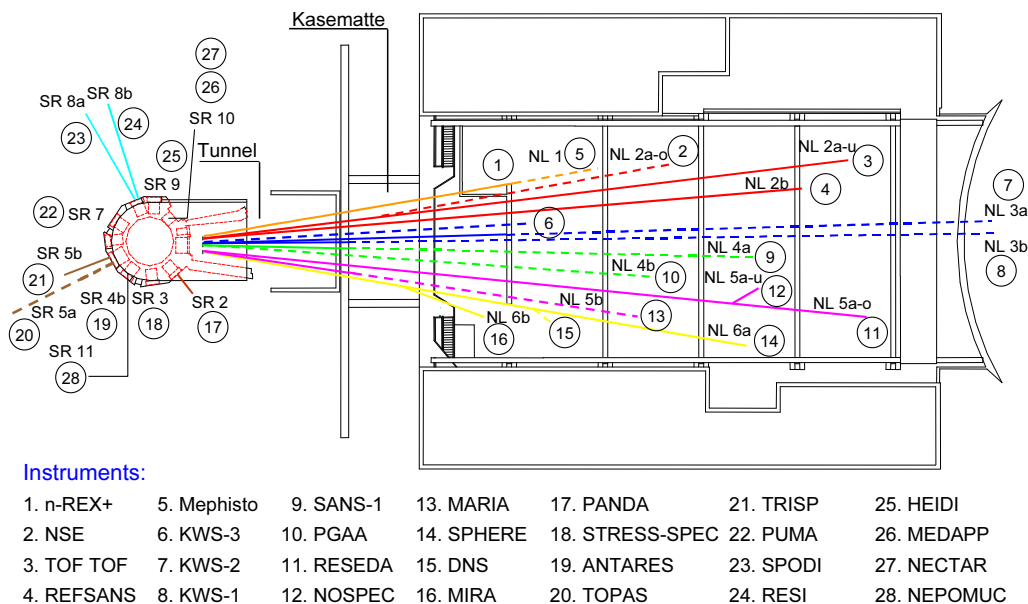


Figure 11.2: Position of the instruments in the experimental and neutron guide hall.

User support

Business as usual, however, might be the right expression for the user office team that helps to organize the stay at the FRM II for external visitors. They provide support for hotel booking and other organizational help. A central e-mail (userinfo@frm2.tum.de) and phone number (+49 899 289 14313) is reachable during normal office hours. A guest house is still not yet available on site, which unfortunately will not change in 2007.

European users are supported by the NMI3 project, under which travel and subsistence costs can be reimbursed for up to two scientists per experiment. So far all proposals which have been accepted by the referee committees could be supported.



Figure 11.3: Exhibition of the FRM II on the cluster congress.

Industrial applications

The presentation of the FRM II for industrial researcher has a long tradition for our institute. Already in the early days during the construction phase of the reactor, we organized regularly workshops and seminars. This year we have presented industrial applications with neutrons together with the VDI-W (10.3 in order to get closer contacts to engineers.

In the year 2006 we participated at the symposium *Material Innovativ, Automobil – Forschung – Energietechnik* which took place at the University of

Bayreuth on 29th March. Winfried Petry explained in a lecture how neutron could be used to design new materials. The symposium was organized by *Bayern Innovativ*, a publicly held company that was set up by the Bavarian State Government in 1995. It was initiated by politics, science and industry as a corporation for innovation and technology transfer.

Already in 2005 the Bavarian Ministry of Economic Affairs, Infrastructure, Transport and Technology initiated the Cluster Strategy in order to further mobilize the cooperation of indus-

try with research institutions and universities. The inauguration of the cluster took place at the M,O,C, fair center Munich on 2nd February 2006. The organization was done by *Bayern Innovativ* in collaboration with the Technische Universität München. More than 1000 participants and 80 exhibitors joined in the successful congress. The FRM II was presented by Dr. Ralph Gilles and Dr. Jürgen Neuhaus who explained the possibilities of neutron scattering for the development of new materials and the irradiation facilities of the FRM II for element analysis and isotope production.

12 Public relations and visitor service

J. Neuhaus³, U. Kurz³, B. Tonin-Schebesta³

³Forschungsneutronenquelle Heinz Maier-Leibnitz, FRM II, TU München

Our visitor service could welcome 2480 people in 2006. Some of the more prominent ones are depicted on the first pages (3). The demand has again exceeded our possibilities for guided tours. We are pleased, that we could increase the number of visiting students at the FRM II by more than a factor of three. In 2006 we had 47 groups and in total 707 students on site visiting our institute. In addition 20 groups of pupils (278 persons) could be welcomed during the year. Some times it even happens that VIP's bring along students to their visit.

The day of open doors 2006 was jointly organized by the scientific campus in Garching. This day, the 15th October 2006 was put together with the inauguration of the underground U6 with the terminal station *Forschungsgelände Garching*. By this line, the connection to Garching and Munich city is provided 7 days a week until the late evening hours, which is a big advantage especially for our scientific users working late in the evening and during the weekend.

The still unchanged tremendous request to get informations about the FRM II motivated us to increase our portfolio of informations at the day of open doors. Besides our guided tours through the reactor building where 489

visitors got the opportunity to see the instruments working, 2 talks in the lecture hall were given by Prof. Winfried Petry. The large lecture hall in the physics department in addition was used to show two recent films about



Figure 12.2: Great interest on the exhibition of the radiation protection department.



Figure 12.1: Cuban delegation in the neutron guide hall. Prof. Fidel Castro (in front) explaining his son (student in Madrid) where the neutrons are.



Figure 12.3: Exhibition of the FRM II in the central tent.



Figure 12.4: Lively discussions at the reactor pool to explain the unique possibilities of neutron beams.

the science of the FRM II. The one produced by the *Bayerischen Rundfunk* gives an overview about the institute and scientific applications, the other produced by a film team from Cologne was broadcasted in the TV station Vox in the channel *Auto Motor Sport* and showed how radiography with neutrons give an insight in to car engines.

Lively discussions at the exposition of natural radioactivity and instruments to measure radiation of our division of radiation protection encourage us to continue this dissemination of information for the general public.

The FRM II participated as well with a stand in the exhibition tent in the central area of the campus. Here more general information about the FRM II was given in numerous discussions. Scientists as well as people from the general public were informed about the use of neutrons for science and industry.

During the summer 2006 Germany was taken by the overwhelming event of the football world championship. On the occasion of the opening game in Munich, the Bavarian State Chancellery invited CEO's from industry and banking, which took the opportunity to visit the FRM II. Accompanied by the Bavarian Minister of Economic Affairs, Infrastructure, Transport and Technology, Erwin Huber, the visitors were welcomed by our President Prof. Dr. Dr. Wolfgang Hermann, who gave an introduction to

the Technische Universität München. Subsequently Dr. Jürgen Neuhaus gave in a short presentation an overview about the application of neutrons in science and industry at the FRM II. The following guided tour through the reactor building provided more insight to the operation of the reactor and its utilization.

On the invitation of the Bavarian State Minister of Science, Research and Arts, Dr. Thomas Goppel, members of the European Parliament came to a presentation of the FRM II at the Bavarian Embassy in Brussels on 26th June 2006. Presentations were given from site of politicians by Dr. Beatrix Vierkorn-Rudolph (Federal Ministry of Education and research) and Dr. Thomas Goppel. It was pointed out, how the FRM II is



Figure 12.5: Science meets politics in Brussels.



Figure 12.6: Science meets politics in Garching.

integrated in the European research infrastructure and how the already established international use of the FRM II in the order of 40% can still be increased.

The FRM II itself was presented by Prof. Winfried Petry, showing possible applications of neutrons for basic science as well as for applied research. In further presentations Prof. Dieter Richter (FZ-Jülich) showed how neutron scattering can contribute to soft-matter research in a large variety of today's products. The medical application of fast neutrons was demonstrated by Prof. Michael Molls, Klinikum Rechts

der Isar, who showed at level particle beams and especially neutrons are favorable for the radiation treatment of cancers.

One highlight during the year concerning the visits of policy-makers at the FRM II has clearly been the visit of the Minister president of North Rhine-Westphalia and nearly his entire cabinet on the 25th September 2006. On invitation of Minister Dr. Thomas Goppel and on the occasion of the common Bavarian North Rhine-Westphalia cabinet meeting in Munich, the FRM II got the opportunity to be presented as the

leading national neutron source in Germany. After the welcome of our President Prof. Dr. Wolfgang Herrmann and a short introduction of Prof. Winfried Petry the guest could take own impressions on the reactor installation itself as well on the broad range of applications for neutrons. Special emphasis was put to explain, how the Technische Universität München operates a large scale facility and how scientific groups from all over Germany participate on the use of the FRM II by building and operating scattering instruments.

Wie Materialspannungen sichtbar werden

Mit Hilfe des Forschungsreaktors lässt sich die Druckverteilung in festen Körpern präzise darstellen

Münchner U-Bahnnetz wieder etwas gewachsen

U 6 fährt jetzt bis Garching

Grundlage für Supraleiter

Keller ist magnetischen Effekten auf der Spur

Neues aus der Nanowelt

Max-Planck-Forscher kooperieren am FRM II

Neue Perspektiven für Zellmembran-Forschung

Präzise Untersuchungen an Schichtgrenzen

Der Neutronenreflektometer „Refsans“ eröffnet die Möglichkeit, selbst die Verteilung von Molekülinseln noch zu messen

Büros für 100 neue Arbeitsplätze

Garching ■ Gut 100 zusätzliche Büroarbeitsplätze werden nach Angaben der TU demnächst am Forschungsreaktor FRM II in Garching benötigt.

Neutronen für die Geowissenschaften

Garching ■ Um den Einsatz von Neutronenstrahlen in den Geowissenschaften ging es bei einem internationalen Workshop, den die Forschungsneutronenquelle Heinz Maier-Leibnitz (FRM II)

Technischer Direktor geht

Klaus Schreckenbach gibt Amt am FRM II ab

Neuer Direktor am FRM 2

Ingo Neuhaus am Reaktor für Technik zuständig

Erfolgreiches Pilotexperiment

Basis für neue Forschungseinrichtung an Garchinger Neutronenquelle geschaffen

Behandlung am Reaktorbecken

Wissenschaftler sind begeistert von Deutschlands neuestem Atomreaktor. Seiner Inbetriebnahme ging ein langer Streit voraus, der durch medizinische Experimente wieder ausbrechen könnte

Nachgefragt

Was fließt da in die Isar rein?

Helmut Zeising ist Strahlenschutzbeauftragter am Forschungsreaktor FRM II der TU München. Anlässlich der Diskussion um die Veröffentlichung von Messwerten der radioaktiven Abwässer stand er Alexandra Vettori Rede und Antwort.

13 People

13.1 Committees

Strategierat FRM II

Chairman

Prof. Dr. Gernot Heger
Institut für Kristallographie
RWTH Aachen

Members

MRin Dr. Ulrike Kirste
Bayerisches Staatsministerium für Wissenschaft,
Forschung und Kunst

Dr. Rainer Koepke
Bundesministerium für Bildung und Forschung

Prof. Dr. Georg Büldt
Institut für Biologische Informationsverarbeitung
Forschungszentrum Jülich

Prof. Dr. Dosch
Max-Planck-Institut für Metallforschung
Stuttgart

Prof. Dr. Dieter Richter
Institut für Festkörperphysik
Forschungszentrum Jülich

Prof. Dr. Dirk Schwalm
Max-Planck-Institut für Kernphysik
Heidelberg

Prof. Dr. Helmut Schwarz
Institute of Chemistry
Technische Universität Berlin

Prof. Dr. Dr. Michael Wannemacher
Radiologische Klinik und Poliklinik
Abteilung Strahlentherapie
Universität Heidelberg

Prof. Dr. Ewald Werner
Lehrstuhl für Werkstoffkunde und -mechanik
Technische Universität München

Prof. Dr.-Ing. Heinz Voggenreiter
Director of the Institute of Structure and Design
German Aerospace Center (DLR) Köln

Prof. Dr. Götz Eckold
Institute of Physical Chemistry
Universität Göttingen (until 22 September 06,
succeeded by Prof. Braden)

Prof. Dr. Markus Braden
Physikalisches Institut
Universität zu Köln

Honorary Members

MDgt i.R. Jürgen Großkreutz

Prof. Dr. Tasso Springer

Guests

Prof. Dr. Dr. h.c. mult. Wolfgang A. Herrmann
Präsident

Technische Universität München

Dr.-Ing. Rainer Kuch
Beauftragter der Hochschulleitung
Technische Universität München

Dr. Michael Klimke
Referent der Hochschulleitung
Technische Universität München

Prof. Dr. Winfried Petry
ZWE FRM II
Technische Universität München

Dr. Ingo Neuhaus
ZWE FRM II
Technische Universität München

Guido Engelke
ZWE FRM II
Technische Universität München

Secretary

Dr. Jürgen Neuhaus
ZWE FRM II

Instrumentation advisory board (Subcommittee of the Strategierat)

Chairman

Prof. Dr. Markus Braden
Physikalisches Institut
Universität zu Köln

Members

Prof. Dr. Dirk Dubbers
Physikalisches Institut
Universität Heidelberg

Prof. Dr. Michael Gradzielski
Institut für Chemie
Technische Universität Berlin

Prof. Dr. Rainer Hock
Lehrstuhl für Kristallographie und Strukturphysik
Universität Erlangen

Prof. Dr. Werner Kuhs
GZG Abteilung Kristallographie
Universität Göttingen

Prof. Dr. Stephan Paul
Physik Department E18
Technische Universität München

Prof. Dr. Wolfgang Scherer
Lehrstuhl für Chemische Physik
Universität Augsburg

Prof. Dr. Wolfgang Schmahl
Dept. für Geo- und Umweltwissenschaften
Ludwig-Maximilians-Universität München
Deputy of the Chairman

Dr. habil. Dieter Schwahn
Institut für Festkörperforschung
Forschungszentrum Jülich

Prof. Dr. Andreas Türler
Institut für Radiochemie
Technische Universität München

Prof. Dr. Albrecht Wiedenmann
Abteilung SF3
Hahn-Meitner-Institut Berlin

Dr. habil. Regine Willumeit
GKSS Forschungszentrum Geesthacht

Guests

Dr. Michael Klimke
Referent der Hochschulleitung
Technische Universität München

Dr. Jürgen Neuhaus
ZWE FRM II
Technische Universität München

Dr. Klaus Feldmann
BEO-PFR
Forschungszentrum Jülich

Prof. Dr. Winfried Petry
ZWE FRM II
Technische Universität München

MRin Dr. Ulrike Kirste
Bayerisches Staatsministerium für Wissenschaft,
Forschung und Kunst

Guido Engelke
ZWE FRM II
Technische Universität München

Prof. Dr. Gernot Heger
Institut für Kristallographie
RWTH Aachen

Dr. Ingo Neuhaus
ZWE FRM II
Technische Universität München

Secretary

Dr. Peter Link
ZWE FRM II

Committee for industrial and medical use (Subcommittee of the Strategierat)

Chairman

Prof. Dr.-Ing. Heinz Voggenreiter
German Aerospace Center (DLR) Köln

Members

Automobile industry
Dr.-Ing. Rainer Simon
BMW AG München

Dr.-Ing. Maik Broda
Ford Forschungszentrum Aachen

Aerospace industry
Dr.-Ing. Rainer Rauh
Airbus Deutschland Bremen

Chemistry and environment
Dr. Jens Rieger
BASF AG Ludwigshafen

Secretary

Dr. Ralph Gilles
ZWE FRM II

Scientific committee - Evaluation of beamtime proposals (Subcommittee of the Strategierat)

Chairman

Prof. Dr. Wolfgang Scherer
Lehrstuhl für Chemische Physik
Universität Augsburg

Members

Prof. Dr. John Banhart
Abteilung Werkstoffe (SF3)
Hahn-Meitner-Institut Berlin

Dr. Philippe Bourges
Laboratoire Léon Brillouin
CEA Saclay

Prof. Dr. Markus Braden
Physikalisches Institut
Universität zu Köln

Prof. Dr. Heinz-Günther Brokmeier
Institut für Werkstofforschung
GKSS - Forschungszentrum Geesthacht

Prof. Dr. Thomas Brückel
Institut für Festkörperforschung
FZ-Jülich

PD Dr. Mechthild Enderle
Institut Laue Langevin
Grenoble

Dr. Hermann Heumann
Max-Planck-Institut für Biochemie
Martinsried bei München

Prof. Dr. Jan Jolie
Institute of Nuclear Physics
Universität zu Köln

Prof. Dr. Bernhard Keimer
Max-Planck-Institut für Festkörperforschung
Stuttgart

Prof. Dr. Andreas Magerl
LS für Kristallographie und Strukturphysik
Universität Erlangen

Prof. Dr. Karl Maier
Helmholtz-Institut für Strahlen- und Kernphysik
Universität Bonn

Dr. Joël Mesot
ETH Zürich und
Paul-Scherrer-Institut Villigen, Schweiz

Prof. Reinhard Dr. Krause-Rehberg
Department of Physics
Universität Halle

Dr. Stéphane Longeville
Laboratoire Léon Brillouin
Laboratoire de la Diffusion Neutronique
CEA Saclay

Prof. Dr. Andreas Meyer
Institut für Materialphysik im Weltraum
Deutsches Zentrum für Luft- und Raumfahrt (DLR)
Köln

Dr. Michael Monkenbusch
Institut für Festkörperforschung
Forschungszentrum Jülich

Prof. Dr. Werner Paulus
Structures et Propriétés de la Matière
Université de Rennes 1

Prof. Dr.-Ing. Anke Pyzalla
Max-Planck-Institut für Eisenforschung
Düsseldorf

Prof. Dr. Joachim Rädler
Department für Physik
Ludwig-Maximilians-Universität München

Prof. Dr. Günther Roth
Institut für Kristallographie
RWTH Aachen

Prof. Dr. Michael Ruck
Institut für Anorganische Chemie
Technische Universität Dresden

Prof. Dr. Wolfgang Schmahl
Dep. für Geo- und Umweltwissenschaften
Ludwig-Maximilians-Universität München

Prof. Dr. Bernd Stühn
Institut für Festkörperphysik
Technische Universität Darmstadt

Prof. Dr. Monika Willert-Porada
Lehrstuhl für Werkstoffverarbeitung
Universität Bayreuth

Scientific secretaries

Dr. Jürgen Neuhaus
ZWE FRM II

Dr. Martin Meven
ZWE FRM II

Dr. Christoph Hugenschmidt
ZWE FRM II

Dr. Tobias Unruh
ZWE FRM II

Dr. Peter Link
ZWE FRM II

TUM Advisory board**Chairman**

Prof. Dr. Ewald Werner
Lehrstuhl für Werkstoffkunde und -mechanik
Technische Universität München

Members

Prof. Dr. Peter Böni
Physik Department E21
Technische Universität München

Prof. Dr. Bernhard Wolf
Heinz Nixdorf-Lehrstuhl für medizinische Elektronik
Technische Universität München

Prof. Dr. Andreas Türler
Institut für Radiochemie
Technische Universität München

Prof. Dr. Arne Skerra
Lehrstuhl für Biologische Chemie
Technische Universität München

Prof. Dr. Markus Schwaiger
represented by Prof. Dr. Senekowitsch-Schmidtke
Nuklearmedizinische Klinik und Poliklinik
Klinikum Rechts der Isar
Technische Universität München

Guests

Dr. Michael Klimke
Referent der Hochschulleitung
Technische Universität München

Prof. Dr. Winfried Petry
ZWE FRM II
Technische Universität München

Guido Engelke
ZWE FRM II
Technische Universität München

Dr. Ingo Neuhaus
ZWE FRM II
Technische Universität München

Scientific steering committee

Chairman

Prof. Dr. Winfried Petry
ZWE FRM II
Technische Universität München

Members

Dr. Hans Boysen
Sektion Kristallographie
Ludwig-Maximilians-Universität München

Prof. Dr. Dieter Richter
Institut für Festkörperforschung
Forschungszentrum Jülich

Prof. Dr. Bernhard Keimer
Max-Planck-Institut für Festkörperforschung Stuttgart

13.2 Staff

Board of directors

Scientific director

Prof. Dr. W. Petry

Technical director

Dr. Ingo Neuhaus

Administrative director

G. Engelke

Experiments

Head

Prof. Dr. W. Petry

Secretaries

W. Wittowetz

E. Jörg-Müller

Secretary JCNS

St. Mintmans

Coordination

Dr. J. Neuhaus

H. Türck

H. Bamberger

Instruments

N. Arend (JCNS)

P. Aynajian (MPI-Stuttgart)

Dr. S. Bayrakci (MPI-Stuttgart)

Prof. Dr. P. Böni (E21)

J. Brunner

K. Buchner (MPI-Stuttgart)

Dr. T. Bücherl

P. Busch (JCNS)

M. Bröll (MPI-Stuttgart)

W. Bünten (JCNS)

E. Calzada

D. Etzdorf

J. Franke (MPI-Stuttgart)

Dr. H. Frielinghaus (JCNS)

Dr. U. Garbe (GKSS)

Dr. A.-M. Gaspar (Visiting scientist from Portugal)

Dr. R. Georgii

Dr. R. Gilles

Dr. M. Haese-Seiller (GKSS)

Dr. W. Häußler

F. Hibsich

Dr. O. Holderer (JCNS)

Dr. M. Hofmann

Dr. M. Hölzel (TU Darmstadt)

Dr. K. Hradil (Univ. Göttingen)

Dr. C. Hugenschmidt

Dr. V. Hutanu (RWTH Aachen)

Dr. A. Ioffe (JCNS)

S. Kampfer

R. Kampmann (GKSS)

Dr. T. Keller (MPI-Stuttgart)

P. Kudejova (Universität zu Köln)

Dr. V. Kudryaschov (GKSS)

B. Krimmer

D. Lamago

Dr. P. Link

Dr. B. Loeper-Kabasakal

C. Loistl

K. Lorenz

A. Mantwill (E21)

J. Major (MPI-Stuttgart)

M. Major (MPI-Stuttgart)

Dr. St. Mattauach (JCNS)

F. Maye (MPI-Stuttgart)

T. Mehaddene

Dr. M. Meven

Dr. R. Mole

S. Mühlbauer

Qi Ning (Visiting scientist from China)

M. Nülle (MPI-Stuttgart)

Dr. A. Ostermann

Dr. B. Pedersen

C. Piochacz

Dr. J. Rebelo-Kornmeier (HMI Berlin)

Dr. A. Radulescu (JCNS)

J. Repper

R. Repper

Dr. D. Rich

J. Ringe

Dr. P. Rottländer (JCNS)

Dr. A. Rühm (MPI Stuttgart)

A. Sazonov

Dr. B. Schillinger

H. Schneider (Univ. Göttingen)

Dr. A. Schneidewind (TU Dresden)

Prof. Dr. K. Schreckenbach (E21)

M. Schulz

R. Schwikowski

Dr. A. Senyshyn (TU Darmstadt)

G. Seidl

C. Smuda

M. Stadlbauer

B. Straßer

P. Stronciwilk (JCNS)

Dr. Y. Su (JCNS)

Dr. T. Unruh

F. M. Wagner

Dr. R. Wimpory (HMI Berlin)

Dr. H.-F. Wirth

Dr. Joachim Wuttke (JCNS)

Prof. Dr. O. Zimmer (E18)

Detectors and electronics

Dr. K. Zeitelhack

Dr. I. Defendi

S. Egerland

Chr. Hesse

Dr. A. Kastenmüller

M. Panradl

Th. Schöffel

Sample environment

Dr. J. Peters

P. Biber

H. Kolb

A. Pscheidt

A. Schmidt

J. Wenzlaff

Neutron optics

Prof. Dr. G. Borchert

C. Breunig

H. Hofmann

E. Kahle

O. Lykhvar

Dr. S. Masalovich

A. Ofner

A. Urban

R. Valicu

IT services

J. Krüger

H. Wenninger

L. Bornemann

J. Ertl

J. Dettbarn

S. Galinski

H. Gilde

F. Hänsel

J.-P. Innocente

R. Müller

A. Preller

J. Pulz

C. Rajaczak

S. Roth

A. Schwertner

M. Stowasser

B. Wildmoser

Construction

K. Lichtenstein

Administration

Head

G. Engelke

Secretary

C. Zeller

Members

R. Obermeier

B. Bendak

B. Gallenberger

I. Heinath

K. Lüttig

Public relations

I. Scholz (ZV TUM)

A. Schaumlöffel (ZV TUM)

Visitor's service

U. Kurz

Dr. B. Tonin-Schebesta

Reactor operation

Head

Dr. Ingo Neuhaus

Secretaries

M. Neuberger

S. Rubsch

Management

Dr. H. Gerstenberg

(Irradiation and fuel cycles)

Dr. J. Meier

(Reactor operation)

R. Schätzlein

(Electric and control technology)

Shift members

F. Gründer

A. Bancsov

A. Benke

M. Danner

Chr. Feil

M. Flieher

H. Groß

L. Herdam

F. Hofstetter

K. Höglauer

T. Kalk

G. Kaltenegger

U. Kappenberg

F. Kewitz

M. G. Krümpelmann

J. Kund

A. Lochinger

G. Mauermann

A. Meilinger

M. Moser

L. Rottenkolber

G. Schlittenbauer

Technical services

K. Pfaff

R. Binsch

H. Gampfer

W. Glashauser

G. Guld

B. Heck

G. Wagner

A. Weber

M. Wöhner

C. Ziller

Sources

C. Müller

D. Päthe

A. Wirtz

Electric and control technology

R. Schätzlein

G. Aigner

W. Buchner

R. Krammer

K.-H. Mayr

Ü. Sarikaya

H. Schwaighofer

J. Wildgruber

Irradiation

Dr. H. Gerstenberg

J.-M. Favoli

Dr. X. Li

M. Oberndorfer

W. Lange

V. Loder

A. Richter

H. Schulz

F.-M. Wagner

N. Wiegner

Reactor enhancement

M. Schmitt

B. Struth

V. Zill

R. Lorenz

Technical design

F.-L. Tralmer

J. Fink

H. Fußstetter

J. Jüttner

G. Langenstück

K. Lichtenstein

Workshops

C. Herzog

U. Stiegel

A. Begic

M. Fuß

A. Huber

A. Scharl

R. Schlecht jun.

Radiation protection

Dr. H. Zeising

S. Dambeck

W. Dollrief

H. Hottmann

D. Kugler

B. Neugebauer

D. Schrulle

H.-J. Werth

S. Wolff

D. Bahmet

W. Kluge

A. Schindler

D. Strobl

Chemical laboratory

U. Jaser

C. Auer

R. Bertsch

S. Kiermaier

Technical safety service

J. Wetzl

R. Maier

J. Aigner

K. Otto

N. Hodzic

J. Schreiner

Reactor physics

Dr. A. Röhrmoser
C. Bogenberger

R. Jungwirth
W. Schmid

N. Wieschalla

Security department

L. Stienen

J. Stephani

13.3 Partner institutions

GKSS Research Centre GmbH

Max-Planck-Straße 1
21502 Geesthacht
Germany
http://www.gkss.de/index_e.html

Hahn-Meitner-Institute GmbH (HMI)

Glienickerstraße 100
14109 Berlin
Germany
http://www.hmi.de/index_en.html

Jülich Centre for Neutron Science JCNS

Research Centre Jülich GmbH
52425 Jülich, Germany
Outstation at FRM II: 85747 Garching
<http://www.jcns.info>

Max-Planck-Institut für Festkörperphysik

Heisenbergstraße 1
70569 Stuttgart
Germany
www.fkf.mpg.de/main.html

Max-Planck-Institut für Metallforschung

Heisenbergstraße 3
70569 Stuttgart
Germany
<http://www.mf.mpg.de/de/index.html>

RWTH Aachen

Institute of Crystallography
Jägerstraße 17 - 19
52056 Aachen
Germany
http://www.xtal.rwth-aachen.de/index_e.html

Technische Universität Darmstadt

Material- und Geowissenschaften
Petersenstraße 23
64287 Darmstadt
Germany
<http://www.tu-darmstadt.de/fb/matgeo/>

Technische Universität Dresden

Institut für Festkörperphysik
01062 Dresden
Germany
<http://www.physik.tu-dresden.de/ifp/ifp.php>

Universität Augsburg

Institut für Physik
Lehrstuhl für Chemische Physik und Materialwissenschaften
86135 Augsburg
Germany
<http://physik.uni-augsburg.de/exp3/home.html>

Universität der Bundeswehr München

Institut Angewandte Physik und Messtechnik
Werner-Heisenberg-Weg 39
85579 Neubiberg
Germany
<http://www.unibw.de/lrt2/>

Universität Göttingen

Institut für Physikalische Chemie
Tammannstraße 6
37077 Göttingen
Germany
<http://www.uni-pc.gwdg.de/eckold/home.html>

Universität zu Köln

Institut für Kernphysik
Zülpicherstraße 77
50937 Köln
Germany
<http://www.ipk.uni-koeln.de/>

Ludwig-Maximilians-Universität München

Sektion Kristallographie (Prof. Schmahl)
and Sektion Physik (Prof. Rädler)
Geschwister-Scholl-Platz 1
80539 Munich
Germany
<http://www.uni-muenchen.de>

14 Figures

14.1 Publications

- [1] Appavou M.-S., Busch S., Doster W., Unruh T. *The Effect of Packing in Internal Molecular Motions of Hydrated Myoglobin*. *MRS (Materials Research Society) Bulletin*, in press, 6 pgs.
- [2] Babcock E., Petoukhov A., Andersen K., Chastagnier J., Jullien D., Lelièvre-Berna E., Georgii R., Masalovich S., Boag S., Frost C., Parnell S. *AFP flipper devices: Polarized ^3He spin flipper and shorter wavelength neutron flipper; Proceedings of PCMI 2006, Berlin, Germany*. *Physica B*, submitted, 3 pgs.
- [3] Bayrakci S., Keller T., Habicht K., Keimer B. *Spin wave lifetimes throughout the Brillouin zone*. *Science*, **312**, (2006), 1926 – 1929. www.sciencemag.org/cgi/content/full/312/5782/1926/DC1.
- [4] Blackburn E., Hiess A., Bernhoeft N., Rheinstädter M., Häußler W., Lander G. *Fermi Surface Topology and the Superconductivity Gap Function in UPd_2Al_3 : A Neutron Spin Echo Study*. *Phys. Rev. Lett.*, **97 (057002)**, (2006), 057002–1–4.
- [5] Bunjes H., Unruh T. *Characterization of Lipid Nanoparticles by Differential Scanning Calorimetry, X-Ray and Neutron Scattering*. *Advanced Review in Pharmaceutical Science*, submitted.
- [6] Busch S., Doster W., Longeville S., Sakai V., Unruh T. *Microscopic Protein Diffusion at High Concentration - QENS Proceeding*. *MRS Bulletin*, in press, 8 pgs.
- [7] Cadogan J., Moze O., Ryan D., Suharyana, Hofmann M. *Magnetic ordering in DyFe_6Sn_6* . *Physica B*, **385 - 386**, (2006), 317 – 319.
- [8] Gilles R., Hölzel M., Schlapp M., Elf E., Krimmer B., Boysen H., Fuess H. *First test measurements at the new structure powder diffractometer (SPODI) at the FRM II*. *Z. Kristallogr.*, **23**, (2006), 183–188.
- [9] Gilles R., Mukherji D., Hoelzel M., Strunz P., Toebbens D., Barbier B. *Neutron and X-ray diffraction measurements on micro- and nano-sized precipitates embedded in a Ni-based superalloy and after their extraction from the alloy*. *Acta materialia*, **54 (5)**, (2006), 1307–1316.
- [10] Gilles R., Ostermann A., Petry W. *Monte Carlo simulations of the new Small-Angle Neutron Scattering instrument SANS-1 at the Heinz Maier-Leibnitz Forschungsquelle*. *J. Appl. Cryst.*, in press.
- [11] Gilles R., Ostermann A., Schanzer C., Krimmer B., Petry W. *The concept of the new small-angle scattering instrument SANS-1 at the FRM -II; Proceedings of ICNS 2005*. *Physica B*, **385-386**, (2006), 1174.
- [12] Hoelzel M., Del Genovese D., Gilles R., Mukherji D., Toebbens D., Roessler J., Fuess H. *Phase analysis and lattice mismatches in superalloys DT706 and Iconel 706, Proceedings of ICNS 2005*. *Physica B*, **385-386**, (2006), 594.
- [13] Hofmann M., Campell S., Link P., Fiddy S., Goncharenko. *Valence and Magnetic Transitions in YbMn_2Ge_2 - Pressure and Temperature*. *Physica B*, **385 - 386**, (2006), 330 – 332.
- [14] Hofmann M., Schneider R., Seidl G., Kornmeier J., Wimpory R., Garbe U., Brokmeier H. *The New Materials Science Diffractometer STRESS-SPEC at FRM-II*. *Physica B*, **385 - 386**, (2006), 1035 – 1037.
- [15] Hugenschmidt C., Schreckenbach K., Stadlbauer M., Straßer B. *First positron experiments at NEPOMUC*. *Appl. Surf. Sci.*, **252**, (2006), 3098–3105.
- [16] Häußler W., Gohla-Neudecker B., Schwikowski R., Streibl D., Böni P. *RESEDA - the new Resonance Spin Echo Spectrometer using cold neutrons at the FRM II*. *Physica B*, submitted, 3 pgs.
- [17] Kampf S., Wagner F.-M., Loeper B., Kneschaurek P. *Erste dosimetrische Ergebnisse an der neuen Neutronentherapieanlage am FRM II*. *Medizinische Physik ; Tagungsband der 37. Jahrestagung der Deutschen Gesellschaft für Medizinische Physik, 20. - 23. 09.2006 in Regensburg, herausgegeben von Ludwig Bogner and Barbara Dobler*, 2 pgs.

- [18] Keller T., Aynajian P., Habicht K., Boeri L., Bose K., Keimer B. *Momentum-resolved electronic-phonon interaction in lead determined by neutron resonance spin-echo spectroscopy*. *Phys. Rev. Lett.*, **96**, (2006), 225501–1–4.
- [19] Kögel G., Dollinger G. *Planned positron experiments at FRM-II*. *Applied Surface Science*, **252**, (2006), 3111–3120.
- [20] Lamago D., Georgii R., Pfeleiderer C., Böni P. *Magnetic-field induced instability surrounding the A-phase of MnSi: Bulk and SANS measurements*. *Physica B*, **385 - 386**, (2006), 385–387.
- [21] Li H., Schillinger B., Calzada E., Yinong L., Mühlbauer M. *An adaptive algorithm for gamma spots removal in CCD-based neutron radiography and tomography*. *Nuclear Instruments and Methods in Physics Research A*, **564**, (2006), 405–413.
- [22] Lin X., Henkelmann R., Türlér A., Gerstenberg H., De Corte F. *Neutron flux parameters at irradiation positions in the new research reactor FRM-II*. *Nuclear Instruments and Methods in Physics Research A*, **564**, (2006), 641–644.
- [23] Magaddino V. *The dependence of the relative biological effectiveness (RBE) of fission neutrons on dose and on gamma ray contamination in human SCC megacolonies*. *Master Thesis at University College London (European Master of Science in Radiation Biology)*.
- [24] Maye F. *Aufbau und Test einer Neutronen-Röntgen-Kontrast-Reflektometrie-Anordnung*. *Diploma Thesis at the Max-Planck-Institut für Metallforschung, Stuttgart, und Institut für Theoretische und Angewandte Physik der Universität Stuttgart*.
- [25] Mehaddene T., Neuhaus J., Petry W., Hradil K. *Phonon dispersions in NiAlMn shape memory alloy*. *Material Science & Engineering A*, submitted.
- [26] Mühlbauer Q., Hradil K. *Monitoring and Preventing collision for a triple axis Spectrometer*. *Proceedings of The IEEE International Conference on Central Applications, October 4 - 6, 2006, Munich, Germany*, 6 pgs.
- [27] Palancher H., Martin P., Sabathier C., Dubois S., Valot C., Wieschalla N., Röhrmoser A., Petry W., Jarousse C., Grasse M., Tucoulou R. *Heavy Ion Irradiation as a Method to Discriminate Research Reactor Fuels*. *Proceedings on the 'International Conference on Research Reactor Fuel Management RRFM 2006', May 04, 2006, Sofia*.
- [28] Pigozzi G., Mukherji D., Gilles R., Barbier B., Kostorz G. *Ni₃Si(Al)/a-SiO_x core shell nanoparticles: characterization, shell formation, and stability*. *Nanotechnology*, **17**, (2006), 4195 – 4203.
- [29] Pühlhofer T., Baier H., Krämer L., Unruh T. *Design, manufacturing and testing of high speed rotating CFRP chopper discs*. *SAMPE EUROPE International Conference 2006*.
- [30] Rühm A., Wildgruber U., Franke J., Major J., Dosch H. *n/X materials science reflectometer at FRM-II in Garching*. *Neutron Reflectometry, a Probe for Materials Surfaces; Proceedings of a Technical Meeting organized by the International Atomic Energy Agency and held in Vienna, 16-20 August 2004, Austria*, 161–175.
- [31] Schillinger B., Brunner J., Calzada E. *A study of oil lubrication in a rotating engine using stroboscopic neutron imaging*. *Physica B (6th International Conference on Neutron Scattering Sydney, November 2005)*, **385 - 386**, (2006), 921 – 923.
- [32] Schneidewind A., Link P., Etzdorf D., Schedler R., Rotter M., Loewenhaupt M. *PANDA – first results from the cold three axes-spectrometer at FRM-II*, *Proceedings of ICNS 2005*. *Physica B*, **385 - 386**, (2006), 1089–1091.
- [33] Senff D., Link P., Hradil K., Hiess A., Regnault L., Sidis Y., Aliouan N., Argyriou D., Braden M. *Magnetic excitations in multiferroic TbMnO₃*. *Phys. Rev. Lett.*, submitted.
- [34] Sergueev I., van Bürck U., Chumakov A., Asthalter T., Smirnov G., Franz H., Ruffer R., Petry W. *Synchrotron-radiation-based perturbed angular correlations used in the investigation of rotational dynamics in soft matter*. *Physical Review B*, **3**, (2006), 024203–1–12.
- [35] Smirnov G., van Bürck U., Franz A., Asthalter T., Leupold O., Schreier E., Petry W. *Nuclear gamma resonance time-domain interferometry: Quantum beat and radiative coupling regimes compared in revealing quasielastic scattering*. *Physical Review B*, **73**, (2006), 184126–1–9.
- [36] Stadlbauer M., Hugenschmidt C., Schreckenbach K., Straßer B. *Spatially Resolved Investigation of Thermally Treated Brass with a Coincident Doppler-Spectrometer*. *Appl. Surf. Sci.*, **252**, (2006), 3269–3273.
- [37] Stampanoni M., Borchert G., Abela R. *Progress in Microtomography with the Bragg Magnifier at SLS*. *Radiation Physics and Chemistry*, in press.

- [38] Stampanoni M., Groso A., Borchert G., Abela R. *Bragg Magnifier: High Efficiency, High Resolution X-Ray Detector*. *Proc. Syn. Rad. Instr.*, in press.
- [39] Strunz P., Mukherji D., Näth O., Gilles R., Röser J. *Characterization of nanoporous superalloy by SANS; Proceedings of ICNS 2005*. *Physica B*, **385-386**, (2006), 626.
- [40] Unruh T., Smuda C., Gemmecker G., Bunjes H. *Molecular dynamics in pharmaceutical drug delivery systems - the potential of qens and first experimental results*. *Mat. Res. Soc.*, in press.
- [41] Wagner F., Bücherl T., Kampf S., Kastenmüller A., Waschowski W. *Thermal Neutron Converter for Irradiations with Fission Neutrons. Conference Proceedings: Current Problems in Nuclear Physics and Atomic Energy (NPAAE-Kyiv2006), May 29 - June 03, 2006, Kyiv, Ukraine*, in press, 9 pgs.
- [42] Wieschalla N., Bergmaier A., Böni P., Böning K., Dollinger G., Großmann R., Petry W., Röhrmoser A., Schneider J. *Heavy ion irradiation of U-Mo/Al dispersion fuel*. *Journal of Nuclear Materials*, **357, 1-3**, (2006), 191–197.
- [43] Zeitelhack K., Schanzer C., Kastenmüller A., Röhrmoser, Daniel C., Franke J., Gutsmedl E., Kudryashov V., Maier D., Päthe D., Petry W., Schöffel T., Schreckenbach K., Urban A., Wildgruber U. *Measurement of neutron flux and beam divergence at the cold neutron guide system of the new Munich research reactor FRM-II*. *Nuclear Instruments and Methods in Physics Research A*, **560**, (2006), 444–453.
- [44] Boysen H., Lerch M., Stys A., Senyshyn A., Hoelzel M. *Oxygen mobility in the ionic conductor maynite ($Ca_{12}Al_{14}O_{33}$: a high temperature neutron diffraction study*. *Acta Cryst. B*, submitted.
- [45] Georgii R., Böni P., Janoschek M., Schanzer C., Valloppilly S. *A flexible instrument for VCN*. *Physica B*, in press.
- [46] Grigoriev S., Maleyev S., Okorokov A., Chetverikov Y., Böni P., Georgii R., Lamago D., Eckerlebe H., Pranzas K. *Magnetic structure of MnSi under an applied field probed by polarized small-angle neutron scattering*. *Phys. Rev. B*, **74 (21)**, (2006), 214414–1–10.
- [47] Hofmann M., Seidl G., Rebelo-Kornmeier J., Garbe U., Schneider R., Wimpory R., Wasmuth U., Noster U. *The New Materials Science Diffraktometer STRESS-SPEC at FRM II*. *Materials Science Forum Vols.*, **524 - 525**, (2006), 211 – 216.
- [48] Hugenschmidt C., Legl S. *A Novel Time-of-Flight Spectrometer for the Analysis of Positron Annihilation Induced Auger Electrons*. *Rev. Sci. Instr.*, **77**, (2006), 103904–1–6.
- [49] Hutanu V., Meven M., Heger G. *Construction of the New Hot Neutrons Single Crystal Diffractometer POLI-HEiDi at FRM-II (Proceedings of PNCMI 2006, Berlin, Germany)*. *Physica B*, in press.
- [50] Lerch M., Boysen H., Rödel T., Kaiser-Bischoff I., Hoelzel M., Senyshyn A. *High temperature neutron diffraction study of scandia/nitrogen co-doped zirconia*. *J. Sol. State Chem.*, submitted.
- [51] Park H.-S., Hoelzel M., Boysen H., Schmidbauer E. *Lithium conductivity in a Li-bearing ring silicate mineral, sogdianite*. *J. Sol. Chem.*, in press.
- [52] Pedersen B., Frey F., Scherer W., Gille P., Meisterernst G. *The new single crystal diffractometer RESI at FRM-II*. *Physica B*, **385 - 386**, (2006), 1046–1048.
- [53] Peters L., Knorr K., Evans J., Senyshyn A., Rahmoun H.-S., Depmeier W. *Proton positions in and thermal behaviour of the phase $4CaO * 3Al_2O_3 * 3H_2O$ and its thermal decomposition to $(OCa_4)2[Al_{12}O_{24}]$, determined by neutron/X-ray powder diffraction and IR Spectroscopic investigations*. *Z. Kristallographie*, in press.
- [54] Ranjan R., Agrawal A., Senyshyn A., Boysen H. *Phases in the system $Na_{1/2}Nd_{1/2} - SrTiO_3$: a powder neutron diffraction study*. *J. Phys.: Condensed Matter*, **18**, (2006), 9679 ff.
- [55] Ranjan R., Agrawal A., Senyshyn A., Boysen H. *Crystal structures of high temperature quantum paraelectrics $Na_{1/2}Nd_{1/2}TiO_3$ and $Na_{1/2}Pr_{1/2}TiO_3$* . *J. Phys.: Condensed Matter*, **18**, (2006), L515–L522.
- [56] Ranjan R., Senyshyn A., Frey F., Boysen H. *Crystal structure of $Na_{1/2}Ln_{1/2}TiO_3$ ($Ln : La, Eu, Tb$)*. *J. Sol. State Chem.*, in press.
- [57] Röhrmoser A., Petry W. *Reduced enrichment program for FRM II, actual status & principal study of monolithic fuel for FRM II; Proceedings on the 10th International Topical Meeting on Reserach Fuel Management, RRFM 2006, Sofia. 2006*, submitted.

- [58] Yeom J., Defendi I., Takahashi H., Zeitelhack K., Nakazawa M., Murayama H. *12-Channel CMOS Preamplifier-Shaper-Discriminator ASIC for APD and Gas Counters*. *IEEE Transactions on Nuclear Science*, **53**, No. 4, (2006), 5 pgs.

Imprint

.....

Publisher:
Technische Universität München
Forschungs-Neutronenquelle Heinz Maier-Leibnitz (FRM II)
Lichtenbergstr. 1
85747 Garching
Germany
Phone: +49 89-289-14966
Fax: +49 89-289-14995
Internet: <http://www.frm2.tum.de>
email: <mailto://userinfo@frm2.tum.de>

.....

Editors:
J. Neuhaus
B. Pedersen
E. Jörg-Müller, TUM

.....

Photographic credits:
All images: TUM, except otherwise noted

.....

Design:
B. Pedersen, TUM
J. Neuhaus, TUM
E. Jörg-Müller, TUM

.....

Typesetting(L^AT_EX 2_ε):
B. Pedersen, TUM
E. Jörg-Müller, TUM

.....